Dipl.-Ing. Harald Kraus

Development of an Operation Strategy for Plug-in Hybrid Electric Vehicles

Long-term Prediction and Adaptation based on Past Vehicle and Driver Data

Doctoral Thesis

to achieve the university degree of
Doktor der technischen Wissenschaften
submitted to

Graz University of Technology

Supervisors:
Assoc.Prof. Dipl.-Ing. Dr.techn. Arno Eichberger
Institute of Automotive Engineering, Graz University of Technology

Ao.Univ.-Prof. Dipl.-Ing. Dr.techn. Eranda Dragoti-Cela
Department of Optimization and Discrete Mathematics, Graz University of Technology

Graz, May 2016

Acknowledgement

The present thesis was part of my work as a scientific project researcher at the Institute of Automotive Engineering at Graz University of Technology, Austria. The project was conducted in cooperation with MAGNA Powertrain AG & Co KG Albersdorf, and I would like to thank all people involved in this project.

Many people contributed to this work. First of all, I want to thank Univ.-Prof.i.R. Wolfgang Hirschberg, the former head of the institute, who convinced me to start my scientific career there.

I would also like to express my heartfelt gratitude to my supervisor, Assoc.Prof. Arno Eichberger, for his outstanding support and guidance. In our time together, I have developed a deep appreciation not only for his professional and leadership competence, but for his social competence as well, and I have greatly enjoyed our collaboration.

I would also like to thank Ao.Univ.-Prof. Eranda Dragoti-Cela, who took the time to assess the thesis and gave me valuable input for improving it.

Furthermore, I owe a debt of gratitude to Dipl.-Ing. Dr.techn. Jürgen Fabian and Dipl.-Ing. Martin Ackerl for their valuable input, which improved my thesis. Without the help of all my graduate students, the development of this work would not have been possible. In particular, I personally want to thank Dipl.-Ing. Martin Hofstetter. Finally, I am grateful to all members of the Institute of Automotive Engineering for the pleasant atmosphere, the fertile environment and their friendly collaboration.

Of course, I am also deeply grateful for the unwavering support of my family, including my parents, Hermine and Bernhard Kraus, who enabled me to study and supported me whenever I needed it, as well as my sister, Claudia Kraus, and my grandmother, Stefanie Mayr, who also contributed to this work. Thank you for your emotional and mental support throughout the whole project.

Last but not least, my gratitude goes to all of my friends, each of whom contributed in their own way to help me keep sight of the goal, find new motivation and finish my work. Many thanks to all of them!

Harald Kraus
Graz, May 2016

Affidavit

I declare that I have authored this thesis independently, that I have not used other than the declared sources/resources, and that I have explicitly indicated all material which has been quoted either literally or by content from the sources used. The text document uploaded to TUGRAZonline is identical to the present doctoral thesis.

Date	Signature

Abstract

The automotive industry is facing significant pressure to drastically reduce in emissions in the near future in order to meet evolving legal requirements for fuel efficiency and CO_2 emissions. Alternative drivetrains, such as hybrid electric vehicles (HEVs), are regarded as a promising technology to help meet these challenges.

In addition to drivetrain layout, energy management is a crucial factor for achieving low emissions and high fuel efficiency. Expectations are high regarding two objectives that, at first glance, seem to be in conflict: fuel efficiency and vehicle performance. Furthermore, companies must grapple with the increasing difficulty of controlling HEVs that results from the ever-growing drivetrain complexity.

The present thesis develops an innovative operation strategy for plug-in hybrid electric vehicles (PHEVs), which simultaneously targets increased fuel efficiency and enhanced longitudinal vehicle performance by using advanced prediction and adaptation algorithms. Based on three different control paths, a novel holistic energy management controller that fulfils the driver demand at all times is introduced. This controller can account for all routes within and beyond the all-electric range (AER), depending on the information available. The core of this thesis is the novel prediction and adaptation (P&A) algorithm, which makes it possible to gather, process and utilise driving data from the driver's previous trips in order to increase the long-term prediction accuracy. The algorithm integrates fixed-position information (e.g., speed limits, route curvatures) with the driver's individual driving behaviour. Merging past individual driving data with predicted information enables additional fuel savings for PHEVs in real-world driving cycles.

Numerical simulations of the novel operation strategy have shown significant fuel savings up to 11% compared to conventional heuristic operation strategies, while efficiently utilising the energy content of the battery in real-world driving cycles. Incorporating individual driving styles into long-term prediction increases total longitudinal vehicle power, and thereby driving pleasure and vehicle agility, while concurrently improving fuel efficiency. Additional benefits should include increased customer acceptance, a higher market share for HEVs, reduced CO_2 emissions and other positive effects on the drivetrain layout.

Kurzfassung

Die Automobilindustrie muss sich mittelfristig mit drastischen Emissionsreduktionen auseinandersetzen, um künftige gesetzliche Anforderungen an Kraftstoffeffizienz und CO_2-Emissionen erfüllen zu können. Alternative Antriebe, wie z. B. Hybridfahrzeuge, scheinen eine vielversprechende Technologie darzustellen, mit denen diesen Herausforderungen entgegnet werden kann. Für die Gewährleistung niedriger Emissionen und hoher Kraftstoffeffizienz spielt das Energiemanagement neben der Antriebsstrangtopologie eine entscheidende Rolle. An die auf erstem Blick widersprüchlichen Entwicklungsziele des Kraftstoffeinparungspotentials und der Fahrleistung werden ungeachtet der anspruchsvollen Regelung von Hybridfahrzeugen durch die gestiegene Antriebsstrangkomplexität hohe Erwartungen gerichtet.

In der vorliegenden Arbeit wird eine innovative Betriebsstrategie für Plug-In Hybridfahrzeuge (PHEVs) entwickelt, welche gleichzeitig die Kraftstoffeffizienz, aber auch die Fahrleistung mittels zukunftsweisender Prädiktions- und Adaptionsalgorithmen steigert. Ein innovatives, ganzheitliches Energiemanagement, das den Fahrerwunsch stets umsetzt und auf drei unterschiedlichen Kontrollpfaden basiert, wird vorgestellt. Dieses berücksichtigt sowohl Strecken innerhalb und außerhalb der rein elektrischen Reichweite (AER). Die zentrale Funktion der innovativen Betriebsstrategie ist der Prädiktion & Adaption (P&A) Algorithmus, der die Daten der letzten Fahrten sammelt, verarbeitet und diese so einsetzt, dass sich die Genauigkeit der langfristigen Prädiktion erhöht. Infrastrukturgebundene Informationen, wie etwa Geschwindigkeitsbeschränkungen oder auch Kurvenverläufe, werden ebenso miteinbezogen wie das spezifische Fahrverhalten. Die Verschmelzung vergangener, individueller Fahrdaten mit prädizierten Informationen ermöglicht ein verbessertes Kraftstoffeinsparungspotential von Hybridfahrzeugen unter realen Verkehrsbedingungen.

Numerische Simulationen der neuartigen Betriebsstrategie zeigen, dass durch intelligentes Planen des Energieinhaltes der Batterie signifikate Verbrauchseinsparungen von bis zu 11 %, verglichen mit einer konventionellen, heuristischen Betriebsstrategie, bei Realfahrten erreicht werden können. Darüber hinaus ermöglicht das Miteinbeziehen des individuellen Fahrstils in die langfristige Prädiktion gesteigerte Fahrzeuglängsdynamik und daher auch mehr Fahrspaß sowie Fahrzeugagilität bei simultan verbesserter Kraftstoffeffizienz. Damit gehen steigende Kundenakzeptanz, höhere Marktanteile, reduzierte CO_2-Emissionen und weitere positive Auswirkungen auf das Antriebsstrangdesign einher.

Contents

Abbreviations

A/C	Air conditioning
ABS	Anti-lock braking system
AC	Alternating current
AC/DC	AC/DC power converter
ACC	Adaptive cruise control
ACEA	Association des Constructeurs Européens d'Automobiles (European Automobile Manufacturers' Association)
ADAS	Advanced driver assistance system
ADASIS	Advanced driver assistance systems interface specifications
AER	All-electric range
ANN	Artificial neuronal network
AUX	Auxiliary
AWD	All-wheel drive
BAT	Battery
BEV	Battery electric vehicle
BMU	Battery monitoring unit
BSFC	Brake-specific fuel consumption
BSG	Belt-driven starter generator
C	Graphite
C2C	Car-to-car
C2I	Car-to-infrastructure
C2X	Hypernym for car-to-car (C2C) and car-to-infrastructure (C2I) communication
CAN	Controller area network
CI	Compression ignition
CL	Clutch
CO	Carbon monoxide
Co	Cobalt
CO_2	Carbon dioxide
CoG	Centre of gravity
COP	Continuous-time optimisation problem
CPU	Central processing unit
CVS	Constant volume sampler
CVT	Continuously variable transmission

CW	Crown wheel
DAB	Digital audio broadcasting
DC	Direct current
DCT	Dual clutch transmission
DDP	Deterministic dynamic programming
DFCO	Deceleration fuel cut-off
DoF	Degree of freedom
DoH	Degree of hybridisation
DOP	Discrete-time optimisation problem
DP	Dynamic programming
ECMS	Equivalent consumption minimisation strategy
ECU	Engine control unit
eCVT	Electrical continuously variable transmission
EG	Electric generator
EM	Electric motor
EMG	Electric motor/generator
ES	Electrical system of the vehicle
ESP	Electronic stability program
ESS	Energy storage system
FCD	Floating car data
FCEV	Fuel cell electric vehicle
FD	Final drive
FIR	Finite impulse response
FLS	Fuzzy logic system
FM-RDS	Frequency modulation - Radio data system
FTG	Institut für Fahrzeugtechnik Graz (Graz Institute of Automotive Engineering)
GBX	Gearbox
GHG	Greenhouse gas
GIS	Geographical information system
GLONASS	Global navigation satellite system of Russia
GNSS	Global navigation satellite system
GPRS	General packet radio service
GPS	Global positioning system developed by the U.S. Department of Defense
GSM	Global system for mobile communication
HC	Hydrocarbons
HCU	Hybrid control unit
HEV	Hybrid electric vehicle
HFC	Hydrofluorocarbons
ICE	Internal combustion engine
IG-L	Immissionschutzgesetz Luft (Austrian ambient air quality protection act)
IMA	Integrated motor assist

IPCC	Intergovernmental Panel on climate change
ISG	Integrated starter generator
ITS	Intelligent transportation system
KPMG	Klynveld, Peat, Marwick and Goerdeler (a business auditing and consultancy company)
L1-In	Input-split
L1-Out	Output-split
LEZ	Low-emission zone
LiC_6	Lithiated graphite
Li-ion	Lithium-ion
$LiMO_2$	Lithium metal oxide
M	Transition metal
Mn	Manganese
MPC	Model predictive control
NEDC	New European Driving Cycle
Ni	Nickel
NMC	Nickel-Manganese-Cobalt
NoVA	Normverbrauchsabgabe (Austrian motor vehicle registration tax)
NOx	Nitrogen oxides
ODE	Ordinary differential equation
OEM	Original equipment manufacturer
OS	Operation strategy
P&A	Prediction and adaptation
PGS	Planetary gear-set
PHEV	Plug-in hybrid electric vehicle
PI	Proportional-integral
PID	Proportional-integral-differential
PM	Particulate matter
PMP	Pontryagin's minimum principle
PMR	Power-to-mass ratio
PMSM	Permanent-magnet synchronous motor
PN	Particulate numbers
PT1	First-order lag
PT2	Second-order lag
PTS	Parallel torque-split
RAM	Random access memory
RB	Rule-based
RDS-TMC	Radio data system - Traffic message channel
REx	Range extender
SDP	Stochastic dynamic programming
SEI	Solid-electrolyte interface
SG	Sun gear
SMPC	Stochastic model predictive control

SOC	State of charge
SOH	State of health
TC	Torque converter
TCS	Traction control system
TCU	Transmission control unit
Tt	Dead-time
VAT	Value-added tax
VDC	Vehicle dynamics control
VEH	Vehicle
WGS84	World geodetic system 1984
WLTP	Worldwide harmonized light vehicles test procedure
XFCD	Extended floating car data
ZEZ	Zero-emission zone

Symbols

Parameters and constants

a	acceleration
a_R	rolling resistance coefficient
a_y	lateral vehicle acceleration
A_x	frontal area of the vehicle
$\bar{a}_{x,\pm}$	average positive and negative vehicle acceleration
b	constant
B	constant
c_D	aerodynamic drag coefficient
C	capacitance
$\bar{C}$	fuel consumption
d	distance
D	constant
e	eccentricity of the vertical tyre load
E_Q	heat
$f(\,)$	function
F	force
$g(\,)$	function of the cost functional
g	gravity
$G(s)$	transfer function
h	height
$h(\,)$	function of the cost functional
H_u	lower heating value
i	number
i_γ	gear ratio of the selected gear
i_{FD}	gear ratio of the final drive
I	current
I_k	instantaneous cost-to-go at stage k
J	cost functional
J^*	optimal cost functional
K_f	fuel consumption correction coefficient
K_p	amplification factor of the PT1-element
K_v	speed correction factor

l	length
m	dimension of the control vector
$m_{k,f}$	instantaneous fuel consumption at discrete time step k
m_{VEH}	total vehicle mass
$\dot{m}$	mass flow
$\tilde{m}$	number of moles of carbon
M	memory demand
n	dimension of the state vector (= system dimension)
$\tilde{n}$	number of moles of hydrogen
N	total number of decision stages
$N^{\mathbf{u}}$	total number of all control space grid points at stage k
$N^{\mathbf{x}}$	total number of all state space grid points at stage k
N_{u_j}	number of control space grid points at stage k of one dimension
N_{x_i}	number of state space grid points at stage k of one dimension
$p(x)$	pressure distribution in horizontal direction
p_p	pedal position
$\tilde{p}$	number of moles of oxygen
P	power
Q	battery capacity
r	radius
r_m	average friction radius
r_κ	radius of a curve
R_{ct}	charge-transfer resistance
R_d	diffusion resistance
R_i	internal resistance
R_o	ohmic resistance
s	slip
s_{sl}	sliding surface
s_E	distance where a certain driving event occurs
t	time
t_S	stopping time
T	torque
$\bar{T}$	torque without system response
T_{BL}	computational time of the boundary-line calculation
$T^{(1)}_{DP,line}$	total computational time of DP using the boundary-line method
T_{DP}	total computational time of the backward DP calculation
T_l	first-order lag time of the PT1-element
T_t	delay time of the Tt-element
T_∞	calculation time of the infeasible grid domain
u	control variable
u_d	power distribution factor – a specific control variable
U	voltage
U_{RC}	voltage drop at the parallel RC-branch

v	speed
v_{L0}	vehicle speed threshold
v_{x0}	intended vehicle speed
v_E	vehicle speed at a certain event
$\bar{v}$	average speed
w	weighting factor
x	state variable
X	random variable

α	state variable of the random process
β	inclination of the road
γ	selected gear
ΔE	energy balance/difference
ΔQ	electricity balance
Δt_A	average time of an acceleration before a speed limit change
Δt_B	average time of a deceleration before a speed limit change
Δt_s	time step
Δt_U	update time period
Δt_W	time window
Δv	speed difference
$\Delta\omega$	rotational speed difference/slip
η	efficiency
ϑ	temperature
Θ	moment of inertia
κ	curvature
λ	mass of pollutant emission per km
μ	friction coefficient
μ_0	static friction coefficient
μ_{sl}	sliding friction coefficient
ν_k	normally distributed parameter within the interval $[-1 \quad 1]$
ρ	density
σ	gradeability of the vehicle in %
τ	average time of a single calculation step
$\phi(\,)$	penalty function
φ_γ	ratio of two consecutive gear ratios
φ_s	total gear spread
$\hat{\mathcal{P}}$	probability
Ψ_γ	progression coefficient
ω	rotational speed
$\dot{\omega}$	rotational acceleration
Ω_k^i	set of reachable states at stage k and node i

Vectors & Matrices

$\mathbf{a}_P$	predicted vehicle acceleration vector
$\mathbf{d}$	coefficient vector
$\mathbf{f}(\,)$	function vector
$\mathbf{u}$	control vector
$\mathbf{v}_P$	predicted vehicle speed vector
$\mathbf{w}_e$	vector of external disturbances
$\mathbf{x}$	state vector
$\dot{\mathbf{x}}$	derivative of the state vector
$\mathbf{y}$	vehicle state vector
$\mathbf{z}$	generalised speed vector
$\dot{\mathbf{z}}$	generalised acceleration vector
$\boldsymbol{\beta}_P$	predicted road inclination vector
$\boldsymbol{\mu}(\,)$	function vector
$\boldsymbol{\pi}$	policy vector
$\boldsymbol{\omega}$	rotational speed vector
$\dot{\boldsymbol{\omega}}$	rotational acceleration vector
$\mathbf{K}$	state space congruent transformation matrix
$\mathbf{M}$	rotational mass matrix
$\mathbf{T}$	torque vector
$\mathbf{Z}_P$	predicted input matrix

Indices

a	air
A	acceleration
av	average
B	brake/deceleration
$cont$	continuous
d	drag
D	air drag
dyn	dynamic
e	electric, end
E	event
f	fuel, front
hi	high
i	number of node
in	input
k	discrete time step

l	left
L	limit
lo	lower
max	maximum
min	minimum
nom	nominal
oc	open-circuit
out	output
P	predicted
pl	plate
Q	heat
r	right, rear
R	rolling
RC	parallel ohmic resistance (R) and capacitance (C) branch
req	requested
s	slip
sft	gear-shifting
sl	sliding
T	tyre
up	upper
x	longitudinal
y	lateral
z	vertical

β	inclination
γ	gear
κ	curvature
π	policy

0	initial
∞	infinite, saturation
$\prod$	product
$\sum$	sum
$+$	positive
$-$	negative

"If you would create something, you must be something".

Johann Wolfgang von Goethe (1749-1832)

1 Introduction

1.1. Background and Motivation

In recent years, there has been much debate about passenger vehicles within the automotive industry, as well as among politicians, consumers and society at large. Individual mobility is an integral part of modern society, and mobility is a key success factor of economic growth that contributes significantly to quality of life [121]. Nevertheless, individual traffic is increasingly producing negative effects, such as pollutions and noise exposure. Tightened fuel and emissions regulations, increased environmental awareness and rising fossil fuel costs are spurring the development of environmentally friendly vehicles.

Conventional gasoline or diesel-powered vehicles are still predominant [94], [184] due to their relatively low costs, long driving range and high driving comfort. In Germany, the total shares of diesel and gasoline-powered vehicles are approximately 31.2 % and 67.2 %. Only the small remainder of about 1.6 % are passenger vehicles with alternative drivetrains [94]. The Austrian registration statistics in 2014 show a similar trend, but diesel-driven vehicles have the biggest proportion (see Figure 1.1).

However, conventional drivetrain technology emits pollutants, such as carbon monoxide (CO), carbon dioxide (CO_2), nitrogen oxides (NOx), hydrocarbons (HC) and particulate matter (PM), and combustion also creates significant noise. Due to the advanced stage of technical maturity, further improvements require proportionally high research effort and costs. In addition to ongoing internal combustion engine (ICE) enhancements, original equipment manufacturers (OEMs) are combining different approaches to increase the overall vehicle efficiency and thus reduce the greenhouse gas (GHG) emitted. Common

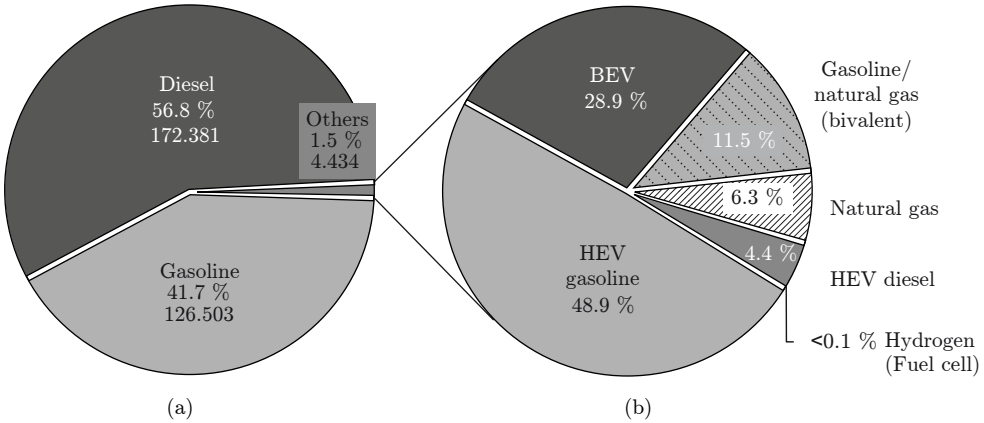

Figure 1.1.: Austrian statistics of newly registered motor vehicles in 2014 [11]

In 2014, 56.8 % of the newly registered passenger cars are propelled by diesel engines, 41.7 % are gasoline-driven, and only 1.5 % use alternative drivetrains, cf. Figure (a). Figure (b) shows the total share of alternative drivetrains. Hybrid electric vehicles (HEVs) with gasoline are predominat (48.7 %), followed by battery electric vehicles (BEVs) with 28.9 %. The rest are alternative drivetrains with gasoline/ natural gas (bivalent) (11.5 %), natural gas (6.3 %), diesel HEVs (4.4 %) and fuel cell electric vehicles (FCEV) with less than 0.1 %.

approaches are reducing the total vehicle mass by intelligently combining different materials, improving the vehicle's aerodynamic drag, lower the rolling resistance of tyres, and increasing the overall drivetrain efficiency by minimising friction and conversion losses. Despite significant advancements in recent years, conventional ICE-driven vehicles offer low energy efficiencies.

In addition, vehicles with alternative drivetrain layouts offer high development potential. They are able to improve energy efficiency and may reduce emissions. Hybrid electric vehicles (HEVs) are one approach to cope with the aforementioned challenges. They feature at least two different energy converters and two different energy storage systems [140] – usually a combination of a conventional ICE-driven drivetrain with an electric propulsion system. Partially recuperating the kinetic energy during braking and the additional degree of freedom (DoF) enable significant fuel saving and reduced CO_2 emissions – fuel savings of about 10 % (depending on the route driven) have been reported [127], [190], [214]. Since combining different propulsion technologies increases the system complexity and the total weight of the vehicle, operation strategies that faciliate the efficient coordination of the different propulsion units are crucial for all HEVs, in order to exploit the maximum potential of such means of transport [183]. The development of such operation strategies have kept OEMs and scientific researchers busy for years and is still ongoing.

The development of energy-efficient drivetrain layouts is furthermore affected by a variety

of challenges, including those related to economic, social, ecological and political factors. All of these reasons influence the development of vehicles with alternative drivetrains.

Economic drivers

Although the world demand for oil continues to increase, crude oil reserves are finite and non-renewable. Figure 1.2(a) shows the steady increase of world oil demand for different economic growth scenarios. Regardless of the growth scenario, the world crude oil demand will increase significantly. According to different studies [72], [153] and [188], oil production will peak in the near future, due to the fast-growing population and expected increasing mobility level in developing countries, in particular China and India [121]. Additionally, the costs of extracting and exploiting unconventional resources (e.g., heavy fuel oils, oil sand) are higher than those involved with conventional resources [153].

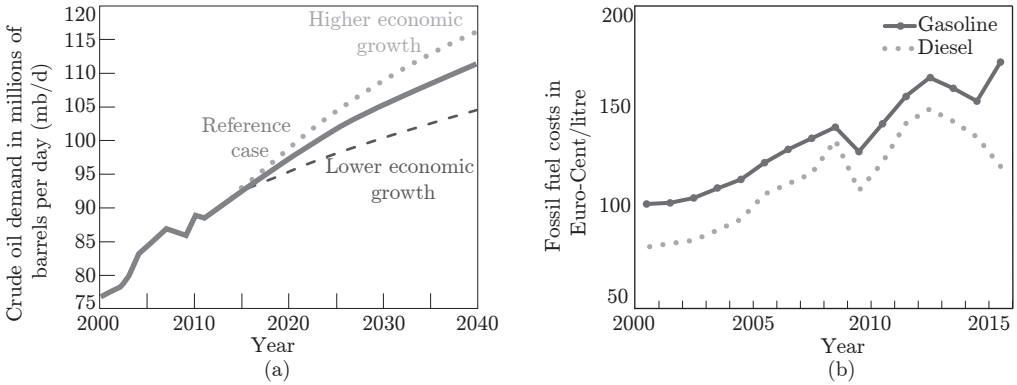

Figure 1.2.: Economic drivers influencing the development of highly efficient vehicles

Figure (a) shows the outlook for the world's crude oil demand under three different economic growth scenarios until 2040. Regardless of the growth scenario, the global demand is increasing [184]. Figure (b) shows the development of fuel costs in Germany based on data from [49], [50].

Moreover, consumer costs for fossil fuels are increasing. Figure 1.2(b) shows the development of fuel costs for diesel and gasoline (including all taxes) in Germany over the last 15 years. The increasing costs of producing and consuming fossil fuels provide motivation for the development of alternative vehicle propulsion systems.

Social drivers

The increase in demand for crude oil anticipated for the near future is closely related to the increase of the world population, see Figure 1.3(a). In highly developed industrialised countries, individual traffic has been a basic need for years, resulting in a high mobility level with a moderate growth rate. In contrast, developing countries, such as China

and India, currently have a low degree of mobility. These fast-growing countries will contribute to an increase of passenger traffic in the future, see Figure 1.3(b).

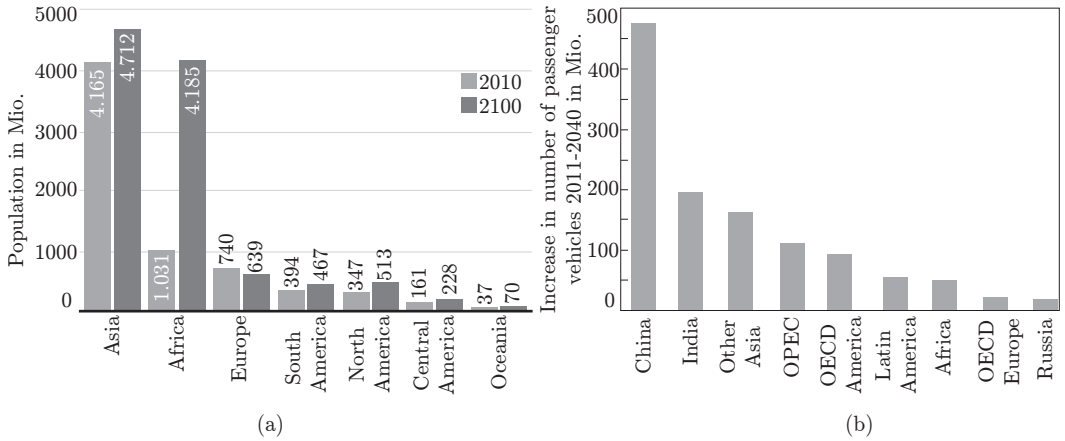

Figure 1.3.: Social drivers influencing the development of highly efficient vehicles

Figure (a) shows the world population in 2010 and the prediction for 2100 by continent [200]. It highlights the increasing world population in future. Figure (b) shows the increase of passenger cars until 2040 by several regions [184]. An increasing number of additional passenger vehicles will be registered.

Another important social factor is urbanisation. Due to increasing urban traffic density and the related pollution, noise exposure and traffic congestion, some cities have introduced *low-emission zones* (LEZs) or *zero-emission zones* (ZEZs) [28], [46], [162]. For example, London established the *congestion charging zone* in 2003 [160]. Entering this zone costs a predefined charge per day, and only low-emission vehicles (under 75 g/km CO_2) are excluded from that regulation. Plug-in hybrid electric vehicles (PHEVs) must also have an all-electric range (AER) of more than 10 miles, and their maximum vehicle speed must exceed 60 mph. A similar toll system was established in Milan, Italy [118], and other cities such as Munich, Berlin, Amsterdam, Hong Kong or Singapore also introduced LEZs [82], [158]. Austria has introduced similar environmental zones (marked as IG-L or Immissionsschutzgesetz Luft, English: Austrian ambient air quality protection act), which restrict speed limits in order to avoid excessive pollutants [4].

Ecological drivers

The operation of conventional ICEs inherently produces different pollutants. With the help of specific exhaust-gas catalytic converters and filters, the exhaust components CO, NOx, HC and PMs are effectively reduced [172]. The amount of CO_2 emitted is directly related to the overall fossil fuel consumption. According to [133], the relation for diesel

and gasoline engines reads

$$100\ \left(\frac{\mathrm{g}}{\mathrm{km}}\right) \mathrm{CO_2} = \begin{cases} 4.24\,\mathrm{l}/100\,\mathrm{km}, & \text{for gasoline } (\rho_{gasoline} = 2.36\,\mathrm{kg/l}) \\ 3.77\,\mathrm{l}/100\,\mathrm{km}, & \text{for diesel } (\rho_{diesel} = 2.65\,\mathrm{kg/l}) \end{cases} \tag{1.1}$$

Since CO_2 is a greenhouse gas, it is partially responsible for global warming [194]. Figure 1.4 shows that the GHG emissions from the transport sector have more than doubled since 1970 and increased at a faster rate than any other energy end-use sector in 2010. Around 80 % of this increasing trend has come from road vehicles, which contribute about 28 % of the total end-use energy [187]. According to a report by the *Intergovernmental*

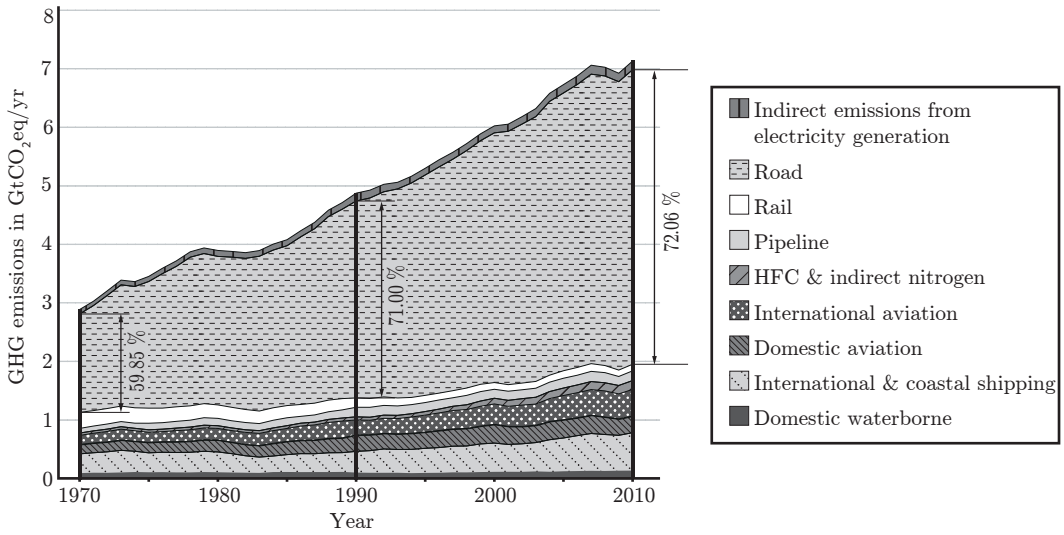

Figure 1.4.: Ecological drivers influencing the development of highly efficient vehicles

The GHG emissions in $GtCO_2eq/yr$[1] from road vehicles have more than doubled since 1970 with around 80 % of this increase from the growing transportation sector [187]. Emissions from other sectors, such as rail, pipeline, hydrofluorocarbons (HFCs) & indirect nitrogens and indirect emissions from electricity generation, are small compared to the road sector. Even shipping contributes a small proportion to the total transportation sector.

Panel on climate change (IPCC) [194], global warming risks are widespread and range from wildfire, increased extinction of wildlife, rising mean sea level and melting glaciers. The IPCC recommends a dramatic decrease in CO_2 emissions.

Political drivers

National, and even international politics are controlling the ecological effects of emissions by introducing different legal requirements. Legal regulations strongly depend on

[1] Gt CO_2 equivalent per year is obtained by multiplying the mass of the gas by the global warming potential of that gas.

the individual vehicle market (e.g., Japan, USA, Europe). In 1995, the European Automobile Manufacturers' Association (ACEA, *Association des Constructeurs Européens d'Automobiles*) voluntarily agreed to reduce the average CO_2 emissions of their new cars fleets to 140 g/km by 2008, which was not achieved [151]. Figure 1.5 highlights the CO_2

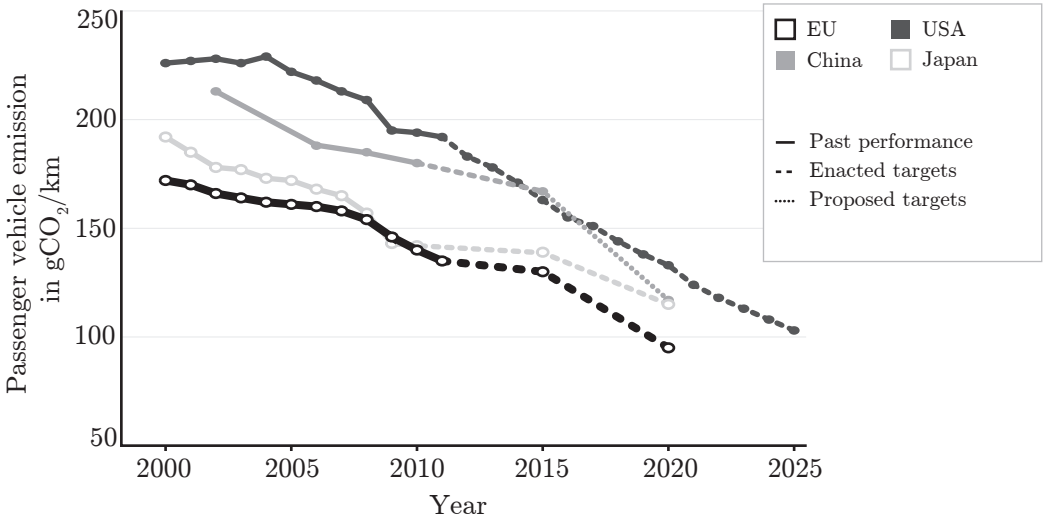

Figure 1.5.: Political drivers influencing the development of highly efficient vehicles

Many countries agreed to significantly reduce CO_2 emissions by 2025. The values are normalised according to the NEDC [151]. Although CO_2 emission targets are set individually for different vehicle markets (e.g., China, European Union, Japan, USA), the trend toward low-emission vehicles is clearly noticeable.

targets for different countries normalised according to the *New European Driving Cycle* (NEDC). In 2009 the European Union sets mandatory emissions reduction targets for new cars [47]. After a 3-year phase-in ending in 2015, the entire new car fleet has to comply with an average CO_2 level of 130 g/km, a target level that is then reduced to 95 g/km for 2020. This corresponds to a fossil fuel consumption of 5.6 l/100 km of gasoline or 4.9 l/100 km of diesel in 2015 and 4.1 l/100 km (gasoline) or 3.6 l/100 km (diesel) in 2020, respectively. Failure to meet these targets results in penalty payments[2] for each vehicle registered. In 2012, the penalty was set at €5 for the first gram over the limit, with the penalty for subsequent grams increasing rapidly to €95 per gram (see Table 1.1). In 2019, this fee scale will be eliminated, and manufacturers will have to pay a flat fee of €95 for each and every gram in excess of the limit [47].

The mandatory regulation also supports OEMs building extremely low-emission vehicles (i.e., below 50 g/km CO_2). The registration statistics count such cars as multiple vehicles (i.e., *super credits*). Moreover, increasingly stringent emission laws will force car manufacturers to develop low-emission vehicles (see Figure 1.6). The emission law covers CO, HC, and NOx, and also strictly limits the mass (PM) and number of particulates (PN).

[2]This penalty payment is called *excess emissions premium*.

Table 1.1.: Penalties for CO_2 emissions in excess of limits, which must be paid for each car registered. Starting in 2019, there will be a flat fee of € 95 for each gram in excess of the limits [47].

Excess CO_2	**Emissions premium in €**
For 1st g/km	5
For 2nd g/km	15
For 3rd g/km	25
Each subsequent g/km	95

Table 1.2 shows the thresholds of the currently valid EURO 6 emission directive [140]. The introduction of catalytic converters and NOx traps are important contributions to the efficient reduction of emissions.

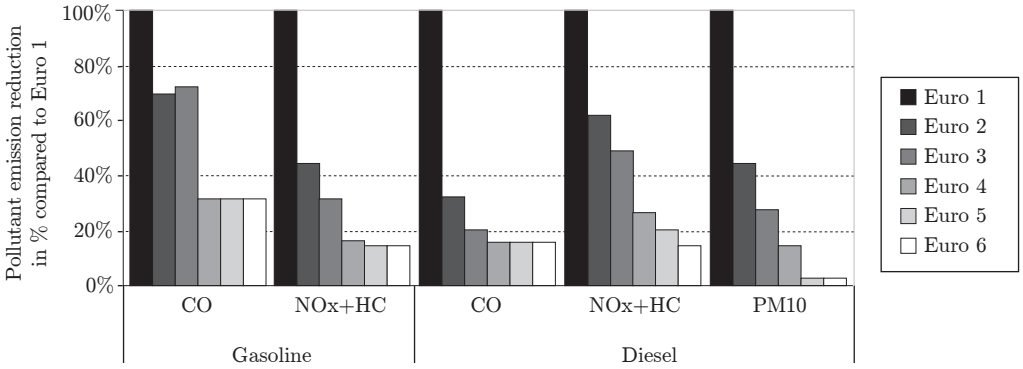

Figure 1.6.: Development of the European emission standard

The exhaust gas emission limits will be consistently tightened. Currently, the EURO 6 is valid. Compared to EURO 1, pollutant emissions have been reduced by more than 50 %. In recent years, especially the particulate matter (PM) has been drastically limited, particularly for diesels.

Since national taxation and statutory regulations differ from market to market, OEMs have to decide which national regulations have to be considered in the vehicle development process. A prioritisation can be done by using a CO_2 costs-market relevance analysis [118]. The following political measurements are related to the Austrian vehicle market.

When initially registering the vehicle, customers have to pay additional taxes (*Normverbrauchsabgabe*, NoVA, English: Austrian motor vehicle registration tax) [1]. This tax, which is strongly related to the overall CO_2 emissions of the corresponding vehicle, reads

$$\mathrm{NoVA} = \frac{\lambda_{CO_2} - 90}{5} \quad . \tag{1.2}$$

Table 1.2.: Thresholds of the European emission standard EURO 6 [140]

Emission limits	Unit	Diesel	Gasoline
CO	g/km	0.5	1.0
HC	g/km	-	0.1
NOx	g/km	0.8	0.6
HC + NOx	g/km	1.7	-
PM	g/km	0.0045	0.0045
PN	#/km	$6.0\,e^{10}$	$6.0\,e^{10}$

The NoVA is given in percentage and is added before VAT, with an upper limit of 32 %. For vehicles exceeding 250 g/km CO_2, the total costs increase by an additional €20 for each gram of CO_2. The average CO_2 emission is given by λ_{CO_2} in g/km. The total costs due to the NoVA are reduced by a fixed amount (in 2015: €400, thereafter €300 for all cars). No tax credit is possible [1].

Table 1.3.: Motor vehicle taxation in Austria for vehicles under 3.5 tons. The taxation is graduated and increases with increasing engine power. The values are based on a monthly rate and are valid for annual payment [5].

Power range in kW	Additional cost in €/kW/month
0-24	0
25-90	0.62
91-110	0.66
>110	0.75

In addition, the fuel consumption of ICEs is indirectly regulated by a mineral oil taxation. According to [2], the taxation is 0.482 €/l for gasoline and 0.397 €/l for diesel, for all fuel with a maximum total sulphur of 10 mg/kg and a predefined amount of biofuels. Moreover, customers have to pay a motor vehicle tax. In Austria, this taxation is directly linked to the motor vehicle liability insurance and depends on the overall ICE power [5]. Table 1.3 outlines the progressive costs.

1.2. Fuel Consumption Evaluation

The test procedure for evaluating the overall fuel consumption and exhaust emissions is statutory. The standard cycles vary by vehicle market. Europe currently uses the NEDC. Figure 1.7 shows the speed profile of the NEDC and its successor, the *worldwide harmonized light vehicles test procedure* (WLTP). Chapter 4.1 summarises the key characteristics of both driving cycles.

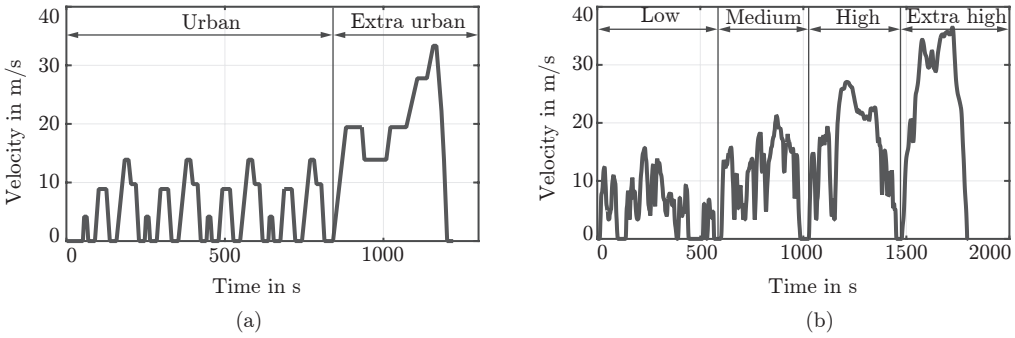

Figure 1.7.: European legal driving cycle

Figure (a) shows the currently valid driving cycle, the NEDC. Its successor, the WLTP class 3b, is shown in Figure (b). The WLTP is divided into power-to-mass ratio (PMR) classes. All vehicles with a PMR above 34 kW/t will be tested with the WLTP class 3b.

The tests are conducted on a chassis dynamometer under predefined operating conditions, in order to guarantee the reproducibility of the results. The real driving resistances in real-world test scenarios are first evaluated, followed by an adaptation on the chassis dynamometer [166]. The exhaust emissions are then collected in samples and evaluated via dilution equipment (CVS, constant volume sampler) [172]. These samples are used to evaluate CO_2 emissions. The overall fuel consumption $\bar{C}_{CI}$ is then calculated from the emissions of HC, CO, CO_2 [140]. For compression ignition (CI) engines, this formula reads:

$$\bar{C}_{CI} = \frac{0.116}{\rho_f} \left[0.749\lambda_{\mathrm{HC}} + 0.429\lambda_{\mathrm{CO}} + 0.273\lambda_{\mathrm{CO_2}}\right]. \tag{1.3}$$

In Eq. (1.3) λ_{HC}, λ_{CO} and $\lambda_{\mathrm{CO_2}}$ are the measured HC, CO, CO_2 emissions in g/km, and ρ_f is the density of the test diesel[3] fuel at 15 °C. This test procedure is adapted to HEVs and PHEVs.

PHEV legal fuel consumption evaluation

Plug-in hybrid electric vehicles are HEVs which can also be externally charged. Although short distances within the AER may be performed purely in electric mode, the ICE is mainly used for longer distances. Legislation seeks to account for that by using the relation stated in Eq. (1.4).

$$\bar{C}_{PHEV} = \frac{d_e\bar{C}_1 + d_{av}\bar{C}_2}{d_e + d_{av}}, \tag{1.4}$$

where $\bar{C}_{PHEV}$ is the overall fossil fuel consumption in l/100 km, $\bar{C}_1$ and $\bar{C}_2$ are the fuel consumption in l/100 km with fully charged or empty battery, respectively [140].

[3]For gasoline engines the coefficients are different, cf. [140].

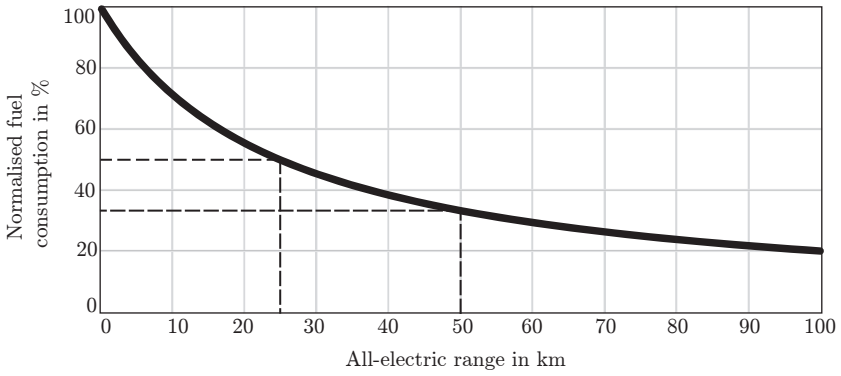

Figure 1.8.: Influence of the all-electric range on the fuel consumption of PHEVs [166]

The figure shows the normalised fuel consumption in % based on the fuel consumption of a conventional ICE-driven vehicle. An AER of 25 km results in a total fuel consumption reduction of 50 % compared to a conventional ICE-driven vehicle. An AER of 50 km leads to a significant reduction of 66.6 %.

The parameter d_{av} describes an average distance of 25 km between consecutive charging cycles, and d_e is the AER in km. The AER is defined by the distance in the legislative driving cycle before the ICE has to start the first time due to low battery power.

In Eq. (1.4), the fuel consumption $\bar{C}_1 = 0$ if the AER exceeds the total distance of the NEDC. However, this does not account for any electricity production costs. Car manufacturers may use this to reduce their vehicles' fuel consumption and the corresponding CO_2 emissions by scaling the energy content of the battery and thus the AER [166]. Figure 1.8 highlights the decreasing fuel consumption of PHEVs due to an increasing AER. For example an AER of 25 km reduces the fossil fuel consumption by 50 % compared to a conventional ICE-driven vehicle. This is an appropriate way to reduce the average CO_2 fleet emission level and avoid additional penalty costs.

HEV legal fuel consumption evaluation

The evaluated CO_2 emissions and the calculated fuel consumption are corrected by a function that considers the energy balance $\Delta E_{BAT} = 0$ at the beginning and end of the driving cycle [140]. The fuel consumption correction coefficient K_f in l/100 km/Ah is determined by

$$K_f = \frac{N \cdot \sum \Delta Q_i \bar{C}_i - \sum \Delta Q_i \sum \bar{C}_i}{N \cdot \sum \Delta Q_i^2 - (\sum \Delta Q_i)^2}, \tag{1.5}$$

where $\bar{C}_i$ and ΔQ_i are the fuel consumption and electricity balance – the difference of the battery's energy content at the end and beginning of the cycle – measured during the i^{th} test, and N is the total number of tests. The corrected fuel consumption $\bar{C}_{HEV}$ reads

$$\bar{C}_{HEV} = \bar{C} - K_f \cdot \Delta Q, \tag{1.6}$$

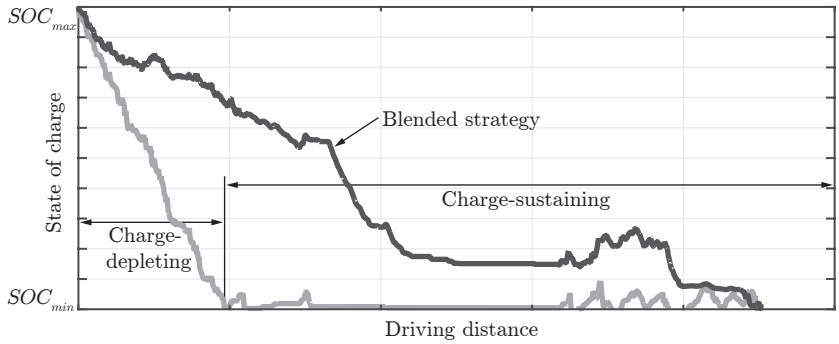

Figure 1.9.: Different operation modes for PHEVs

PHEVs operate in different operation modes. If the SOC is kept nearly constant, the PHEV operates in charge-sustaining mode. However, operating in either a combined charge depleting/sustaining mode or a blended operation strategy enables more fuel saving potential for PHEVs.

where $\bar{C}$ is the fuel consumption measured during testing in l/100 km, and ΔQ is the electricity balance measured during testing in Ah. The CO_2 emissions are corrected in a similar way, but instead of using the fuel consumption $\bar{C}_i$ and $\bar{C}_{HEV}$, the corresponding emission value λ_{CO_2} in g/km has to be inserted. The reason for such a test procedure is that the electric energy in this case always comes from the fossil fuel.

Fuel consumption evaluation in real-world traffic and simulation

There are two different approaches in the literature for evaluating the overall fuel consumption of HEVs and PHEVs. In simulations, HEVs are often operating in a *charge-sustaining mode* [61], [101]. In this case, the energy of the battery at the beginning and after a certain distance has to be equal. Using appropriate optimisation algorithms ensures the energy balance [12]. An equivalence factor is also used to transform the electric energy difference in fossil fuel consumption. However, finding an appropriate factor is a challenging task [190], since it depends on the driving conditions along the particular driving route and therefore must be adapted during real-time operation [183].

For PHEVs a *charge-depleting* operation strategy is more suitable [6], [61]. Assuming that the battery can be externally charged after each trip [59], the battery's energy content is expected to drop near to the lower state of charge (SOC) level (SOC_{min}). Such an operation strategy ensures improved energy efficiency. Figure 1.9 highlights the different SOC characteristics of PHEV operation strategies. Operating the PHEV in charge-depleting mode until the lower SOC threshold is reached and then operating in charge-sustaining mode results in improved fossil fuel consumption. However, a blended operation strategy for PHEVs enables additional fuel savings [214]. The innovative energy management strategy proposed here also uses such a blended operation strategy. Approaching the lower SOC threshold implies knowledge of the desired destination; otherwise, a deviation and an accompanying reduction in fuel consumption potential occur.

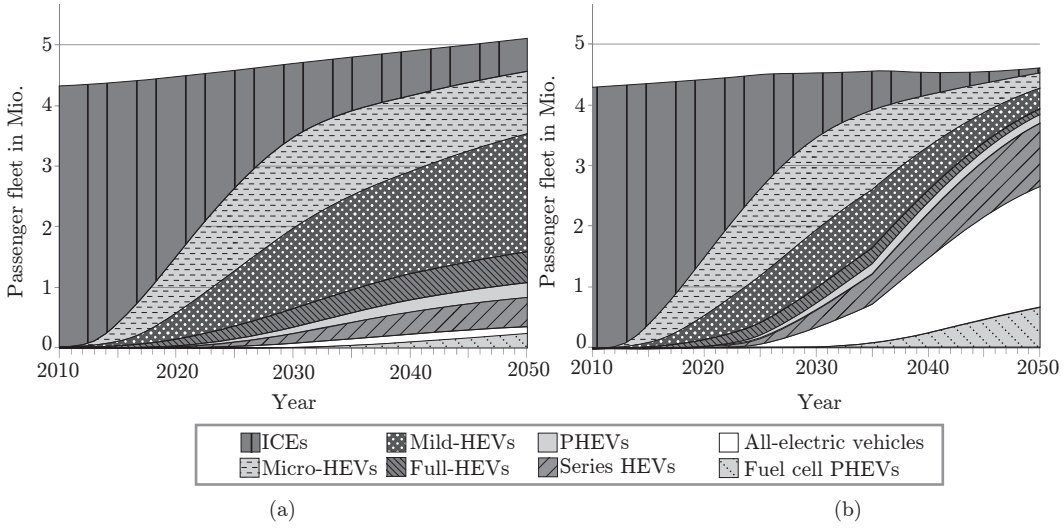

Figure 1.10.: Prognosis for the future Austrian vehicle fleet [3]

Figure (a) shows the future market shares assuming a low crude oil price and no additional legal interventions. Figure (b) illustrates the opposite scenario – high fossil costs and political interventions and subventions in favour of electrification.

1.3. Future Trend of Passenger Vehicle Electrification

The study *ELEKTRA* [3] highlights that the future market shares of different propulsion systems for passenger vehicles depend on crude oil costs and legal framework conditions. Figure 1.10(a) depicts the development of the total fleet of passenger vehicles in Austria with a low crude oil price and no additional political restrictions or subventions. Hybrid electric vehicles will significantly increase their market share and will form the core of the future fleet. In this scenario, full-HEVs increase to 10 %, whereas PHEVs and all-electric vehicles are unable to succeed in the long-term. Moreover, the overall fleet energy consumption and the GHG emissions decline [3].

Figure 1.10(b) emphasises that high future crude oil costs and additional political interventions in favour of electrification result in a different development. In the short-term, the conventional drivetrain is substituted by micro and mild HEVs[4]. Starting in 2020, PHEVs and all-electric vehicles gradually replace conventional drivetrains. Nevertheless, there are no significant market shares before 2025 [3]. In the long-term, the market shares of electrified vehicles with a high degree of hybridisation (DoH), cf. Chapter 2.1, grow to 85 %. Both overall energy consumption and GHG emissions will be significantly reduced by 2050 [3].

The two extremes highlight that micro and mild HEVs will penetrate the vehicle market regardless of economic and political boundary conditions. However, the competitiveness of highly electrified vehicles, such as PHEVs, series HEVs and all-electric vehicles, is

[4]Micro and mild HEVs have a rather low electric power and energy supply for the additional electric motor and battery, see also Chapter 2.1.

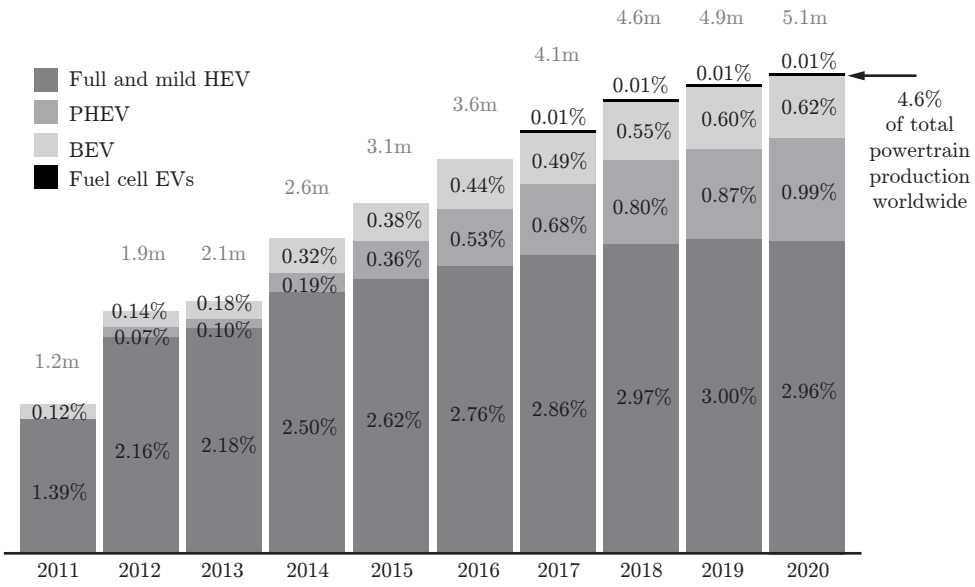

Figure 1.11.: KPMG's forecast of electrified powertrain production 2011-2020 [111]

In 2020 less than 5 % of the overall powertrain production volume will be HEVs. However, the survey respondents believe that PHEVs will generate the most consumer demand of highly electrified vehicles by the end of this decade [111]. However, mild and full HEVs will still have the biggest market shares among HEVs.

strongly dependent upon political interventions, such as tax advantages.

According to the *KPMG's Global Automotive Executive Survey 2015* [111], PHEVs will be the most in-demand electrified propulsion technologies in 2020 (see Figure 1.11). KPMG operates as a global network of independent member firms offering audit, tax and advisory services. More than 200 automotive executives from all parts of the automotive value chain, including OEMs, Tier 1, 2 and 3 suppliers, dealers, and providers of financial and mobility services, participate in this annual assessment of the current state and future prospects of the worldwide automotive industry. Battery electric vehicles (BEVs) remain in the number two position. However, optimising traditional fossil-fuel-based propulsion technologies is still the top priority of OEMs. Moreover, the survey highlights that fuel efficiency is clearly seen as the number one purchase criterion in 2020.

A more optimistic study [180] estimates the global share of HEVs between 16-20 %, depending on the costs of fossil fuel. Once again, the PHEV is seen as a promising technology. The market shares of PHEVs and all-electric vehicles will be between 1-9 % in 2020.

1.4. Structure of the Thesis

The present research focuses on the development of an operation strategy for plug-in hybrid electric vehicles. The hypothesis of the present research is that an intelligent

combination of route prediction and adaptation to the individual driving style in the long-term may simultaneously increase the overall fuel efficiency and the longitudinal vehicle dynamics of HEVs, thus resulting in higher consumer acceptance and increased market shares. The structure of this thesis is as follows.

Chapter 2 describes the state-of-the-art of HEVs and PHEVs in detail. First, HEVs are categorized according to their functions and power capability. Furthermore, different HEV drivetrain topologies with corresponding mass-production vehicles are presented. Next, the state-of-the-art of HEV and PHEV operation strategies is explained. Three main types are depicted: rule-based, optimal and suboptimal operation strategies (OSs). The chapter closes with the main scientific contributions of the present thesis.

Chapter 3 introduces the methodology. It consists of three main parts: modelling, optimisation, and prediction & adaptation (P&A). First, two different vehicle modelling approaches are described, and detailed information about HEV drivetrain component modelling is then provided. At the end of this part, an innovative energy management controller for PHEVs is proposed, and the main characteristics of the investigated vehicle are described. The chapter continues with an explanation of the main structure of the optimisation algorithm. *Dynamic programming* (DP) is used to solve the optimal control problem. The author highlights the fundamental concepts of the optimisation method and explains the implementation issues in detail, such as approximation, computational effort and performance. The methodology concludes with an introduction of the innovative P&A algorithms used to approximate future power demand, whereby prediction is based on static information from digital maps. The vehicle position is evaluated with *global navigation satellite system* (GNSS) signals, such as *global positioning system* (GPS)[5], *global navigation satellite system* (GLONASS)[6], *Galileo*[7] and *Beidou*[8]. Subsequently, the static prediction is adapted to the individual driving style. The integration of the driver's particular driving behaviour with static road data enables additional fuel saving potentials in the long-term.

Chapter 4 discusses the results of numerical simulations of the proposed innovative operation strategy. The fuel saving potential is explicitly determined with a real-world driving cycle (FTG cycle), recorded in the area of Graz, Austria. In addition, the author compares the real-world driving cycle used and the legally stipulated driving cycles. The controller stability to parameter variations is then analysed. The chapter concludes with a discussion of the fuel saving potential and other positive effects (e.g., enhanced longitudinal vehicle performance and increased electrical propulsion system availability), as well as the cost impact for OEMs and customers.

Chapter 5 presents the key findings and a final statement about this research.

[5]Global navigation system originally developed by the U.S. Department of Defense
[6]Global navigation system used by the Russian Aerospace Defence Forces
[7]Global navigation system of the European Union
[8]Global navigation system of China

2

State-of-the-Art Hybrid Electric Vehicles

2.1. HEV Classification

According to standards ECE-R83 [140] and SAE J1715 [88], an HEV is a means of transport that consists of at least two different on-board energy converters, as well as two different energy storage systems (ESSs). Hybrid electric vehicles combine the advantages of two drivetrain designs. That is, they have an ICE for long-distance travels, and can drive short distances "locally emission-free" with the electric propulsion system (i.e., the vehicle itself produces zero-emissions).

Besides the long-distance capability and the possibility of locally emission-free driving, there are numerous technical benefits depending on the operation modes implemented, the system power performance and the drivetrain layout.

The application and usefulness of different operation modes are affected by the component and system layout. A distinction can be made with the DoH, which reads [14]

$$\mathrm{DoH} = 1 - \frac{|P_{EMG,max} - P_{ICE,max}|}{P_{EMG,max} + P_{ICE,max}} \tag{2.1}$$

where $P_{EMG,max}$ and $P_{ICE,max}$ are the rated electric motor/generator (EMG) and ICE power, respectively. Figure 2.1 shows the relation of the DoH according to the definition in [14]. In a conventional drivetrain $P_{EMG,max} = 0$, and consequently the DoH is also 0. The same holds for an all-electric vehicle. If $P_{ICE,max} = P_{EMG,max} \neq 0$, the DoH is 1.

The present research uses a more straightforward definition of the DoH defined in [66]

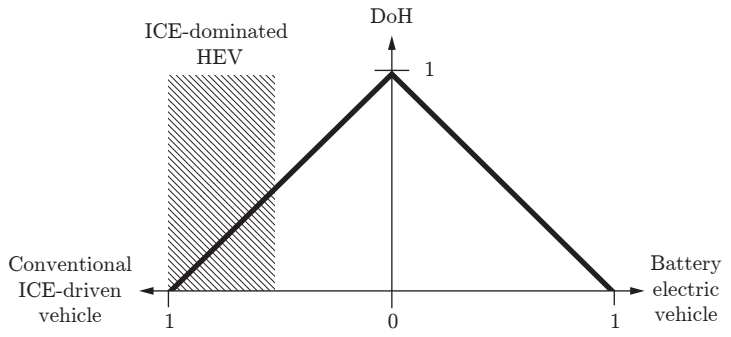

Figure 2.1.: Definition of the degree of hybridisation (DoH) [14]

In conventional drivetrains ($P_{EMG,max} = 0$) and all-electric vehicles ($P_{ICE,max} = 0$), the DoH is zero; otherwise, the DoH is calculated using Eq. (2.1) and is greater than zero.

and [81]:

$$\text{DoH} = \frac{P_{EMG,max}}{P_{ICE,max} + P_{EMG,max}}. \tag{2.2}$$

Figure A.1 also shows a classification of HEVs by their DoH and battery capacity. Depending on the required voltage range and the modification level of the drivetrain, different power levels can be defined [169]. The availability of certain hybrid functions is strongly related to the DoH (see Figure 2.2). Based on the electric system capability, HEVs are categorised as:

- Micro-HEV
- Mild-HEV
- Full-HEV
- Plug-in HEV (PHEV)

Figure 2.2 shows the different available hybrid functions for different HEV performance classes. For a micro and mild HEV, ICE start/stop is available. All other hybrid functions are limited, and pure electric driving is not possible. A mild-HEV has a voltage level up to 200 V to increase the effectiveness of certain operation modes. However, e-drive is still not possible. In a full-HEV, all hybrid functions are available with no limitation. In HEVs the on-board energy comes from fossil fuel, while PHEVs offer additional possibilities. A PHEV is in principle a full-HEV with a larger ESS (10-20 kWh) and the additional option of recharging via external outlets. Consequently, PHEVs share the characteristics of both an HEV (i.e., a battery, electric motor (EM), and ICE) and an all-electric vehicle (e.g., a plug to connect to the electrical grid). One logical application of PHEVs is commuting within a short distance, whereby the AER is between 20-50 km [23], [34]. However, the main technical challenges for PHEVs are improving the ESS capacity of the Li-ion batteries and reducing costs [126].

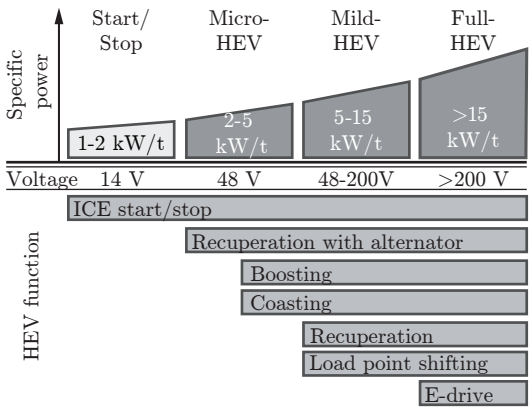

Figure 2.2.: Classification of HEVs according to their DoH, adapted from [23], [169]

Depending on the power capability of the electric traction components, different HEV functions, such as recuperation, boosting, and e-drive, are available. Only highly electrified HEVs, e.g., full-HEVs and PHEVs, enable all HEV functions.

2.1.1. Operation Modes

Hybrid electric vehicles take advantage of several different operation modes, which enable additional fuel savings and thus reduced GHG emissions. In general, there are different operation modes available, depending on the capability of the electric traction system and the drivetrain layout. The implementation and precise function definition depend on the corresponding OEM.

ICE start/stop

The start/stop function turns off the ICE when the vehicle stops or shortly before in the braking phase at quite low speeds. The logic accounts for multiple factors, such as the electric power demand of the auxiliaries (AUXs), temperatures of the ICE, the catalytic converter and energy content of the starter battery, in order to ensure a proper and comfortable operation of the vehicle [23]. Moreover, this feature is often combined with an intelligent control of the alternator, where the low-voltage battery is charged while braking, thereby enabling additional fuel saving and increased vehicle performance, since the ICE has to load the battery only on demand [39]. BMW introduced a combination of different technologies to save fossil fuel called *EfficientDynamics*, which includes such an intelligent control of the alternator, among other factors [117]. The prerequisite for switching off the engine while braking is that the main auxiliaries are electrified.

Coasting

Coasting is another method to improve the energy efficiency of the overall vehicle. While free rolling (i.e., not using the accelerator pedal), the ICE is disengaged by a clutch and eventually switched off. Auxiliaries such as the power steering pump, brake booster, heating and air conditioning (A/C) have to be partially electrified. Moreover, the capability of the on-board battery has to be adapted. The authors in [138] distinguish between coasting with ICE in idle (idle-coasting) and coasting with a deactivated ICE (start/stop-coasting). The definition and implementation of this mode depend on the particular OEM [173]. However, using the author's own nomenclature, three categories can be identified:

- *Passive coasting*:
  The ICE is disengaged, and there is no additional EMG torque [26], [51], [107]. Only the driving resistances are acting.
- *Constant-speed coasting*:
  The ICE is decoupled, and the EM supplies traction to maintain a constant driving speed [173].
- *Active coasting*:
  The EMG reproduces the ICE drag torque [10], [169]. The electric power generated is used to charge the battery.

E-drive

This operation mode enables the vehicle to drive fully electrically and to operate with low-noise and zero local emissions (i.e., the vehicle itself produces zero-emissions while driving). However, the performance depends on the system configuration. A high-power EM application is able to provide sufficient traction power over a wide operation range, whereas a low-power design is only active during nearly constant speed with low acceleration. A proper implementation requires independent and fully electrified auxiliaries.

Boosting

The hybridisation of conventional drivetrains enables concurrent utilisation of the power of both propulsion units for specific HEV topologies. This mode results in increased longitudinal vehicle performance, as long as the SOC level does not drop below a certain lower threshold.

Recuperation

Implementing an EMG enables recuperation[1]. When the brakes are applied, the EMG converts a portion of the vehicle's kinetic energy to electrical energy, and the remaining energy is then dissipated as heat through the conventional hydraulic brake system. The recuperative potential and additional fuel savings depend on the driving style and the HEV design [23]. Furthermore, reducing the aerodynamic drag and rolling resistance increases the effectiveness of regenerative braking. An additional brake force controller ensures an appropriate brake power distribution.

Load point shifting

Instead of operating in low load areas, the ICE is forced to produce excess power, which is concurrently used to load the ESS via the electric generator (EG). Load point shifting results in improved ICE operating efficiencies. The stored energy is used to propel the vehicle on the upcoming driving profile, which enhances the overall fuel efficiency. In the case of an almost fully charged ESS, load point shifting to lower loads is not reasonable [23]. An efficiency-optimised operation strategy requires the consideration of the entire energy conversion chain [169]. The objective is to charge the battery at low fossil fuel costs and reuse the stored energy with high efficiency. For HEVs with no external charging possibility (also called *autarkic* HEVs), load point shifting is an effective measure to enhance the overall operating efficiency.

Phlegmatisation

The ICE/EG unit may be disconnected from the drivetrain by a clutch, which enables operation with rotational speed independent of the rest of the drivetrain. Hence, it can operate in a steady-state in operation areas with high ICE efficiency. This operation mode is called phlegmatisation of the ICE. In addition to enabling operation close to the optimum load point, the exhaust emissions can also be reduced [169]. Furthermore, the different dynamic response of both propulsion units – ICE and EMG – can be used to increase the response characteristics of the entire drivetrain. The EMG has the ability to generate positive torque in a shorter time period than the ICE, due to its almost immediate response. Consequently, peak loads of the ICE can be avoided by balancing the volatile change of demanded driving torque with the EMG. The ICE can then be readjusted slowly, with low fuel consumption and raw exhaust emissions [23]. The almost instantaneous EMG response not only increases the overall longitudinal vehicle dynamics but also the driving pleasure of passengers.

Moreover, other vehicle control systems can profit from the rapid response time, such as electronic stability program (ESP) [164]. In [164], the author developed a vehicle

[1] Also called regenerative braking [169]

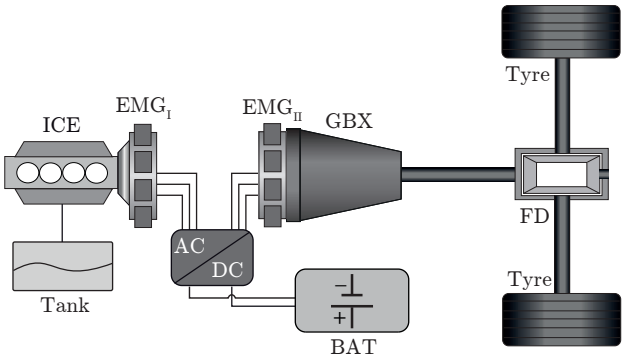

Figure 2.3.: Schematic representation of a series HEV, adapted from [169]

The ICE is directly connected to the EMG_I, which operates as an EG, and there is no mechanical link to the drive shafts. A second EMG_{II} provides all necessary traction. Besides the gearbox (GBX), a battery (BAT) and AC/DC power converter (AC/DC) are parts of the HEV's drivetrain.

dynamics controller combining the conventional hydraulic friction brake system with independent wheel hub motors. This guarantees that most of the vehicle dynamics control actions are performed by utilizing electric traction machines. Consequently, the almost immediate response of the EMG can enhance the brake response.

2.1.2. HEV Drivetrain Layout

Besides the classification by function, HEVs can also be categorised based on the arrangement of the ICE, EM(s), EG(s), and gearbox (GBX). In general, there are three different hybrid drivetrain concepts.

Series hybrid electric vehicle

In series HEVs, the ICE is directly connected to an EMG_I operating mainly as an EG (see Figure 2.3). The electric energy produced is either stored in a battery (BAT) or directly used for propulsion. An additional EMG_{II} provides all necessary propulsion power. Furthermore, there is no mechanical connection between the ICE and the drive shaft. This mechanical decoupling allows the ICE to operate in a steady-state in high-efficiency areas, resulting in low fossil fuel consumption and emissions [169]. Nevertheless, the need for multiple energy conversions due to the long efficiency chain is a disadvantage. The system can compensate for the resulting losses if the engine is operating at its best operation point and a relatively high driving dynamics is predominant [23], such as permanent stop-and-go traffic in cities. The electric traction motor is solely responsible for the traction and the maximum speed. Consequently, its dimensions have to be adapted to the desired performance, which increases costs and technical effort [23]. This

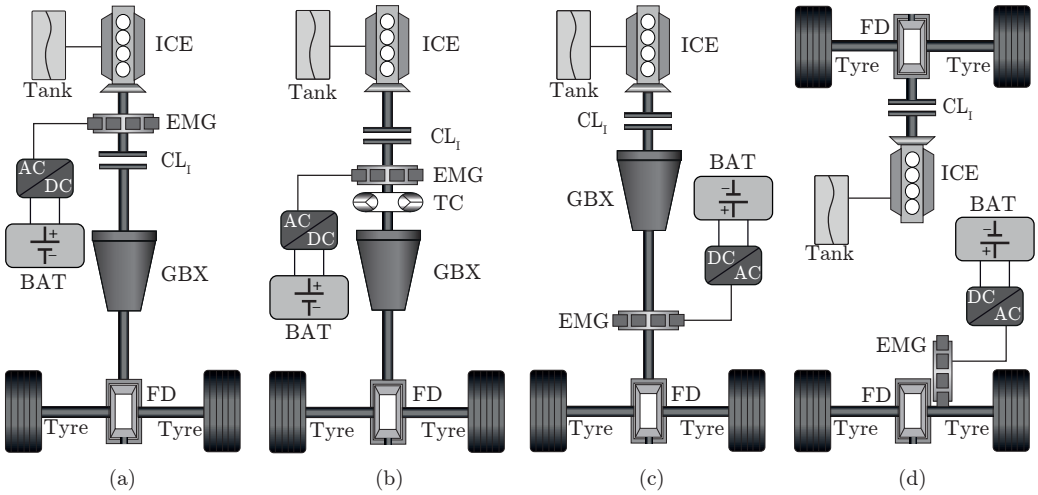

Figure 2.4.: Schematic representation of different parallel HEVs, adapted from [169]

There are different variations depending on the arrangement of the EMG in the drivetrain. From left to right, a P1-HEV (a), a P2-HEV (b), a P3-HEV (c) and a P4-HEV (d) are shown. The conventional drivetrain consisting of internal combustion engine (ICE), clutch (CL), gearbox (GBX) and final drive (FD) is extended by a battery (BAT), an AC/DC power converter (AC/DC) and an electric motor/generator (EMG). A torque converter (TC) can also be integrated.

topology is suitable for independent wheel hub motors or near-to-the-wheel motors [169]. Since the ICE is no longer subject to the driver's widely varying power demands, the ICE can be built smaller than the EM [126]. The BMW i3 with range extender (REx) [38], [197] is a currently available PHEV with series configuration and one central EMG at the rear axis to drive the wheels.

Parallel hybrid electric vehicle

The main characteristic of parallel HEVs is that both the EM and ICE are mechanically connected to the drive shaft. The EMG can be connected or disconnected when required. The relatively modest and cost-efficient assembly is beneficial. Depending on the drivetrain layout, the overall system power is achieved by adding either speed, torque or traction. According to [23], [169], there are different parallel drivetrain variations, depending on the arrangement and dimensioning of the EMG. The relevant nomenclature is based on [169] (see Figure 2.4).

Parallel-1 Hybrid Electric Vehicle (P1-HEV)

Figure 2.4(a) shows a P1-HEV. The EMG is directly driven by the crankshaft. The degree of modification of the conventional drivetrain is low. The EMG is mounted between the ICE and the clutch CL_I. This configuration enables start/stop, recuperation, load point shifting and boosting, but pure electric driving is limited. However, the recuperation potential is reduced by the ICE drag, due to the fixed connection. The Honda Insight Hybrid with integrated motor assist (IMA) [9] was the first HEV with a P1 topology. A currently available example is the Mercedes-Benz S400 Hybrid [202]. In [196], two different P1 topologies are discussed – a belt-driven starter generator (BSG) and an integrated starter generator (ISG). The BSG is integrated in the belt drive of the ICE, resulting in an easy drivetrain integration (cf. Figure A.2(a) in Appendix A). However, the system packaging is increased, and this configuration requires an additional 12 V starter for cold starts and a special belt tensioner to ensure good power transfer between ICE and BSG (cf. Figures A.2(b) and A.2(c) in Appendix A). The ISG configuration is directly mounted on the crankshaft between the ICE and the GBX (see Figure A.3 in Appendix A). The direct power transfer enables higher performance and eliminates the need for a 12 V starter at low temperatures [196]. Both BSG and ISG operate with a 48 V HEV system. Typically, the power is below 20 kW, and the battery energy content is below 2 kWh, thus placing such vehicles in the category of mild-HEVs.

Parallel-2 Hybrid Electric Vehicle (P2-HEV)

In Figure 2.4(b), the EMG is installed between the ICE and the GBX. A clutch CL_I between the EMG and the ICE enables independent driving of the EMG. The ICE is either started by a conventional starter or by a predefined activation of the clutch [23]. There are variations with and without an additional converter clutch. In the first variant, the EMG replaces the torque converter (TC), and an additional starter is used to tow-start the ICE without power sag [169]. The BMW ActiveHybrid5 [64], the Mercedes-Benz E 300 BlueTec Hybrid [97], the Mercedes-Benz S500 Plug-In Hybrid [96] and the Mercedes-Benz C350 Plug-In Hybrid [98] are examples of this configuration. The variation with a TC clutch is applied in the Porsche Panamera S E-Hybrid [23], [185], the Porsche Cayenne S E-Hybrid, the VW Touareg Hybrid [26], the BMW X5 eDrive Plug-In [10] and the Audi Q7 e-tron 3.0 TDI quattro [107]. In this approach, an additional starter is not needed [169]. All HEV operation modes can be realised, including regenerative braking without ICE drag losses. Implementing a second clutch enables battery charging during standstill [169]. One design approach is that the EMG can cover low-efficiency areas of the ICE, such as partial-loads [23]. A P2 layout typically has an EMG power in the range of 20-50 kW and an ESS capacity of about 2 kWh [169].

Parallel-3 Hybrid Electric Vehicle (P3-HEV)

In this arrangement, the EMG is mounted after the GBX and before the final drive (FD), as shown in Figure 2.4(c). Gear-shifting without traction interruption and no additional losses in the gearbox are advantages of this configuration. Moreover, regenerative braking efficiency is maximised due to the physical location. A conventional starter enables start/stop. However, the EMG has to operate in a wide rotational speed range, resulting in low gear ratios and thus a low torque level during start-up [23]. This may be one reason why such a drivetrain topology is not widespread in the industry. Almost all HEV functions can be easily implemented, except load point shifting [169]. Moreover, integration in a conventional drivetrain is straightforward. Typically, the EMG power range is 20-50 kW [169].

Parallel-4 Hybrid Electric Vehicle (P4-HEV)

This HEV topology has two independently operating drive axles. In Figure 2.4(d) the front axle is driven by a conventional ICE, while an EMG operates at the rear axle. The relatively low effort of modification [169] and the temporarily available all-wheel drive (AWD) are benefits of this topology. Nevertheless, load point shifting is not possible [169], and the availability of the AWD is limited by the restricted battery energy content. Moreover, a conventional starter is needed to enable start/stop function, and battery charging during standstill is not possible. Recently, Volvo introduced a diesel PHEV with a P4 drivetrain layout [197]. Other examples include the Peugeot 408 Hybrid and the Peugeot 3008 Hybrid4 [23]. The BMW i8 combines an ICE-driven rear axle with 6-speed automatic transmission and an electric front axle, including a 2-speed transmission [38].

Variations of parallel hybrid electric vehicles

Figure 2.5 shows two variations of the conventional parallel HEV layout. Combining two individual parallel topologies by integrating at least two EMGs enables more flexibility. For instance, a P12 combines a P1 and a P2 drivetrain layout [169]. The P12-HEVs combine series and parallel HEV topologies in one drivetrain. One EMG_I, mainly operating as an EG, is directly connected to the ICE, as shown in Figure 2.5(a). A second EMG_{II} provides the traction torque. The HEV operates in series operation mode if the clutch CL_I between the ICE and gearbox is disengaged. The power of the ICE is used to provide electric energy via the EG. Moreover, the EG can tow-start the ICE. At higher loads, the clutch is engaged, and the ICE has a direct connection to the wheels. The vehicle operates in parallel operation mode and thus avoids multiple conversion losses in series mode. Load point shifting and boosting are possible. HONDA recently introduced such a concept with the Accord Hybrid [148]. Another parallel topology is the parallel torque-split (PTS). This side-by-side hybrid enables the operation of the two propulsion

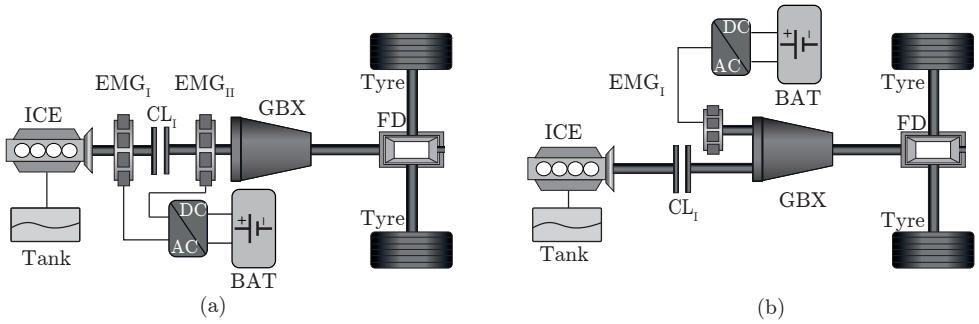

Figure 2.5.: Schematic representation of variations of parallel HEVs, adapted from [169]

Figure (a) shows a P12-HEV, which combines the functions of a P1 and P2 layout. Depending on the state of the clutch, either series or parallel mode is activated. Figure (b) shows a parallel torque-split (PTS) configuration, which allows for the combination of both traction torques at different speed levels. The conventional drivetrain consisting of ICE, clutch (CL_I), gearbox (GBX) and final drive (FD) is extended by electric motor/generators (EMGs), a traction battery (BAT) and an AC/DC power converter (AC/DC).

units at different speeds, cf. Figure 2.5(b). The advantages are the low modification effort and no interruption of the traction power during gear-shifting [169].

Power-split hybrid electric vehicle

At least one planetary gear-set (PGS) is used to distribute the mechanical power of the ICE to both the electrical and mechanical power paths. The electrical path consists of two EMGs and, in combination with the PGS, represents an electrical continuously variable transmission (eCVT), as shown in Figure 2.6. Consequently, given a demanded traction power, the operation strategy determines an efficient operation point for the ICE by actuating both EMGs. Depending on the power of all propulsion units, all operation modes can be realised. The advantages of a power-split HEV are the high flexibility in selecting an appropriate ICE operation point, the reduced overall conversion losses in the electric power path, and the elimination of the conventional gearbox and clutch [169]. This topology allows for tow-starting the ICE, and an additional starter is not required. Nevertheless, system complexity and control effort, vehicle weight and system costs increase [169]. The rather high reactive power in the electrical path is also a drawback (cf. Figure A.4 in Appendix A). In an input-split (L1-In), as shown in Figure A.5, the mechanical path is between the ICE and the ring of the PGS. Figure A.6 shows an output-split (L1-Out), where the mechanical path is between the planetary carrier and the FD [169]. Consequently, in an L1-In, one EMG is directly connected to the output axle, while in an L1-Out, one EMG is connected to the input shaft. A combination of both is called a compound power-split, where two PGSs are integrated together with two EMGs [169], cf. Figure A.7. In 2005 BMW, Chrysler, Daimler and GM [31] introduced a

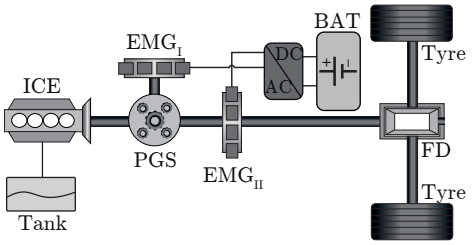

Figure 2.6.: Schematic representation of a power-split HEV

The mechanical power of the ICE is distributed via a planetary gear-set (PGS) to both a mechanical and electrical power path. The electrical path consists of two EMGs and, in combination with the PGS, represents an electrical continuously variable transmission (eCVT). The battery (BAT) is used for energy storage.

mutually developed two-mode HEV into their respective vehicles. It combines an L1-In split (i.e., for driving at slow speed and loads) with a compound power-split (i.e., for driving on rural and highway roads). Moreover, due to the combined actuation of two additional clutches and brakes, an eCVT with 4 fixed gear ratios for pure ICE drive can be realised. This complex system results in lower power flows in the electrical path and thus reduces efficiency losses. Currently available power-split HEVs include the Opel Ampera and the Chevrolet Volt, which are based on similar drivetrain layouts [63], as well as the Toyota Prius [146], [176].

2.2. HEV Operation Strategy

The supervisory control strategy of HEVs is a key success factor for outstanding fuel savings, enhanced longitudinal vehicle performance and a high level of safety and comfort. The main objective of an operation strategy (OS) is to distribute the demanded driving power optimally among all propulsion units. Developing efficient control algorithms for HEVs and PHEVs constitutes a challenging task and has been the focus of research and development in recent years [183]. The remainder of this chapter gives an overview of the widespread state-of-the-art operation strategies for different HEV topologies in recent years. In literature, there are three main groups of control strategies to optimise fuel economy:

- Rule-based (RB) operation strategy
- Optimal operation strategy
- Suboptimal operation strategy

Rule-based operation strategy

In RB-OS, also known as *heuristic* operation strategies, the power is distributed between all propulsion units with predefined rules and correlations based on the engineering knowledge of experts. These strategies account for certain vehicle states, such as the battery's SOC and the temperature levels of different components. In principle, heuristic operation strategies often ensure high engine operating efficiency by avoiding less efficient operation points [170]. In these unfavourable regions, the EM provides the traction torque. Load-levelling enables ICE operating efficiency near its peak value by additionally increasing the demanded power. The excess engine power is then shifted to load the battery [14]. A second control task is to keep the battery SOC within its desired limits. In [170] the battery is recharged when the energy content of the battery drops below a certain limit. If the SOC exceeds a certain upper threshold, the EM is used more often. In [68] a schematic set of rules is presented, which are inherent to rule-based operation strategies:

- Pure electric drive at low speed, low power demand and a high SOC-level
- Pure ICE drive at high speed and higher torque request
- Supporting the ICE with the EMG (known as boosting)
- Charging of the battery at low SOC levels (known as load point shifting)

The thresholds strongly depend on the SOC level of the battery. At lower levels the recharging operation area is adapted in order to increase the energy content of the battery. The main benefits are the real-time capability and the robustness in different driving situations.

In [122] an RB-OS for trucks is improved by analysing the optimal results of DP. The author in [89] introduced an energy management controller, the rules of which are based on the power demand, the driver's acceleration command and the SOC. This should ensure that vehicle components operate at high efficiency by avoiding high power losses.

Furthermore, heuristic operation strategies are the foundation of *fuzzy logic* energy management controllers. Fuzzy logic is the generalisation of the *Boolean logic*, which only permits conclusions which are either false (0) or true (1), so-called *crisp sets*. However, fuzzy logic systems (FLSs) allow truth values within the interval [0 1], thus enabling partial truth values (see Figure B.1 in Appendix B). Such *fuzzy sets* are characterised by *membership functions*, which assign a degree of membership to a certain input [198]. The membership function of such a fuzzy set may reach arbitrary values within the normalised closed interval of [0 1]. Figure B.2 shows a schematic example of such a membership function in detail. The corresponding membership functions are defined by experts [14]. In general, since the input variables of an FLS belong to crisp sets, a transformation to fuzzy sets is necessary. Afterwards, the degree of membership has to be translated back to crisp sets again, in order to obtain crisp outputs. One advantage of FLSs is that they can be designed without exact knowledge of the plant [7]. For detailed information, refer to subject-specific technical literature [7], [217].

In [116], [208] and [209], a fuzzy-logic-based energy management agent is proposed, which is able to assess the current vehicle state and driving conditions by extracting information through on-line driving cycle analysis. The fuzzy logic controller consists of four main components designed to extract the driving information, identify the driving style and distribute the demanded power in an efficient manner while maintaining the energy content of the battery. Other fuzzy-logic-based operation strategies are proposed in [14], [170], [177]. These strategies focus on the improvement of the overall drivetrain efficiency. Load-levelling is applied to shift the ICE operation within its peak efficiency area.

The fuzzy logic controller implemented in [70] accounts for both future path information and the battery state of health (SOH). The *predictive* and *protective* algorithm [70] selects an appropriate battery mode according to the additional information obtained by GPS.

Due to the intuitive selection of operation modes, rule-based and fuzzy-logic-based OSs are widespread in automotive research [215]. However, heuristic energy management controllers may not completely realise the optimal fuel economy [61] because real driving cycles differ from the artificial driving cycles used to create these rules.

Optimal operation strategy – Off-line optimisation

Optimal OSs based on global optimisation algorithms have been used for research and development purposes for years. Global optimisation methods assume that the entire driving cycle and route information are fully known a-priori. However, a perfect knowledge of the future driving profile is rarely available in practice due to unexpected traffic situations, such as traffic congestion and accidents. Nevertheless, methods such as dynamic programming (DP) [15] are often used as performance benchmarks for real-time-capable operation strategies [183]. Although DP can deal with non-linear and non-convex optimisation problems [101], the computational effort increases with the number of state and control variables (cf. Chapter 3.2.5). However, the generated solution is guaranteed to be the optimal solution [68].

The publication series [214], [215] and [216] investigated the potential of route-preview and a real-time implementation with the help of the instantaneous optimisation method *equivalent consumption minimisation strategy* (ECMS). Deterministic dynamic programming (DDP) is used as a performance benchmark, as well as to determine an equivalence factor. A detailed discussion on ECMS follows later. Two different series PHEV operation strategies are compared in [157] using DDP. One strategy has no restriction on engine fuel usage, while the second strategy limits the engine operation mode only after the SOC drops below a certain threshold.

In contrast, *stochastic dynamic programming* (SDP) is capable of deriving an optimal solution for a large group of driving cycles by minimizing the expectation of some cost functional (e.g., fuel consumption). In [123], the power demand from the driver is mod-

elled as a Markov chain[2]. A Markov chain is a random process whereby the conditional probability of a state at any time in the future depends only on the probability of the previous state and not on the sequence of events that preceded it, as shown in Eq. (2.3):

$$\hat{\mathcal{P}}(X_{k+1} = \alpha_{k+1}|X_k = \alpha_k, ..., X_0 = \alpha_0) = \hat{\mathcal{P}}(X_{k+1} = \alpha_{k+1}|X_k = \alpha_k), \tag{2.3}$$

where $\hat{\mathcal{P}}(X_{k+1} = \alpha_{k+1}|X_k = \alpha_k, ..., X_0 = \alpha_0)$ and $\hat{\mathcal{P}}(X_{k+1} = \alpha_{k+1}|X_k = \alpha_k)$ are the conditional probabilities of a sequence of random variables X_0, X_1, ..., X_k, which describe the state of the system at time steps 0,1,..., k, respectively, and α_k is the state variable of the random process at time step k. The optimal control strategy is determined by using SDP. For a given route, the obtained control law can be directly implemented. In [92], the stochastic properties of a certain route are used to assess the fuel saving potential of HEVs by incorporating information from GPS and traffic-flow information systems. To this end, a Markov process is configured with speed data of the certain route. Similar research [137] has used a probabilistic distribution of driving cycles to optimise the PHEVs power-split. The method evaluates the most probable future power demand based on the current vehicle speed with a Markov chain. Furthermore, it accounts for the trade-off between fuel and electricity costs by using an appropriate formulation of the cost functional of the optimisation problem. The authors of this publication propose the implementation of a static probability map that enables real-time implementation without requiring knowledge of the entire driving cycle a-priori. The probability of the next power-split could be estimated with the help of the current vehicle speed and acceleration, for example.

Another global optimisation approach, the *Pontryagin's minimum principle* (PMP), is used in [35], [99], [182] to solve the optimal control problem of HEVs. In addition to the fuel costs, the author in [186] also considered battery ageing by applying a damage accumulation model. The battery ageing is based on the SOC and charge/discharge rates.

The study in [168] also proposed an energy management controller using PMP. When accounting for all state and control variable constraints, it was not possible to find an analytic solution.

Suboptimal operation strategy – On-line optimisation

The main drawback of global optimisation methods is that the entire driving cycle has to be known a-priori. The ECMS reduces the optimisation problem to an instantaneous minimisation of an equivalent fuel consumption [155], [182], [183]. An equivalence factor is used to convert battery power to an equivalent fuel power, which must be added to the actual fuel power. Its estimation is the most critical aspect of ECMS and a key factor for obtaining good performance [35]. In general, the equivalence factor depends on the

[2] Also called Markov process. For detailed description refer to subject-specific technical literature such as [65].

driving conditions along a certain route [183]. It is evaluated either with past driving conditions [139], past and present driving [35], [100], or past, present and future driving conditions [68], [139], [159], [214].

To ensure improved fuel efficiency with charge-sustaining mode, some approaches [35], [100], [155] adapt the equivalence factor to the instantaneous deviations of the SOC from its target value. In [102] the ECMS strategy is also adapted to a possible change of the vehicle mass. In [42] the ECMS control scheme is augmented by the battery SOH. The equivalence factors are adapted online with a simple proportional-integral (PI) controller. The study shows a significant trade-off between fuel economy and battery wear.

Numerous studies have proven that additional information about the route ahead improves the overall fuel efficiency [10], [96], [157], [214], [216]. Due to the recent development of *intelligent transportation systems* (ITSs) based on GNSSs and *geographical information systems* (GISs), multiple authors have incorporated these additional information sources in the operation strategies of HEVs and PHEVs. For instance, in the work of [25], [59], [60] and [61], an OS for PHEVs based on DP and trip-modelling is introduced. If any historical or real-time traffic data from roadside sensors are available, a simplified prediction algorithm using speed limits and constant acceleration and deceleration rates, independent of the driving style, is applied.

For PHEVs a SOC drop to the lowest possible level at the end of the trip is desirable to improve the overall fuel efficiency. This has led many researchers, such as the author of [91] and [190], to develop multi-level energy management controllers. In [190] a traffic-data-enabled predictive control framework based on a supervisory battery SOC planning level and a lower level short-term velocity estimator is proposed. The high-level SOC planning integrates real-time traffic data obtained from roadside sensors in order to improve the overall fuel efficiency. The authors in [91] introduced a similar approach for the efficient control of PHEVs. A high-level on-line stochastic optimisation based on real-time traffic information determines the optimal SOC trace. The low-level controller operates off-line and determines the optimal power distribution based on historical driving cycles.

In recent years, *model predictive control* (MPC) has been used to design energy management controllers for HEVs and PHEVs. Model predictive control minimises a cost functional over a short future horizon with a terminal cost. For instance, in the doctoral thesis of [12], MPC is used to optimise a parallel HEV using driver-independent speed profiles. In addition, real-time implementation was demonstrated.

In the work of [165], *stochastic model predictive control* (SMPC) is implemented in a series HEV. The driver's future power demand is modelled as a Markov chain, which is trained off-line. In [33], the control algorithm for series HEVs regulates the transition between different operating points by using the battery energy to smooth engine transients in order to improve the powertrain efficiency, rather than the total fuel consumption. An on-line learning SMPC is introduced in [32]. Here again, a Markov process models the future power request, but it is learned in real-time and thus allows adjustments to variations in the driver behaviour. The results show a near-optimum fuel economy in real-world driving cycles. The authors in [27] proposed two different MPC algorithms

(linear, non-linear) for controlling a power-split HEV with a different formulation of the cost functional. The non-linear controller outperformed both the linear MPC and the baseline strategy implemented in the software tool used.

Another research focus is on enhancing the overall fuel efficiency of HEVs by incorporating an advanced learning mechanism and the individual driving style. For example, in [90] *driving pattern recognition* is used to automatically select a control scheme from a database of six representative driving modes using *artificial neural networks* (ANNs). The authors in [211] propose an on-line driving pattern recognition algorithm for a certain route, such as commuter routes. The future driving cycle is predicted by using the previously recorded driving pattern. An on-line, two-step energy management controller for a power-split PHEVs using ANN is proposed in [36]. The ANNs are trained on six driving cycles based on the optimised results obtained by DP. The controller selects the suitable ANN depending on the trip information, such as trip length and duration. The results show improved fuel economy compared to a simple charge depleting/sustaining strategy.

The operation strategy of the 2015 BMW X5 eDrive Plug-In [10] incorporates digital map data with real-time traffic data. An activated route guidance via navigation system enables route-specific optimisation of the SOC level. The future SOC trace is adapted to the upcoming route, for example, to ensure a rather low energy level when driving downhill. In addition, an intelligent function holds back electric energy to guarantee pure electric driving in low-speed areas, such as inner cities. Audi introduced a similar OS in the 2015 Audi Q7 e-tron 3.0 TDI quattro [107]. In [96] and [98], Mercedes launched a route-based operation strategy in their new PHEVs, which ensures pure electric driving in cities over the entire driving route, while concurrently saving fossil fuel and increasing comfort.

2.3. Main Scientific Contributions

State-of-the-art OSs for PHEVs rely on a multi-level energy management controller [91], [122]. Due to the fact that the best fuel economy for plug-in hybrid electric vehicles is achieved when the SOC level drops to its minimum threshold at the end of the trip, the upper-level controller evaluates the optimal SOC trace using several different optimisation algorithms. The low-level controller selects appropriate operation modes with respect to the high-level SOC boundaries. To determine the optimal SOC trajectory, some researchers rely on the advancements of ITS combined with GPS and GIS [91], [122]. Others use trip-modelling based on the upcoming speed limits and predefined constant acceleration/deceleration behaviour [25], [61]. Both energy management schemes result in fuel savings.

There are three main scientific contributions included within the present thesis. First, based on the ideas of [25] and [61], the fixed-trip model is augmented with the driver's individual driving behaviour. Instead of using recorded speed traces from roadside sensors provided by advanced communication technologies such as ITS and GIS, the intelligent energy management controller is based on information about the specific driver's past driving tendencies. The innovative, long-term prediction and adaptation (P&A) algorithm processes fixed-location information, such as speed limits, by using GNSS signals and digital maps. However, the core functions of the P&A are to gather, process and utilise past driving data from the driver's previous trips in order to increase the long-term prediction accuracy without using any other information, such as roadside sensors. Methods for approximating the driver's individual driving style (e.g., the acceleration/deceleration behaviour or the maximum lateral vehicle acceleration) are incorporated with fixed-position information. The advantage of the P&A algorithm is that it is able to achieve outstanding fuel efficiency even in areas where no average speed profile information is available from roadside traffic sensors. Moreover, taking the driver's individual driving style into account over a longer period may increase customer acceptance of HEVs.

Second, a novel holistic energy management controller is proposed here, which is able to account for different trip scenarios, such as trips both within and beyond the AER. Depending on additional available route information, the OS uses a baseline strategy that selects certain operation modes according to predefined rules. If a frequently driven route is recognised and/or input data from the navigation system and GNSS signals are available, this information is used to enhance the overall fuel efficiency of PHEVs. Thus, the controller manages multiple driving routes by selecting an appropriate control path.

Third, all of the effects of the proposed intelligent OS are explicitly presented and discussed in a dynamic vehicle model. This yields more realistic conclusions regarding fuel saving potential and improvements of the longitudinal vehicle dynamics, such as full-load acceleration or vehicle gradeability.

3
Methodology

3.1. Modelling and Simulation Environment

The rapidly growing complexity of vehicles and powertrains requires increased interdisciplinary coordination in vehicle development, a trend which is driving an accompanying shift to a more simulation-centric development process [163]. The need to constantly reduce development time and cost in the highly competitive market of automotive engineering encourages the use of numerical development tools [77].

The development of HEVs, with their growing system complexity [124], wide range of topologies [78] and strong dependency on the power distribution strategy [126], offers more DoF in development and constitutes new challenges. Numerical modelling and simulation approaches are a basic principle to meet these challenges [84]. Furthermore, simulation models lead to a deeper understanding of the system behaviour and efficiently reduce time, cost and effort during the development process [179]. Compared to experiment-based engineering, model-based simulations provide vehicle manufacturers with some competitive advantages, including:

- The initial component design is provided at an early stage of development [124].
- The repeatability of results and technical phenomena is ensured[1] [75], [167].
- Conceptual studies and system optimisation can be carried out in rapid iterations [75], [124].

[1] However, simulation results may vary depending on the software and hardware used, especially when performing parallel computing. Thus, reproducibility is not necessarily ensured.

- Physical limits can be exceeded with no danger [75], [167].
- Disturbances can be controlled [75], [167].
- Difficult measurable values can be derived [75].
- Parameters with low influence can be investigated more easily [75].

The scope of application for numerical models and simulation tools in HEV development is vast. These tools are used to perform conceptual studies on the drivetrain layout [191], to realize fuel saving potential [114] and to achieve optimal component sizing [112], [191]. Moreover, virtual methods are also used to develop and test HEV operation strategies [106], as well as to investigate drivetrain dynamics [204]. Nevertheless, it is important that researchers validate simulation results and the vehicle model behaviour with real-vehicle and component test data frequently.

However, drivetrain modelling should always consider the principle of simplicity: not as accurate as possible, but rather as accurate as necessary [13]. Consequently, the detail of modelling depends on the specific research objective. The subsequent chapters first discuss the two modelling approaches used in the simulation environment and then provide a description of mathematical models of the HEV's drivetrain.

3.1.1. Modelling Approaches

The proposed simulation environment deploys two different drivetrain models, depending on the intended application. The *quasi-static vehicle model* and the *dynamic vehicle model* are described below.

Quasi-static vehicle model

The input variables of the *quasi-static vehicle model*[2], depicted in Figure 3.1, are the vehicle speed v_x, the vehicle acceleration a_x and the inclination β of the road of a predefined driving cycle. The force F_T acting on the wheels to follow the given driving profile is calculated in the vehicle model block by

$$F_T = \underbrace{m_{VEH} \cdot a_x}_{F_A} + F_D + F_R + F_\beta, \tag{3.1}$$

where F_A is the acceleration force, m_{VEH} is the total vehicle mass, F_D is the air drag, F_R is the rolling resistance, and F_β is the resistance due to the road inclination β. Assuming perfect road-tyre contact – thus, no tyre slip is considered – the rotational speed ω_T and the torque T_T at the vehicle tyres can be calculated. These values are constant for each time step Δt_s [69]. Subsequently, the angular speed ω_i and the torque T_i of each powertrain component i are determined backwards to the propulsion units

[2] Also known as backward-facing model [136]

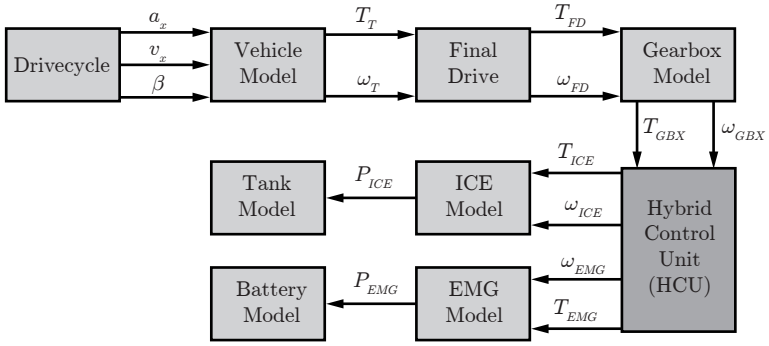

Figure 3.1.: Quasi-static vehicle model

The necessary driving torque T_T and the angular speed ω_T at the tyres are calculated according to the given driving cycle, defined by its speed v_x, acceleration a_x and the road inclination β. The torque and rotational speed of each component are evaluated backward-facing. The hybrid control unit (HCU) with its operation strategy determines the propulsion torque share between the ICE and the EMG. The power demanded at the propulsion units P_{ICE} and P_{EMG} results in a consumption of fossil fuel and electric energy, respectively.

considering component efficiency with the help of multi-dimensional efficiency maps. The energy consumption of the ICE and the EMG is then evaluated with fossil fuel consumption maps and electric energy consumption maps, respectively. Since *backward-facing vehicle models* run with relatively large time steps, this method operates quickly and is therefore convenient for optimisation purposes [69], [136]. The main drawback of the quasi-static method is its "backward" formulation, resulting in a loss of physical causality and the need to know a driving cycle a-priori [69]. Moreover, this modelling approach is not capable of considering drivetrain dynamics [136], since only algebraic equations are calculated. Nevertheless, as long as no drivetrain dynamics have to be considered, the backward modelling approach is sufficiently accurate [115].

Dynamic vehicle model

In contrast, *dynamic vehicle models*[3] (see Figure 3.2) contain ordinary differential equations (ODEs) in state-space form:

$$\frac{\mathrm{d}}{\mathrm{d}t}x(t) = f\Big(x(t), u(t)\Big), \qquad x(t) \in \mathbb{R}^n, u \in \mathbb{R}^m. \tag{3.2}$$

The state variable is denoted by $x(t)$ (e.g., position, velocity, brake pressure), and the control variable is $u(t)$ (e.g., steering-wheel angle, accelerator pedal position, gear lever position). Forward-facing models deal with quantities that are measurable in real drivetrains and have the correct causality [69], [136]. Moreover, a driver model has to be

[3] Also called forward-facing models [136]

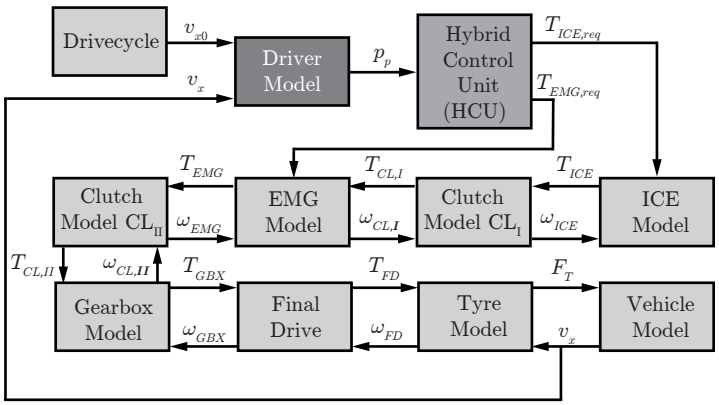

Figure 3.2.: Dynamic vehicle model using the example of a parallel HEV drivetrain

A driver model defines the torque demand of the ICE $T_{ICE,req}$ and/or the EMG $T_{EMG,req}$ by comparing the actual vehicle speed v_x with the driver's intended speed v_{x0} in the form of a pedal position input p_p. The HCU determines a fuel-efficient power distribution between the two propulsion units. The torque produced by the ICE and EM is transmitted through the gearbox and final drive. At the wheels, the torque results in a longitudinal tyre force F_T, which causes a vehicle speed v_x, which is then propagated back to the propulsion units as angular speed ω_i.

included that provides the control variables $u(t)$ in the form of the desired propulsion torque of the ICE $T_{ICE,req}$ and/or EMG $T_{EMG,req}$ and brake torque, to meet the driver's intended speed profile. Consequently, the torque flow starts from the driver input – a pedal position input p_p – and propagates through the different drivetrain components to the wheels. The resulting traction force F_T at the tyres causes a certain vehicle speed v_x and an angular speed ω_i at each powertrain component. There will be a small margin of error between the actual vehicle speed v_x and the intended speed v_{x0} of the driver, due to the controller characteristics of the driver model. Figure 3.2 shows a schematic representation of a dynamic vehicle model for a P2-HEV drivetrain. Based on the pedal position input p_p (evaluated by comparing the actual v_x with the desired vehicle speed v_{x0}), the hybrid control unit (HCU) determines a fuel-efficient power distribution of both propulsion units – the ICE and EMG. The dynamic vehicle model can theoretically cover all dynamic effects in the drivetrain and capture limits of the physical system. Consequently, the description of the driver-vehicle system is more realistic. However, the simulation has to run in smaller time steps [136] because of the numeric time-integration of the ODEs providing different dynamics for each simulated component. Moreover, higher system complexity and high modelling effort for the control algorithm are disadvantageous [115]. Unlike the quasi-static vehicle model, in the dynamic vehicle model the power transfer is bi-directional, which means the direction of the effort (torque) is opposite to the direction of the flow (speed) [136], as in real physical systems (cf. Figures 3.1 and 3.2).

3.1.2. Modelling of Drivetrain Components and Vehicle Model

3.1.2.1. Internal Combustion Engine (ICE)

The ICE converts the chemical energy of fuels via combustion into kinetic energy, which is used to propel vehicles. Although there are different types of combustion engines, the most common ones are piston engines. In the automotive area, these engines work according to the four-stroke principle[4]: *intake*, *compression* and *ignition*, *expansion*, and *exhaust*. The most frequent powertrain units for passenger vehicles are gasoline and diesel engines [43], as shown in Figure 1.1. In both working principles, a fuel-air mixture is ignited either by a spark plug in gasoline engines or by self-ignition at the end of the compression stroke in diesel engines. The released heat increases the pressure of the pre-compressed gases, which is rendered into mechanical work at the crankshaft during the subsequent expansion. According to [131], the reaction equation for *complete combustion* of fossil fuels reads

$$\mathrm{C}_{\tilde{m}}\mathrm{H}_{\tilde{n}}\mathrm{O}_{\tilde{p}} + \left(\tilde{m} + \frac{\tilde{n}}{4} - \frac{\tilde{p}}{2}\right)\mathrm{O}_2 \longrightarrow \tilde{m}\mathrm{CO}_2 + \frac{\tilde{n}}{2}\mathrm{H}_2\mathrm{O} \tag{3.3}$$

where $\mathrm{C}_{\tilde{m}}\mathrm{H}_{\tilde{n}}\mathrm{O}_{\tilde{p}}$ is the general expression for fossil fuels. The number of moles of carbon (C), hydrogen (H) and oxygen (O) are denoted by $\tilde{m}$, $\tilde{n}$ and $\tilde{p}$, respectively. This means that during a complete combustion, the fossil fuel is oxidised, and only CO_2 and H_2O are produced.

However, real combustion processes are characterised by oxidation with ambient air (air composition: 21 vol.-% O_2, $<$ 1 vol.-% inert gas and $\approx$ 78 vol.-% N_2 [131]) and incomplete chemical reactions. Consequently, due to *incomplete combustion*, additional emissions are produced, such as CO, HC, NOx and PM [20], [44].

The working process of modern ICEs is controlled by numerous electronic control units, such as mixture and idle speed control [44]. These control algorithms significantly influence the characteristics of an ICE. Consequently, modelling the behaviour of internal combustion engines always includes these control algorithms [130].

Mean value model

In combustion engines, the requested torque T_{ICE} depends on the current *operation point*, which is characterised by the current ICE rotational speed ω_{ICE} and the accelerator pedal position p_p.

$$T_{ICE} = f(\omega_{ICE}, p_p). \tag{3.4}$$

Equation (3.4) can be characterised as a map that is measured on an engine dynamometer for a given accelerator pedal position p_p and engine speed ω_{ICE}, as shown in Figure 3.5(a). However, the present research uses a generic relation between engine torque T_{ICE} and

[4] Two-stroke methods also exist, but they are not popular in automotive engineering.

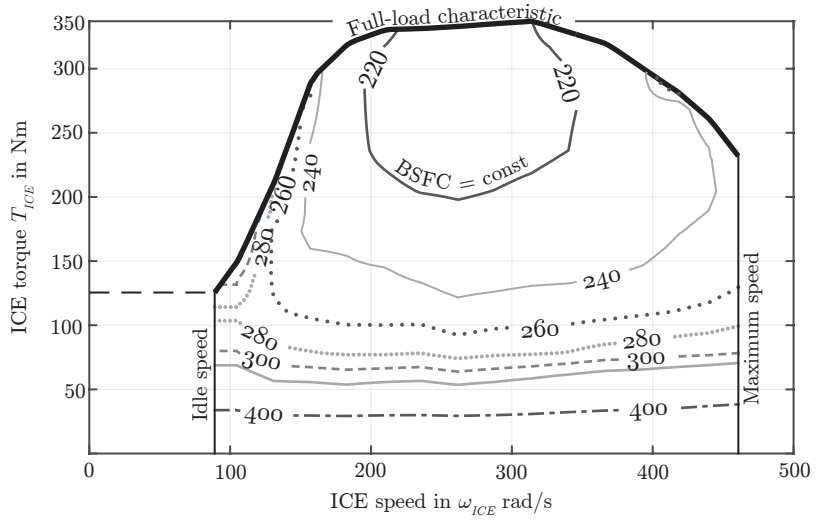

Figure 3.3.: Implemented ICE map with its characteristic parameters

The different lines in the map are the areas with a constant brake-specific fuel consumption (BSFC). The lower the BSFC, the higher the ICE efficiency. Moreover, the idle speed and the maximum speed of the ICE are highlighted.

the pedal position p_p, which assumes that zero pedal position $p_p = 0$ is similar to the engine's drag torque $T_{ICE,d}$, and $p_p = 1$ equals the *full-load characteristic* $T_{ICE,max}$. Intermediate values are interpolated linearly, as shown in Eq. (3.5) and Figure 3.5(b).

$$T_{ICE}(\omega_{ICE}, p_p) = T_{ICE,d}(\omega_{ICE}) + p_p \cdot \Big(- T_{ICE,d}(\omega_{ICE}) + T_{ICE,max}(\omega_{ICE}) \Big). \quad (3.5)$$

In real ICE maps the accelerator pedal position characteristics are often non-linear [53], as shown in Figure 3.5(a). The drag torque $T_{ICE,d}$, as seen in Figure 3.5(b), at $p_p = 0\,\%$, is defined as negative torque $T_{ICE,d} < 0$, and it increases almost linearly with the engine speed ω_{ICE} [130], [134]. The implemented engine map is shown in Figures 3.3 and 3.5(b).

Using Eq. (3.5), the characteristics of the ICE can be described following the *principle of angular momentum*

$$\Theta_{ICE} \cdot \dot{\omega}_{ICE} = T_{ICE} - \bar{T}_{ICE,out}, \quad (3.6)$$

where Θ_{ICE} is the moment of inertia of the ICE, and $\bar{T}_{ICE,out}$ is the actual torque at the crankshaft, without considering the system response time. The ICE response is modelled in Eq. (3.7) as first-order lag element $G_2(s)$ in combination with a dead-time element $G_1(s)$. These transfer functions account for the combustion delay and the intake process [103]. Therefore, the engine torque at the crankshaft $T_{ICE,out}$ considering the engine response reads

$$T_{ICE,out}(s) = \bar{T}_{ICE,out}(s) \cdot \underbrace{\frac{K_{p,ICE}}{1 + T_{l,ICE} \cdot s}}_{G_2(s)} \cdot \underbrace{e^{-sT_{t,ICE}}}_{G_1(s)}, \quad (3.7)$$

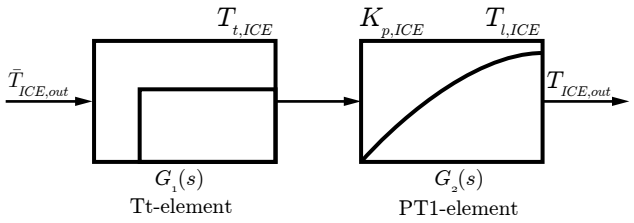

Figure 3.4.: Internal combustion engine response characteristics

The ICE dynamic response characteristics are described by a dead-time element $G_1(s)$ and a first-order lag element $G_2(s)$. The dead-time element represents the combustion delay, and the first-order lag element accounts for the intake process. Both time variables $T_{t,ICE}$ and $T_{l,ICE}$ are inversely proportional to the rotational engine speed ω_{ICE} [103]. The amplification factor of the PT1-element is described by $K_{p,ICE}$. The engine torque at the crankshaft considering the ICE dynamics is represented by $T_{ICE,out}$.

where $K_{p,ICE}$ is the amplification factor, $T_{l,ICE}$ is the first-order lag time of the PT1 element, and $T_{t,ICE}$ is the delay time. In [85], a second-order lag element (PT2) is proposed to consider the dynamic characteristics of the ICE. According to [130], such a modelling approach is sufficiently accurate. Nevertheless, this thesis uses a PT1 characteristics with a dead-time element, as shown in Figure 3.4. Figure 3.3 shows the brake-specific fuel consumption (BSFC) [44]. The lower the BSFC value, the higher the engine efficiency η_{ICE}. It reads

$$\text{BSFC} = \frac{\dot{m}_f}{P_{ICE}} = \frac{1}{\eta_{ICE} \cdot H_u}, \tag{3.8}$$

where $\dot{m}_f$ is the fuel mass flow, P_{ICE} is the effective ICE power, H_u is the lower heating value of the fuel, and η_{ICE} is the efficiency of the ICE defined as

$$\eta_{ICE} = f(T_{ICE}, \omega_{ICE}). \tag{3.9}$$

Emissions which occur during engine operation are not considered in this work, since the focus of the present work is on fuel efficiency rather than clean combustion. Therefore, an ideal exhaust gas treatment is assumed. Nevertheless, in practice duty-cycles (permanent transitions between different operation modes) or engine shut-off at idle causes engine or catalyst cooling, which increases emissions.

Engine Control Unit (ECU)

The objective of the engine control unit (ECU) is to positively influence drivability[5], fuel consumption and exhaust emissions. To this end, multiple complex control systems [44] are implemented in modern ICEs. In this thesis, the amount of controllers is reduced to the idle speed controller, the engine speed limiter, the deceleration fuel

[5]Drivability describes the objective assessment of driving comfort based on physically measurable criteria [130].

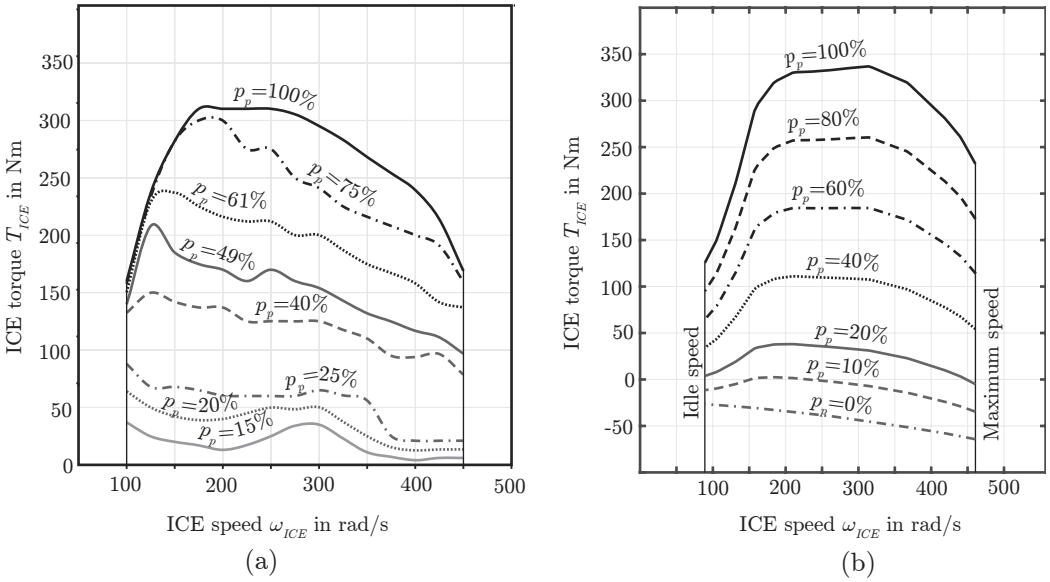

Figure 3.5.: Schematic representation of an engine map

Figure (a) depicts an engine map with non-linear pedal position p_p characteristics based on [53]. However, the engine map implemented in Figure (b) linearly interpolates between the drag torque characteristics ($p_p = 0\,\%$) and the full-load characteristics ($p_p = 100\,\%$) of the ICE.

cut-off (DFCO) and an automatic start/stop function. The idle speed is controlled with a proportional-integral-differential (PID) controller, see also [103]. Its parameters are empirically evaluated with the help of the *open loop method* of *Ziegler* and *Nichols* [83]. The engine speed limiter is modelled with the help of the engine characteristic map, which provides zero torque at maximum engine speed, as shown in Figure 3.3. During engine towing, fuel injection is (partially[6]) stopped, which results in a lower total fuel consumption. Modern passenger vehicles are often equipped with a start/stop function, which switches off the engine during standstill. In the implemented HEV, this function is extended so that the HEV can operate in pure electric mode, which will further increase fuel efficiency. The fossil fuel consumed during ICE operation $\dot{m}_f(t)$ for each time step is modelled as a function of the ICE speed ω_{ICE} and its load T_{ICE} and reads

$$\dot{m}_f(t) = f\Big(\omega_{ICE}(t), T_{ICE}(t)\Big). \tag{3.10}$$

The average fuel consumption over a distance of 100 km $\bar{C}$ can be written

$$\bar{C} = \frac{\int \dot{m}_f(t)\,\mathrm{d}t}{\rho_f \cdot d} \cdot 10^5 \tag{3.11}$$

[6]While towing (e.g., driving downhill) it may occur that the entire drag torque of the ICE is too high to maintain the desired speed. In this case, the driver has to push the accelerator pedal $p_p > 0$ slightly to reduce the drag torque. This again results in a fossil fuel injection.

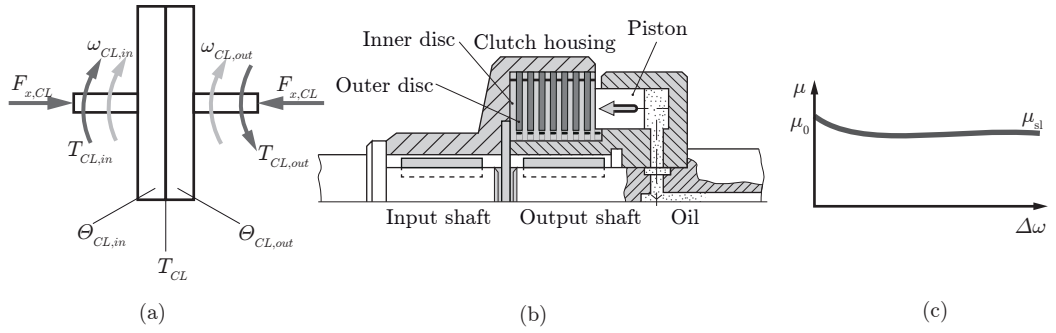

Figure 3.6.: Implemented clutch model

Figure (a) depicts the simplified clutch model used here, which consists of two inertias; Figure (b) shows a schematic representation of a multi-disc wet clutch with its main components; and Figure (c) highlights a representative μ-characteristics based on [206]. The μ-characteristic depends on multiple factors, such as the friction pairing or the rotational speed difference $\Delta\omega$.

where ρ_f is the fuel density in kg/l, and d is the currently driven distance in m.

3.1.2.2. Clutch (CL)

A clutch ensures a comfortable start-up process and enables the propulsion unit to be disengaged from the remainder drivetrain [110]. Moreover, it allows rotational speed adaptation between the input and output shafts. While manual transmissions mainly feature dry clutches, conventional automatic transmissions use wet clutches, see Figure 3.6(b). The *transferable clutch torque* T_{CL} (cf. Figure C.1) reads [125], [206]

$$T_{CL} = N_{pl} \cdot r_m \cdot \mu \cdot F_{x,CL}, \tag{3.12}$$

where $F_{x,CL}$ is the axial contact force, r_m is the average friction radius, μ is the friction coefficient and N_{pl} is the number of clutch plates. The friction coefficient μ depends on the clutch slip $\Delta\omega_{CL} = \omega_{CL,in} - \omega_{CL,out}$. Moreover, the sliding friction coefficient μ_{sl} is smaller than the static friction coefficient μ_0, as shown in Figure 3.6(c).

Modelling a slipping clutch and a locked clutch is numerically complex [130], [212]. The approach of [212] was chosen, since it performs with high numerical stability. The fundamental problem of clutch models is that during slipping the two inertias move independently, and the model therefore behaves as a second-order model, cf. Eq. (3.14). Nevertheless, if the clutch is fully engaged, the system order is reduced [212], as in Eq. (3.13).

$$(\Theta_{CL,in} + \Theta_{CL,out}) \cdot \dot{\omega}_{CL} = T_{CL,in} - T_{CL,out}, \qquad \omega_{CL,in} = \omega_{CL,out} = \omega_{CL}, \tag{3.13}$$

where $\Theta_{CL,in/out}$ are the moments of inertia at the input/output shafts, $\dot{\omega}_{CL}$ is the rotational acceleration while the clutch is engaged, and $T_{CL,in/out}$ and $\omega_{CL,in/out}$ are

the torques and rotational speeds at the input/output shafts, respectively. If clutch slip occurs, i.e., $\omega_{CL,in} \neq \omega_{CL,out}$, the system equations shown in Figure 3.6(a) read in matrix form

$$\underbrace{\begin{bmatrix}\Theta_{CL,in} & 0\\ 0 & \Theta_{CL,out}\end{bmatrix}}_{\mathbf{M}}\underbrace{\begin{bmatrix}\dot{\omega}_{CL,in}\\ \dot{\omega}_{CL,out}\end{bmatrix}}_{\dot{\boldsymbol{\omega}}} = \underbrace{\begin{bmatrix}T_{CL,in}\\ -T_{CL,out}\end{bmatrix}}_{\mathbf{T}} - \underbrace{\begin{bmatrix}1\\ -1\end{bmatrix}}_{\mathbf{d}^T} T_{CL}\,\mathrm{sgn}\left(\underbrace{\begin{bmatrix}1 & -1\end{bmatrix}}_{\mathbf{d}}\underbrace{\begin{bmatrix}\omega_{CL,in}\\ \omega_{CL,out}\end{bmatrix}}_{\boldsymbol{\omega}}\right), \tag{3.14}$$

where $\mathbf{M}$ is the rotational mass matrix, $\dot{\boldsymbol{\omega}}$ is the rotational acceleration vector, $\mathbf{d}$ is a coefficient vector, $\mathbf{T}$ is the torque vector, and $\boldsymbol{\omega}$ is the rotational speed vector. Introducing a proper congruent state space transformation decouples the original system into two independent parallel systems, namely the *main dynamics* and *relative dynamics* [212]. The state space congruent transformation matrix $\mathbf{K}$ reads

$$\mathbf{K} = \begin{bmatrix}1 & \frac{\Theta_{CL,out}}{\Theta_{CL,\Sigma}}\\ 1 & -\frac{\Theta_{CL,in}}{\Theta_{CL,\Sigma}}\end{bmatrix}, \tag{3.15}$$

with $\Theta_{CL,\Sigma} = \Theta_{CL,in} + \Theta_{CL,out}$. The generalised speed vector $\mathbf{z}$ and the rotational speed vector $\boldsymbol{\omega}$ hold the following relation

$$\boldsymbol{\omega} = \mathbf{K}\mathbf{z}. \tag{3.16}$$

Finally, the system dynamics with generalised speeds can be determined by

$$\begin{bmatrix}\dot{z}_1\\ \dot{z}_2\end{bmatrix} = \begin{bmatrix}\frac{1}{\Theta_{CL,\Sigma}} & \frac{1}{\Theta_{CL,\Sigma}}\\ \frac{\Theta_{CL,out}}{\Theta_{CL,\Pi}} & -\frac{\Theta_{CL,in}}{\Theta_{CL,\Pi}}\end{bmatrix}\begin{bmatrix}T_{CL,in}\\ -T_{CL,out}\end{bmatrix} - T_{CL}\begin{bmatrix}0\\ \frac{\Theta_{CL,\Sigma}}{\Theta_{CL,\Pi}}\end{bmatrix}\mathrm{sgn}\left(\begin{bmatrix}0\\ 1\end{bmatrix}^T\begin{bmatrix}z_1\\ z_2\end{bmatrix}\right), \tag{3.17}$$

with $\Theta_{CL,\Pi} = \Theta_{CL,in} \cdot \Theta_{CL,out}$ and the generalised acceleration vector $\dot{\mathbf{z}} = [\dot{z}_1 \quad \dot{z}_2]^T$. The main dynamics are described with $\dot{z}_1$, while the relative dynamics are stated in $\dot{z}_2$. Using the inverse transformation of Eq. (3.15) results in the rotational accelerations of the input and output shafts. Sliding mode theory[7] [7] is applied, in which the coulomb friction torque T_{CL} is the sliding input variable for the system. If the generalised relative velocity $z_2 = 0$, the transferable clutch torque starts switching at a finite frequency between $\pm T_{CL}$. Therefore, the system in Eq. (3.17) converges towards the sliding surface $s_{sl} = 0$. The required high switching frequency results in a small simulation time step Δt_s, which concurrently increases the simulation time [212].

A more straightforward approach which neglects detailed processes during clutch actuation is also introduced within this thesis. This model limits the rotational speed change $\dot{\omega}_{CL,sft}$ while shifting. Assuming an average shifting time t_{sft} between 0.7 s to 1.2 s [133] results in

$$\dot{\omega}_{CL,sft} = \frac{|i_{\gamma,hi} - i_{\gamma,lo}|\omega_{CL,in}}{t_{sft}}, \tag{3.18}$$

[7] Sliding mode theory is applied in linear and non-linear control. It toggles between two control rules depending on its state vector, whereby sliding modes occur [7].

where $i_{\gamma,hi}$ and $i_{\gamma,lo}$ are the gear ratios of the two gears involved. For upshifting, $\dot{\omega}_{CL,sft}$ is negative, while it is positive for downshifting manoeuvres. The immediate torque change is limited in a similar way.

3.1.2.3. Electric Motor/Generator (EMG)

In conventional pure ICE-driven vehicles, an EMG is used as starter or as an alternator. In HEVs the electric traction motors are used in order to provide additional propulsion power. Besides the battery, the EMG is a key component [66]. Depending on the HEV's drivetrain layout, the dimensioning and the number of EMGs vary [78], [169]. In a P2-HEV drivetrain layout (cf. Chapter 2.1), the EMG can operate in different ways.

1. The EMG can convert the electric power of the battery to mechanical power to support the ICE or drive the vehicle purely electrically.
2. In addition, the electric motor/generator is able to convert the excess mechanical power of the ICE into electrical power to charge the battery, also known as load point shifting [169].
3. Transforming the kinetic energy during braking into electrical energy of the battery, also known as recuperation, is a third typical operation mode of the EMG.

In general, there are two different types of machines: direct current (DC) and alternating current (AC) motors. Although there are different types available, an EMG always consists of a stator and a rotor, which is directly connected to the output shaft. In this thesis, an AC permanent-magnet synchronous motor (PMSM) is used as an additional traction motor.

Phenomenological EMG model

This model describes the motor characteristics with the help of multi-dimensional maps. The differential equation of the mechanical part of the EMG reads

$$\Theta_{EMG} \cdot \dot{\omega}_{EMG} = T_{EMG} - \bar{T}_{EMG,out}, \tag{3.19}$$

where Θ_{EMG} is the inertia of the rotor of the EMG, T_{EMG} is the motor torque requested due to driver or operation strategy input, and $\bar{T}_{EMG,out}$ is the torque at the output shaft of the EMG without considering the system response. The response time of the EMG follows a first-order lag element [128]. Consequently, the torque at the output shaft reads in frequency domain

$$T_{EMG,out}(s) = \frac{K_{p,EMG}}{1 + T_{l,EMG} \cdot s} \cdot (T_{EMG}(s) - \Theta_{EMG}(s) \cdot s \cdot \omega_{EMG}(s)). \tag{3.20}$$

The parameter $T_{l,EMG}$ is the time constant, and $K_{p,EMG}$ is the proportional factor of the PT1-element. The current required to deliver the output torque $T_{EMG,out}$ is determined

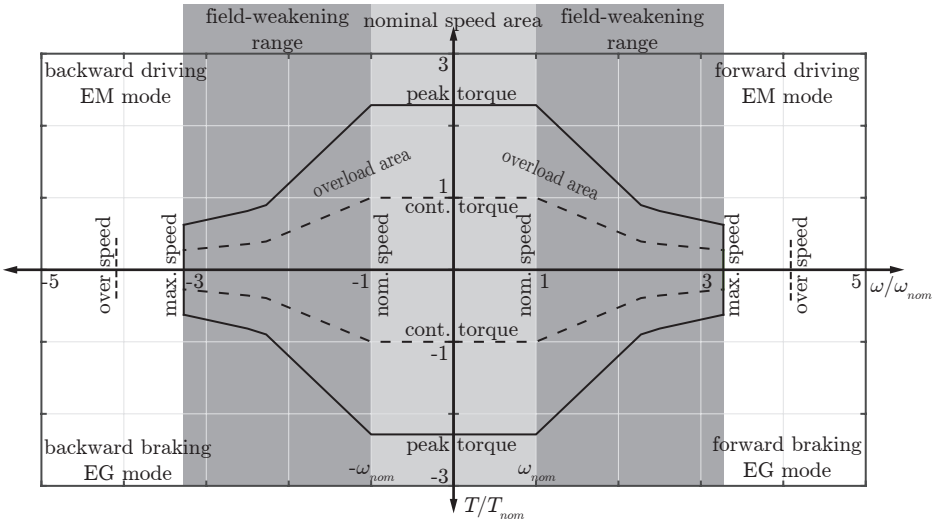

Figure 3.7.: Schematic representation of a four-quadrant EMG characteristics

The implemented EMG characteristics are assumed to be symmetrical in relation to the electric motor (EM) and generator (EG) mode. Within the nominal speed area $\pm\omega_{nom}$, there is a constantly high continuous EMG torque T_{nom}. This area is followed by the field-weakening range. The EMG can operate in its overload mode for a short time.

using a multi-dimensional efficiency map η_{EMG} (see Figure 3.8), and the conservation-of-energy principle, using Eq. (3.21) and Eq. (3.22).

$$\eta_{EMG} = f(\omega_{EMG}, T_{EMG}), \tag{3.21}$$

$$I_{EMG} = \frac{T_{EMG} \cdot \omega_{EMG}}{U_{BAT}} \cdot \eta_{EMG}^{-\mathrm{sgn}(T_{EMG})} \tag{3.22}$$

The signum function considers the losses in both EM ($T_{EMG} \geq 0$) and EG ($T_{EMG} < 0$) mode. The instantaneous battery voltage is given by U_{BAT}. The efficiency η_{EMG} is assumed to be symmetric in the first and fourth operation quadrant. Consequently, it holds that

$$\eta_{EMG}(\omega_{EMG}, |T_{EMG}|) = \eta_{EMG}(\omega_{EMG}, -|T_{EMG}|). \tag{3.23}$$

Figure 3.7 depicts the motor speed-torque characteristics. The EMG has two different operation modes. First, in the continuous operation mode, the motor provides its continuous torque T_{cont} and its continuous power P_{cont}. This torque is permanently available, without violating any thermal or mechanical constraints. In contrast, the overload operation mode allows higher torque T_{max} and power P_{max} over a limited short-term. The duration mainly depends on the windings temperature and the mechanical strength [79]. Temperature sensors in the end windings help to control the different operation modes. Typical overload factors are between 1 to 2.5 [79]. The continuously high torque level

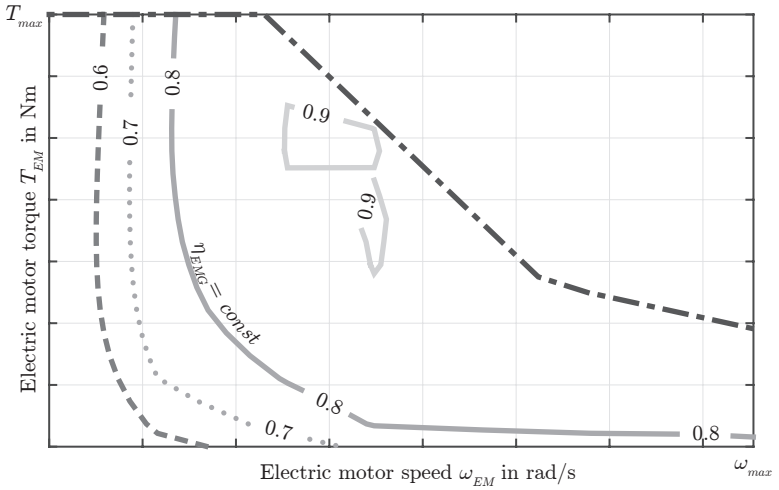

Figure 3.8.: Schematic representation of an electric motor efficiency

Only the first operation quadrant of the implemented EMG efficiency map is shown, since a symmetric characteristic is assumed. The EMG is characterised by high operation efficiencies, depicted by the different lines with constant EMG efficiency η_{EMG}. Operating efficiencies above 90 % are possible.

from zero speed to nominal speed ω_{nom} is another advantage of an EMG (cf. Figure 3.7). In this area, the power increases linearly with the motor speed, the current is proportional to the motor torque, and the motor speed is proportional to the voltage. At rotational speeds higher than ω_{nom}, the power remains at nearly constant high power, while the motor torque decreases in indirect proportion to the motor speed. This area is also known as field-weakening range. In this area, the maximum allowable voltage is reached, and consequently the magnetic flux has to be reduced in order to keep the voltage at a high constant level [79]. The shape of the field-weakening range depends on the type of EMG – synchronous or asynchronous machines.

For the present thesis, this modelling approach is sufficiently accurate and requires no advanced control algorithm. Nevertheless, electrical parameters are not used. The inverter model is assumed to be ideal, which means that no additional losses and time delays occur. Since the efficiency of the power electronics varies between 0.93 to 0.99 [79], this assumption does not strongly affect the model accuracy.

3.1.2.4. Battery (BAT)

The additional ESS has a major importance in HEVs. There are different types of ESS (e.g., mechanical, chemical, electrical). Nevertheless, this chapter only discusses battery HEVs. The fundamental system of a battery is the galvanic cell. This cell enables the energy conversion from chemically-bounded to electrical energy and vice versa. Figure 3.9 shows the main components of a lithium-ion (Li-ion) battery. The battery consists

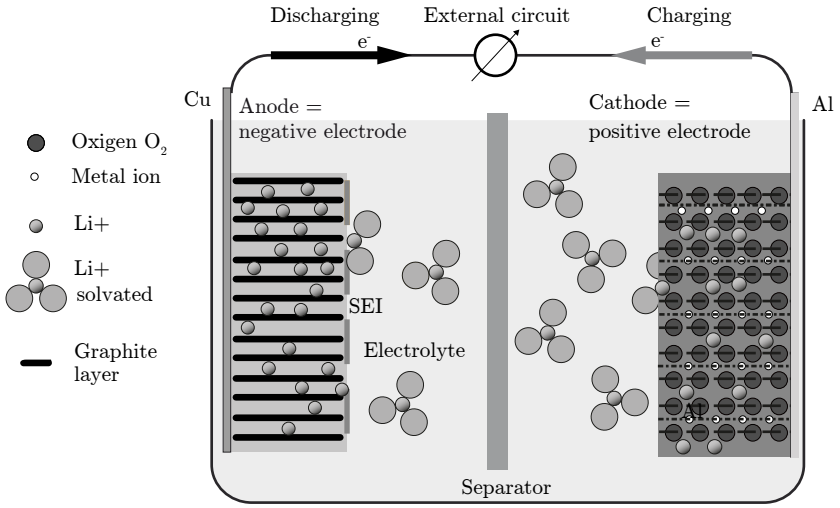

Figure 3.9.: Components of a Li-ion battery [8]

The basic components of a galvanic cell are two electrodes (anode, cathode), a separator, an electrolyte and an external circuit to power a device. The anode consists of thin hard carbon layers with Li^+-ions in between. Since the separator is commonly designed as a shut-down-separator, it melts above temperatures of 135 °C. The electrolyte is a solvent mixture with dissolved conducting salt. Solvated Li^+-ions develop due to the reaction of Li^+ with the electrolyte. The solid-electrolyte interface (SEI) is formed during the initial charging and increases the battery's internal resistance.

of two different electrodes. The anode is a reductant, and the cathode is an oxidant. A separator prevents any electron transfer between the two electrodes inside the cell. Moreover, there is an electrolyte that conducts the working ions [62].

During a discharging process, Li^+-ions move from the anode, through the electrolyte and separator to the cathode. Thereby, the electrolyte and the Li^+-ions form solvated Li^+. Concurrently, electrons e^- flow from the anodes via external circuits to the cathodes, thereby reducing the anodes. This electron flow enables a current, which can be used by a power device connected to the external circuit. Thus, during discharge the battery transforms the stored chemical energy into electrical energy at the load device [62]. The anode consists of thin hard carbon layers with Li^+-ions in between. Since the separator is commonly designed as shut-down-separator, it melts above temperatures of 135 °C. The electrolyte is a solvent mixture with dissolved conducting salt. Solvated Li^+-ions are developed due to the reaction of Li^+ with the electrolyte. The solid-electrolyte interface (SEI) is formed during the initial charging and increases the battery's internal resistance.

A battery pack for automotive application consists of several electrochemical cells in series and/or parallel arrangement. Different types of Li-ion batteries are commonly used in vehicles [30], [120]. According to [8], the reaction equation of Li-ion batteries

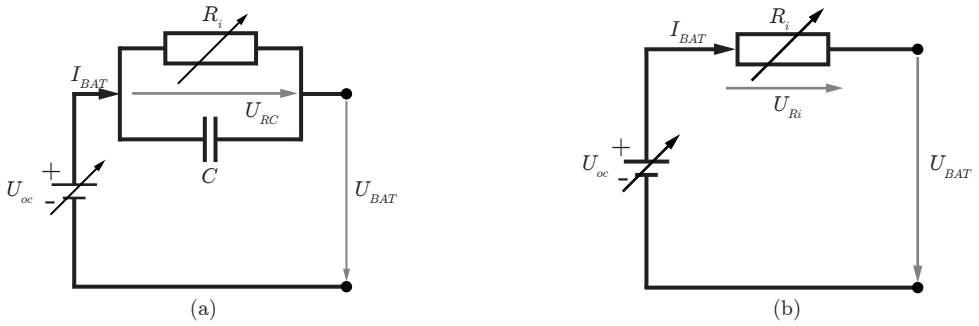

Figure 3.10.: Different battery models

Figure (a) shows the implemented dynamic model. It is a simplification of the well-known Randles battery model, the parameters of which are hard to identify exactly [210]. The simplification arises from ease of parametrisation. It consists of an open-circuit voltage U_{oc} and a parallel RC-element. Figure (b) depicts the implemented quasi-static battery model, which consists of only one internal resistance R_i.

generally reads

$$\mathrm{LiMO_2} \underset{\text{discharging}}{\overset{\text{charging}}{\rightleftharpoons}} \mathrm{Li_{1-x}MO_2} + x\mathrm{Li^+} + x\mathrm{e^-}, \tag{3.24}$$

$$x\mathrm{Li^+} + 6\mathrm{C} + xe^- \underset{\text{discharging}}{\overset{\text{charging}}{\rightleftharpoons}} \mathrm{Li}x\mathrm{C_6}, \tag{3.25}$$

$$\mathrm{LiMO_2} + 6\mathrm{C} \underset{\text{discharging}}{\overset{\text{charging}}{\rightleftharpoons}} \mathrm{Li_{1-x}MO_2} + \mathrm{LiC_6}, \tag{3.26}$$

where $\mathrm{LiMO_2}$ are lithium metal oxides, M is a transition metal, often consisting of Cobalt (Co) and/or Nickel (Ni) and/or Manganese (Mn)[8], the anode material is graphite C, and $\mathrm{LiC_6}$ is lithiated graphite. Since the Li-ion battery technology offers high specific energy, high specific power, high efficiency and little self-discharging effect [120], it is suitable for application in HEVs. In the literature, different types of battery models are discussed. Depending on the model requirements, three main groups are distinguished [95], [210]:

- Physical-chemical models
- Equivalent-circuit models
- Mathematical black-box models

An equivalent-circuit model approach enables fast calculation and sufficient accuracy of the basic dynamic effects. The characteristics of the battery are reproduced by resistances, inductances, and capacitances. The implemented dynamic battery model (see Figure 3.10) accounts for self-discharging effects, as well as for the dependency of the open-circuit voltage U_{oc} on the SOC and temperature effects. The battery model used

[8]Such a cathode combination is referred to nickel-manganese-cobalt, or NMC.

represents a simplification of the well-known *Randles model* [161]. However, the simplification guarantees an easy parametrisation of the battery with an adequate accuracy, which is not the case with the Randles model [210], because a clear allocation of the internal resistances is prohibitively difficult. The open-circuit voltage U_{oc} is assumed to be an ideal voltage source, which depends on the current SOC and the current temperature ϑ. The RC-element models battery dynamic behaviour. The internal resistance $R_i(SOC, \vartheta)$ accounts for several different phenomena, as shown in Eq. (3.27),

$$R_i = R_d + R_{ct} + R_o. \tag{3.27}$$

The variable R_o is the ohmic resistance, which occurs in the electrolyte, the electrodes and the current collector. It causes the instantaneous voltage drop at the beginning of the battery discharge, as shown in Figure 3.11(a). The reaction kinetics occurring at the electrodes result in the charge-transfer resistance R_{ct}. The diffusion of ions in the electrolyte is accounted for with the diffusion resistance R_d [66]. The internal resistance R_i is different for charging and discharging sequences. The capacitance C describes the capacitive effects of the charge accumulation/separation occurring at the interface between the electrodes and electrolyte [66]. Using Kirchhoff's laws, the dynamic behaviour of the battery model in Figure 3.10(a) reads:

$$C\frac{\mathrm{d}}{\mathrm{d}t}U_{RC} = I_{BAT} - \frac{U_{RC}}{R_i}, \tag{3.28}$$

$$U_{BAT} = U_{oc} - U_{RC}, \tag{3.29}$$

where I_{BAT} is the battery current, U_{RC} is the voltage drop in the parallel RC-branch, and the parameter C is the capacitance. The current battery's state of charge $SOC(t)$ is

$$SOC(t) = SOC_0 - \int_0^t \frac{I_{BAT}}{Q_{nom}}\mathrm{d}\tau. \tag{3.30}$$

The initial battery's SOC is described by SOC_0, and Q_{nom} is the nominal battery capacity.

Battery Monitoring Unit (BMU)

The main task of the battery management system is to ensure the battery's health throughout the entire battery life-cycle [41]. The implemented BMU continuously monitors the battery current I_{BAT}, the battery voltage U_{BAT} and the SOC. To guarantee a high SOH, the battery temperature ϑ has to be monitored as well (cf. Figure 3.12). The SOH of a battery describes battery ageing effects: at high SOC, electrolyte decomposition occurs, and at low voltage, arrester corrosion occurs. The BMU limits the maximum current in order to avoid lithium plating. This phenomenon occurs when metallic lithium precipitates at the anodes during charging phases and significantly reduces the battery pack's capacity and battery performance [109] and may result in short-circuits [213].

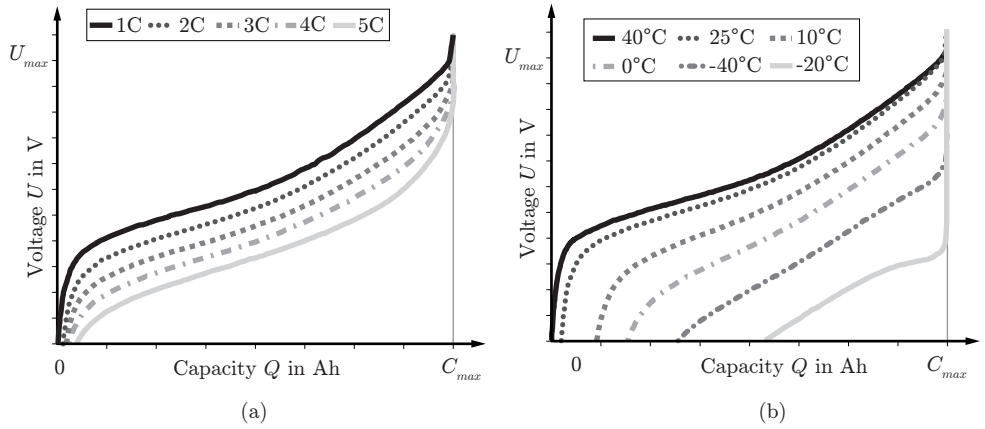

Figure 3.11.: Characteristics of the implemented battery model

Figure (a) shows the decreasing influence of the battery current, expressed by the C-rate[9], on the battery voltage. The C-rate describes the ratio of the maximum battery current and its capacity. Figure (b) shows the battery's performance with varying temperature. It decreases as the temperature decreases.

Since the battery's performance strongly depends on the cell temperature ϑ, see also Figure 3.11(b), the battery heating is also included in the model. The amount of heat to be dissipated E_Q [57] is determined by

$$E_Q = \int_0^t P_Q \, \mathrm{d}\tau = \int_0^t \frac{1}{R_i} U_{RC}^2 \, \mathrm{d}\tau, \tag{3.31}$$

where R_i is the internal resistance of the battery, and P_Q is the heat power. Due to the assumption of ideal cooling, the entire amount of heat dissipates. Consequently, the battery model always performs in its optimal temperature range between 20 °C to 40 °C [213]. If the temperature is too low, the internal resistances rise significantly, and if the temperature is too high, thermal decomposition of the electrolytes is followed by cell inflammation [213]. The monitoring of the cell voltage is also a crucial part of the BMU. Severe discharging ($< 2.5\,\mathrm{V}$) leads to battery capacity loss and higher self-discharging effects. However, over-voltage ($> 4.2\,\mathrm{V}$) results in spontaneous ignition [213]. In addition to the voltage control, the battery's SOC is also evaluated. The usable SOC is set to the almost linear voltage area, see Figure 3.11. The SOH is approximated with the help of the battery states voltage U, current I and temperature ϑ.

[9]The C-rate is defined as the ratio of maximum charging/discharging current and the capacity, thus C-rate $= \frac{I_{max}}{C}$.

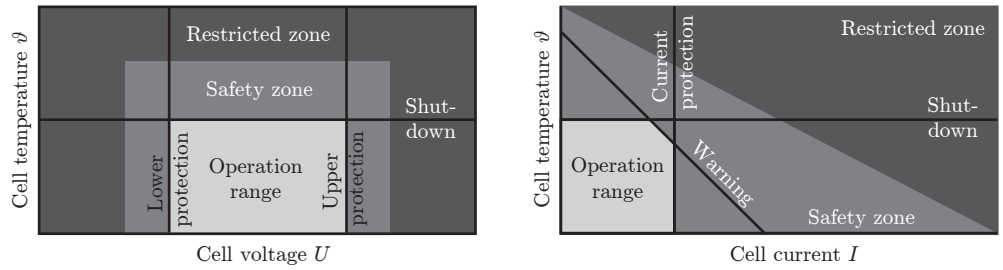

Figure 3.12.: Limited operation area of a Li-ion battery [41]

The operation range is limited by the cell temperature ϑ, cell current I and voltage U. The safety zone guarantees a sufficient distance to the restricted zone. These thresholds have to be controlled by the BMU in order to ensure a long life-cycle.

3.1.2.5. Gearbox (GBX)

Gearboxes are essential in automotive drivetrains in order to achieve good vehicle performance concerning fuel efficiency and vehicle agility [53]. The main function of the GBX is to adapt the ICE torque and angular speed to the requested power at the wheels [110]. The GBX enables the ICE to operate over a wide vehicle speed area within its narrow speed range. The different types of gearboxes include manual automated transmissions, stepped-automatic transmissions, automated transmissions with hydrodynamic torque converter (German: Drehmomentwandler), continuously variable transmissions (CVTs) and dual clutch transmissions (DCTs). In this thesis, a gearbox model that considers the different gear ratios and the inertias at the input and output shafts is implemented. The first gear, which has the largest gear ratio, is often chosen to meet the towing requirements for climbing ability. Top speed or fuel economy aspects are the main design criteria of the highest gear, which has the lowest gear ratio [67]. Furthermore, the total gear spread φ_s also has to consider packaging limitations in addition to the towing and top speed requirements [52].

Besides the total gear spread φ_s, there exist two more design parameters. The ratio between two consecutive gears ratios φ_γ, which reads

$$\varphi_\gamma = \frac{i_\gamma}{i_{\gamma+1}}, \qquad \gamma = 1, ..., N_\gamma - 1 \tag{3.32}$$

where typical values for the φ_1 are in the range of 1.45 through 1.9 [52]. Consequently, the total gear ratio φ_s reads

$$\varphi_s = \prod_{\gamma=1}^{N_\gamma - 1} \varphi_\gamma, \tag{3.33}$$

where γ is the selected gear, and N_γ is the total number of gears. The second design

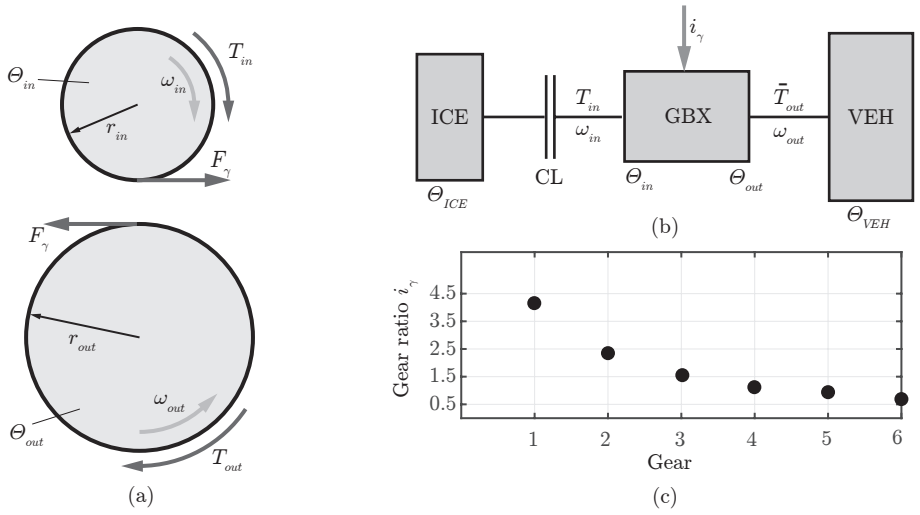

Figure 3.13.: Schematic representation of a single gear ratio and the gearbox model

Figure (a) shows a single gear ratio with its characteristic parameters. Figure (b) shows the gearbox model integrated in the drivetrain. The total moment of inertia of the vehicle is combined in Θ_{VEH}. The combination of clutch (CL) and gearbox (GBX) is often called transmission. Figure (c) shows the gear ratios i_γ for each individual gear.

criterion is the progression coefficient Ψ_γ, which reads

$$\Psi_\gamma = \frac{\varphi_\gamma}{\varphi_{\gamma+1}}, \qquad \gamma = 1, ..., N_\gamma - 2. \tag{3.34}$$

This design law avoids excessive gaps between two consecutive gears. If $\Psi_\gamma = 1$, a geometrical design is used. In practice, a gearbox design with constant progression factor ($\Psi_\gamma = \text{const}$) is often used [52]. Figure 3.13(b) depicts the implemented simplified transmission model. It consists of a clutch and a gearbox with different gear ratios i_γ.

The gear ratio i_γ in Figure 3.13(c) reads [52]

$$i_\gamma = \frac{T_{out}}{T_{in}} = \frac{\omega_{in}}{\omega_{out}} = \frac{r_{out}}{r_{in}}, \tag{3.35}$$

The variables T_{out} and T_{in} define the torques at the output and input shafts of the gearbox, respectively. The gearbox speeds at the input and output shafts are described by ω_{in} and ω_{out}. The parameters r_{out} and r_{in} are the radiuses of the corresponding gear. If the input and output shafts have opposite rotating directions, a negative sign has to be added.

Applying the conservation of angular momentum on the schematic representation in Figure 3.13(a) results in

$$\Theta_{in} \cdot \dot{\omega}_{in} = T_{in} - F_\gamma \cdot r_{in}, \tag{3.36}$$

$$\Theta_{out} \cdot \dot{\omega}_{out} = -T_{out} + F_\gamma \cdot r_{out}, \tag{3.37}$$

where F_γ is the gear force. Reformulating Eq. (3.36) and Eq. (3.37) and using the relation stated in Eq. (3.35) yields

$$F_\gamma = (T_{in} - \Theta_{in} \cdot \dot{\omega}_{in}) \cdot \frac{1}{r_{in}}, \tag{3.38}$$

$$T_{out} = -\Theta_{out} \cdot \dot{\omega}_{out} + F_\gamma \cdot r_{out}. \tag{3.39}$$

Eliminating F_γ, the torque and the angular speed at the output shaft read

$$T_{out} = T_{in} \cdot i_\gamma - (\Theta_{out} + \Theta_{in} \cdot i_\gamma^2) \cdot \dot{\omega}_{out}, \tag{3.40}$$

$$\omega_{out} = i_\gamma \cdot \omega_{in}. \tag{3.41}$$

The parameters $\Theta_{in/out}$ are the moments of inertia of the input/output shafts, and the force F_γ acts on both contacting tooth flanks. Although this simple model accounts for changing gear ratios, an overlapping gear-shifting mechanism, which is common in stepped-automatic and DCTs, cannot be considered [130]. Since analysing the shifting quality is not part of this thesis, the introduced model is sufficiently accurate. Equation (3.40) does not account for the gearbox efficiency. By introducing the gearbox efficiency η_{GBX}, the torque at the output shaft $\bar{T}_{out}$ is determined by

$$\bar{T}_{out} = \begin{cases} T_{out} \cdot \eta_{GBX}, & T_{out} \geq 0, \\ T_{out} \cdot \frac{1}{\eta_{GBX}}, & T_{out} < 0 \end{cases} . \tag{3.42}$$

The gearbox efficiency is assumed to be constant. Typical values are between 0.95 and 0.97 [69], [134]. In real transmissions, losses occur at various component parts, such as gears, bearings and sealings. These losses strongly depend on the load level, angular speed, temperature and operating time. Nevertheless, dissipative losses due to friction play a crucial role. At low loads, the gearbox efficiency is low, and it decreases further as the angular speed increases. At low speed and high loads, the best efficiency is reached [53].

Transmission Control Unit (TCU)

The transmission control unit (TCU) is responsible for controlling the GBX components. In automatic transmissions, the TCU takes over some driver functions, namely selection of a suitable gear, actuation of the clutch and the interference with the ICE. Since the interactions of the TCU are complex [53], the focus in this chapter is only on the shifting strategy. Its main objective is to sense and process all environmental conditions in order to choose a suitable gear for a certain driving situation. The shifting strategy can either focus on fuel consumption, traction or driving performance [53]. The main input signals for a conventional shifting strategy are the accelerator pedal p_p and the current vehicle velocity v_x. These inputs are used to determine the most suitable gear in a predefined gear-shifting map (cf. Figure 3.14). There are at least two different maps for upshifting

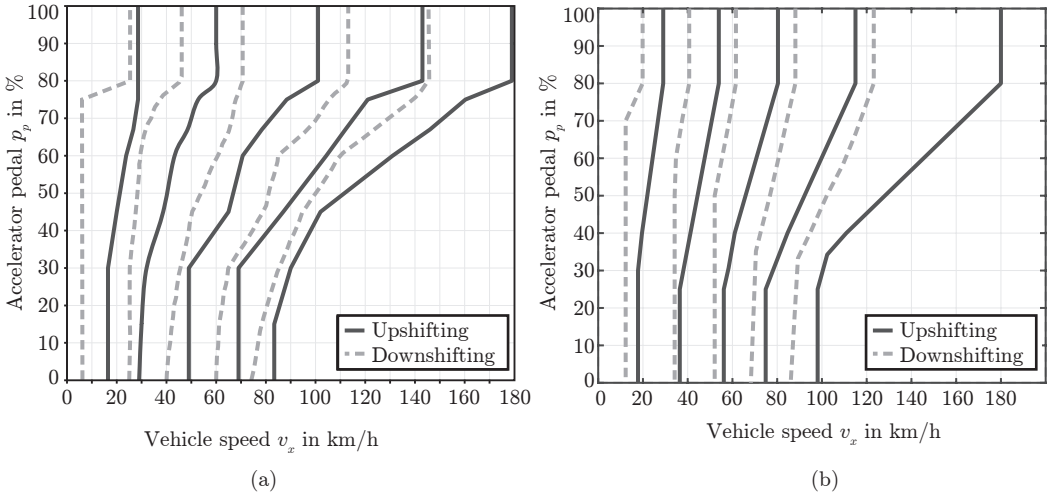

Figure 3.14.: Schematic representation of a conventional shifting strategy

Figure (a) shows an implemented shifting strategy of a real vehicle according to [53]. Figure (b) presents the simplified shifting strategy implemented here. In both cases, the kick-down function occurs at a pedal position of 80 %.

and downshifting, and the number grows with the number of different shifting modes. In general, the selected gear γ reads

$$\gamma = f(p_p, v_x). \tag{3.43}$$

Figure 3.14(a) depicts a conventional shifting strategy according to [53], while Figure 3.14(b) illustrates the simplified strategy implemented here. A hysteresis is implemented in order to avoid oscillating shifting behaviour. This conventional shifting strategy is often extended by additional functions [53], such as:

- *Kick-down function:*
  The shifting strategy is optimised to maximum engine power. The TCU detects a kick-down either by the position and gradient of the accelerator pedal p_p or by a switch. This mode also enables dual-downshifts and an upshift near the engine's maximum speed $\omega_{ICE,max}$.
- *Sport mode:*
  This mode enables higher engine revolutions; thus, the shifting strategy holds the gear for a longer time. The sport mode can be selected by the driver via a switch, or it can be selected by a self-learning algorithm.
- *Load detection:*
  This function detects the current vehicle load and switches to a traction-optimal shifting strategy. Consequently, gear hunting[10] can be avoided.

[10] Also known as oscillating gear-shifting behaviour

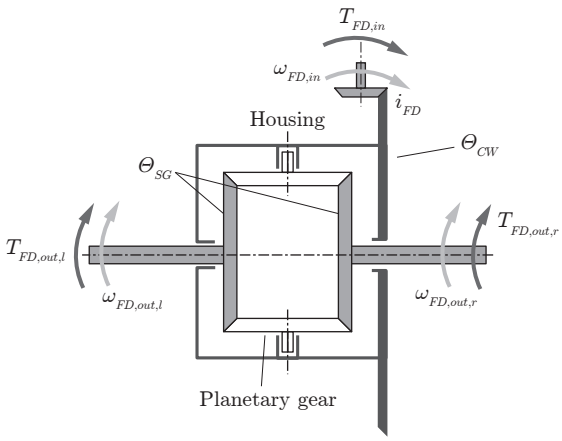

Figure 3.15.: Schematic representation of a final drive

The final drive balances the wheel speeds of the driven axles $\omega_{FD,out,l/r}$. It is modelled by four rigid bodies: the crown wheel (CW) and housing, the input shaft with pinion, and the left and right output shafts with pinion or sun gears (SGs).

- *Tyre slip detection:*
  This mode interacts with the electronic stability program (ESP) and the anti-lock braking system (ABS) in order to detect spinning or locking wheels.

The implemented shifting strategy covers a kick-down function (realised with the position of the accelerator pedal p_p) and two operating modes (economy and sport mode). To ensure fast shifting and high shifting quality, the TCU is able to systematically influence the propulsion torque. Gear hunting is avoided by using a shifting hysteresis between upshifting and downshifting, see Figure 3.14(b).

3.1.2.6. Final Drive (FD)

The main function of the final drive (cf. Figure 3.15) is to balance the wheel speeds of the driven axles. The torque distribution is permanently equally distributed. Furthermore, a gear ratio i_{FD} between 2.6 to 4.5 is often used [110]. If there is no speed difference between the driven wheels, the pinion gears (sun and planetary gears) of the final drive in Figure 3.15 do not move. However, if a speed difference occurs, such as during cornering, unequal dynamic tyre radiuses of the driven axle, or different tyre grip potential (such as μ-split surfaces[11]), the pinion gears (sun and planetary gears) start to move, and mechanical power is shifted [53]. In order to avoid excessive traction losses, mechanically and electrically actuated differential locks or advanced traction control systems (TCSs) can be used.

[11] A road condition where the friction significantly differs between the left and right wheelpaths, e.g., a wet road which has dried along a central area

Figure 3.15 shows a schematic illustration of a final drive. It consists of a crown wheel (CW), sun gears (SGs), planetary gears and a housing. Omitting the masses and inertias of the planetary gears, the mechanical characteristics of the final drive reads:

$$\begin{bmatrix} \Theta_{SG,l} + \frac{1}{4}\Theta^* & \frac{1}{4}\Theta^* \\ \frac{1}{4}\Theta^* & \Theta_{SG,r} + \frac{1}{4}\Theta^* \end{bmatrix} \begin{bmatrix} \dot{\omega}_{FD,out,l} \\ \dot{\omega}_{FD,out,r} \end{bmatrix} = \begin{bmatrix} T_{FD,out,l} \frac{1}{2} i_{FD} T_{FD,in} \\ T_{FD,out,r} + \frac{1}{2} i_{FD} T_{FD,in} \end{bmatrix} \tag{3.44}$$

where $\Theta_{SG,l}$ and $\Theta_{SG,r}$ are the moments of inertia of the left and right sun gears, and $\Theta^* = \Theta_{CW} + i_{FD}^2 \Theta_{FD,in}$ combines the inertias of the crown wheel Θ_{CW} and of the input gear $\Theta_{FD,in}$.

Since the simulation environment only consists of a longitudinal vehicle model, the wheel speed balancing is neglected and a rigid axle is modelled. Moreover, component inertias are neglected. Thus, the model yields the following equations:

$$T_{FD,out,l/r} = \frac{1}{2} \cdot i_{FD} \cdot T_{FD,in} \cdot \eta_{FD}, \tag{3.45}$$

$$\omega_{FD,in} = \frac{i_{FD}}{2} (\omega_{FD,out,l} + \omega_{FD,out,r}). \tag{3.46}$$

The final drive efficiency η_{FD} is assumed to be in the same range as the transmission efficiency η_{GBX}, but a bit lower, since a bevel gear is used [143]. The ratio of the final drive i_{FD} defines the maximum vehicle speed and is supposed to be in the range of 2.5 to 5.5, according to [142]. Considering the final drive efficiency, the actual output torque $\bar{T}_{FD,out,l/r}$ reads:

$$\bar{T}_{FD,out,l/r} = \begin{cases} T_{FD,out,l/r} \cdot \eta_{FD}, & T_{FD,out,l/r} \geq 0, \\ T_{FD,out,l/r} \cdot \frac{1}{\eta_{FD}}, & T_{FD,out,l/r} < 0 \end{cases} . \tag{3.47}$$

3.1.2.7. Tyre

Tyres are the link between the vehicle and the ground and are responsible for transmitting all forces and torques to the ground. Consequently, in vehicle dynamics modelling, a sufficient description of the interaction between tyre and road is essential [74]. According to [75], there are three different tyre models:

- Physical tyre model: RMOD-K [150], FTire [58]
- Semi-physical tyre model: TMeasy [74], TMsimple [73]
- Empirical-mathematical tyre model: Magic Formula [154], IPG-Tire [175]

The tyre model should consider the main tyre characteristics and should allow fast simulation with a lean parameter set of physical meaning for easier interpretation and parametrisation. The semi-physical model TMsimple [73] is used in this thesis. The

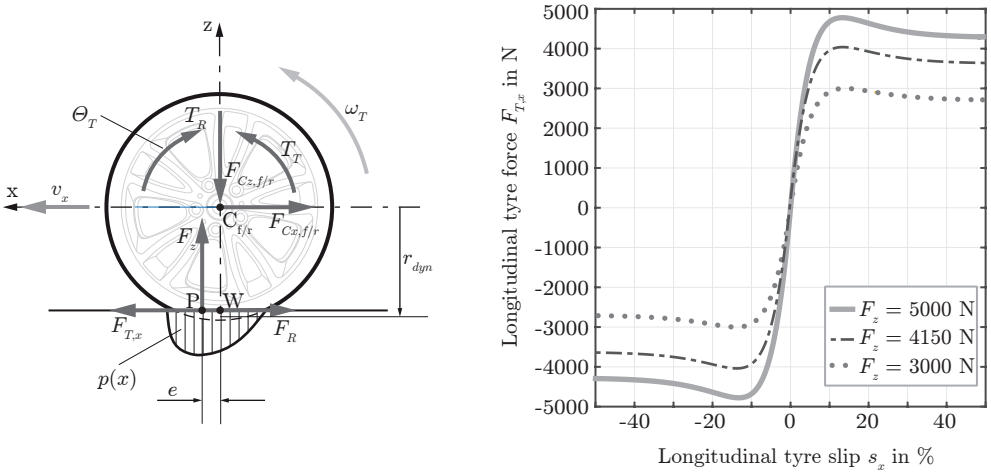

Figure 3.16.: Tyre characteristics with their tyre dynamics

Figure (a) shows a free body diagram of the tyre with its characteristic values. It shows the cutting forces $F_{Cz,f/r}$ and $F_{Cx,f/r}$ in the tyre centre $C_{f/r}$, the torque acting on the tyres T_T, and the rolling resistance torque T_R. The rolling resistance torque T_R arises due to the visco-elastic deformation in the tyre contact area. This results in an asymmetric pressure distribution $p(x)$, which is characterised by the eccentricity e. The transferable longitudinal tyre force $F_{T,x}$ depending on the vertical tyre load F_z is depicted in Figure (b). The dotted-dashed line ($F_z = 4150\,\mathrm{N}$) represents the static vertical tyre load at the rear wheels. Higher vertical loads occur during acceleration, whereas deceleration lowers $F_{T,x}$ at the rear wheels. At the front wheels, the opposite is true.

tyre dynamics according to Figure 3.16(a) are

$$\Theta_T \cdot \dot{\omega}_T = T_T - F_{T,x} \cdot r_{dyn} - \overbrace{\underbrace{F_z \cdot a_R}_{F_R} \cdot r_{dyn}}^{T_R}, \tag{3.48}$$

where Θ_T is the inertia of the tyre, T_T is the torque acting on the tyre, $F_{T,x}$ is the longitudinal tyre force, r_{dyn} is the dynamic tyre radius, F_z is the vertical tyre load, and a_R is the rolling resistance coefficient. The increasing dynamic tyre radius r_{dyn} due to higher velocities [75] is neglected. The longitudinal tyre slip s_x reads

$$s_x = \begin{cases} \frac{v_s}{\omega_T \cdot r_{dyn}} & T_T \geq 0, \\ \frac{v_s}{v_x} & T_T < 0. \end{cases} \tag{3.49}$$

where $v_s = \omega_T \cdot r_{dyn} - v_x$ is the slip velocity at the wheel W within the tyre contact area. The available longitudinal grip potential $F_{T,x}$ only depends on the longitudinal tyre slip s_x and the vertical tyre load $F_{T,z}$, assuming other influences (e.g., temperature, road surface, tyre pressure) are kept constant [75]. In the TMsimple approach, the

longitudinal tyre characteristics are calculated by

$$F_{T,x} = B_1 \cdot \sin\left[B_2 \left(1 - e^{\frac{-|s_x|}{B_3}}\right) \operatorname{sign}(s_x)\right], \tag{3.50}$$

where the coefficients read

$$B_1 = F_{x,max}, \tag{3.51}$$

$$B_2 = \pi - \arcsin \frac{F_{x,\infty}}{F_{x,max}}, \tag{3.52}$$

$$B_3 = \frac{1}{dF_{x0}} B_1 \cdot B_2. \tag{3.53}$$

For a given vertical load F_z, the parameter $F_{x,max}$ describes the maximum longitudinal tyre force, $F_{x,\infty}$ is the saturation value, and dF_{x0} is the initial longitudinal tyre stiffness. The degressive influence of the vertical tyre load F_z is considered with the following approach

$$F_{x,max}(F_z) = b_1 \frac{F_z}{F_{z,nom}} + b_2 \left(\frac{F_z}{F_{z,nom}}\right)^2, \tag{3.54}$$

$$F_{x,\infty}(F_z) = b_3 \frac{F_z}{F_{z,nom}} + b_4 \left(\frac{F_z}{F_{z,nom}}\right)^2 \tag{3.55}$$

$$dF_{x0}(F_z) = b_5 \frac{F_z}{F_{z,nom}} + b_6 \left(\frac{F_z}{F_{z,nom}}\right)^2. \tag{3.56}$$

The coefficients b_1 and b_2 are calculated by

$$b_1 = 2 \cdot F_{x,max}^{F_{z,nom}} - 0.5 \cdot F_{x,max}^{2F_{z,nom}}, \tag{3.57}$$

$$b_2 = 0.5 \cdot F_{x,max}^{2F_{z,nom}} - F_{x,max}^{F_{z,nom}}. \tag{3.58}$$

The same procedure has to be carried out in order to obtain the coefficients b_3, b_4 and b_5, b_6, but instead of using $F_{x,max}^{F_{z,nom}}, F_{x,max}^{2F_{z,nom}}$, the saturation value $F_{x,\infty}$ and the initial tyre stiffness dF_{x0} at the nominal load $F_{z,nom}$ and twice the nominal load $2F_{z,nom}$ have to be used. Figure 3.16(b) shows an example of the characteristic longitudinal tyre forces depending on the vertical tyre load.

Rolling resistance F_R

The rolling resistance of tyres is an important factor for increasing the fuel economy of vehicles. Therefore, many highly environmentally friendly vehicles use rolling-resistance-optimised tyres [201]. The resulting force F_R can be calculated by

$$F_R = a_R \cdot m_{VEH} \cdot g \cdot \cos\beta. \tag{3.59}$$

Table 3.1.: Characteristic values of the rolling resistance coefficient a_R, adapted from [141]

Road surface	a_R
Smooth asphalt road	0.010
Concrete road	0.011
Rough concrete road	0.014
Good paving	0.020
Rutted road	0.035

The parameter a_R describes the rolling resistance coefficient. The rolling resistance arises due to the visco-elastic deformation in the tyre contact area. This results in an asymmetric pressure distribution $p(x)$ and causes the rolling resistance [135], cf. Figure 3.16. Equation (3.59) is only valid if the rolling resistance is the same for all tyres. The rolling resistance coefficient a_R is defined by

$$a_R = \frac{e}{r_{dyn}}, \tag{3.60}$$

where e is the eccentricity, which defines the position where the resistance acts. The coefficient strongly depends on the current road surface and increases with increasing vehicle speed [76], [135]. In this thesis, the speed dependency of a_R is neglected. Tables 3.1 and 4.2 summarise typical values for the rolling resistance coefficient a_R.

3.1.2.8. Vehicle Model

The available longitudinal tyre force $F_{T,x}$ at the wheels results in a longitudinal vehicle acceleration according to Newton's second law (see Figure 3.17):

$$m_{VEH} \cdot a_x = F_{T,x} - F_D - F_\beta, \tag{3.61}$$

where m_{VEH} is the total vehicle mass including the additional weight of the hybrid system components, a_x is the longitudinal vehicle acceleration due to the forces acting at the vehicle body, $F_{T,x}$ is the total propulsion force of the tyres, F_D is the air drag, and F_β is the resistance due to the road inclination. The braking force acts directly on the wheels, whereas the propulsion force $F_{T,x}$ is transmitted through the entire drivetrain. The rolling resistance F_R is considered in the tyre model, see Eq. (3.48).

Air drag F_D

The influence of aerodynamics on the performance and fuel efficiency of passenger vehicles increases with increasing vehicle speed. The reduction of the aerodynamic drag is

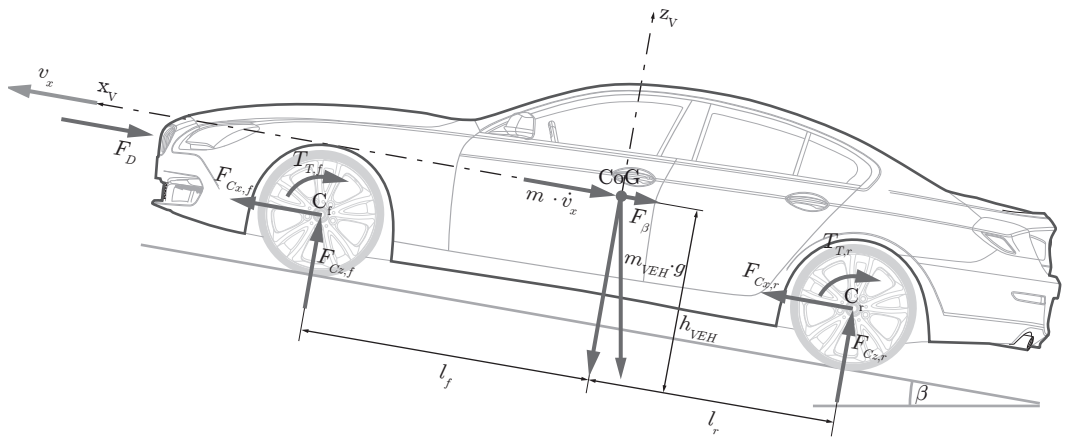

Figure 3.17.: The free body diagram of the vehicle model

This figure shows all forces acting on the chassis. The tyre hub $C_{f,r}$ transmits all forces of the tyres, shown in Figure 3.16. The air drag F_D acts on the chassis. The entire vehicle mass m_{VEH} is combined in the centre of gravity (CoG). Moreover, the resistance F_β due to the road inclination β also acts in the CoG. The CoG is charactersied by the distances l_f, l_r and its height h_{VEH}.

one objective in developing low-emission vehicles [174].

$$F_D = \frac{1}{2} \cdot c_D \cdot \rho_a \cdot A_x \cdot v_x \cdot |v_x|, \tag{3.62}$$

The flow resistance is described with the dimensionless air resistance coefficient c_D, and ρ_a is the density of the air, which is assumed to be constant ($\rho_a = 1.199\,\mathrm{kg/m^3}$)[12]. The parameter A_x represents the frontal area of the vehicle. The lateral and vertical air resistance properties are not considered in this thesis. The aerodynamic factor mainly depends on the shape of the vehicle [132]. The chosen reference point is often on the road surface in the middle of wheelbase and track width [132]. Table 3.2 lists characteristic values for c_D and A_x for different vehicles, adapted from [141].

Resistance due to road inclination F_β

Currently, legally stipulated driving cycles do not consider any road inclination. Nevertheless, in real-world driving cycles, the height profile cannot be neglected, since it strongly influences the performance of the vehicle. The resistance due to the road inclination F_β reads

$$F_\beta = m_{VEH} \cdot g \cdot \sin\beta, \tag{3.63}$$

[12]For an air pressure of 1.013 bar, a relative humidity of 60 % and an air temperature of 20 °C [141]

Table 3.2.: Characteristic values c_D and A_x of the air drag F_D, adapted from [141]

Vehicle	c_D	A_x in m^2	$c_D A_x$ in m^2
Convertible	**0.29-0.53**	**1.58-2.90**	**0.58-1.54**
Mercedes-Benz SL 500			
-Open top	0.34	2.00	0.68
-Closed top	0.29	2.00	0.58
Sedan/SUV	**0.25-0.39**	**1.97-2.90**	**0.5-1.54**
Audi A6 Avant	0.31	2.26	0.70
Mercedes-Benz S320 CDI	0.26	2.40	0.62
BMW 645i	0.29	2.15	0.62
Mercedes-Benz ML 280 CDI	0.34	2.81	0.96
Porsche Cayenne Turbo	0.39	2.78	1.09

where g is the acceleration due to gravity, and β is the inclination of the road ahead.

3.1.2.9. Driver Model

In the dynamic vehicle simulation, a driver model is needed to follow a certain desired speed profile. Modelling the behaviour of the driver is an ongoing research topic, and different levels of complexity are available. The control behaviour of humans depends on physical and psychological factors, as well as the current demands of the driving situation. The individual driving behaviour is often modelled using classical control theory or fuzzy logic theory [104].

A PID-controller is sufficient to control the vehicle speed [104] in closed-loop vehicle-driver simulations. The driving task is divided into a longitudinal and a lateral proportion [40]. The implemented driver model uses a control approach which only focuses on longitudinal driving, e.g., maintaining the predefined acceleration and vehicle speed. However, human behaviour is not a technical controller. In fact, real drivers have to manage multiple driving tasks, such as speed control, with frequently changing priorities. These tasks can be compressed into three main activities occurring simultaneously during a trip. Thus, prioritisation is mandatory [104]:

- *Navigation level:*
  This level involves the choice of the optimal route before the trip starts in order to accomplish the transportation task; for instance, deciding to travel on the motorway to reach the desired destination.
- *Guidance level:*
  This layer ensures that the driver adapts their driving to the current road and traffic conditions. Moreover, the driver controls the position, speed and direction of the vehicle. Thus, at the course guidance level, the driver selects the desired

trajectory, e.g., drive at 100 km/h and overtake another car.

- *Stabilisation level:*
  This level has the highest priority and controls pedal position or steering-wheel angel. Moreover, it has to compensate for short-term disturbances, such as stabilisation of the vehicle during immediate over-steering.

All three levels are based on the human perception of environment and vehicle. The implemented controller compares the actual v_x with the desired vehicle speed v_{x0} and calculates a required accelerator pedal p_p or brake pedal position to minimise the speed difference. In this thesis, the pedal position is within the interval $[-1 \quad 1]$, a positive value accounts for the accelerator pedal position, and a negative value is a brake pedal signal. Hence, in the implemented model, concurrent activation of the brake and accelerator pedal is not permitted. The values of control parameters of the PID-controller are determined by empirical methods in order to follow the desired speed profile with sufficient accuracy. These parameters vary with different driving cycles [136]. Furthermore, a feedforward-controller may be implemented to enable high control dynamics.

In commercially available simulation tools, the structure, parameters and hence the complexity of the driver models can be adapted to the particular research objectives. In general, the inputs of a driver model are the pedal position, steering-wheel angle, and gear choice. For further information, cf. [145], [147].

3.1.2.10. Hybrid Control Unit (HCU)

The HCU has to ensure that the power of the different propulsion units is distributed in an efficient manner. One key success factor for HEVs is the operation strategy. Besides determining the power distribution, the operation strategy directly influences drivability and efficient energy consumption. The simulation environment uses two different kinds of operation strategies. A *rule-based* operation strategy (cf. Chapter 2.2), is used as a baseline strategy. It uses the electric energy in the battery as often as possible, assuming no constraints are harmed. In the literature, this strategy is known as a *charge-depleting* [24] approach. After the SOC of the battery is at its lower allowable threshold SOC_{min}, the operation strategy turns to a *charge-sustaining* [24], [183] strategy. This operation strategy uses the current driving state in order to select a suitable driving mode. No additional information about the upcoming driving route is used. Besides the power distribution, the HCU controls the state of the ICE and the clutch between the ICE and the EMG. The rule-based operation strategy used here minimises the instantaneous fuel consumption $\dot{m}_f$ by maximising the electric propulsion share. This results in

$$\min_{u(t)} \dot{m}_f \Big(x(t), u_d(t), t \Big) \Rightarrow \max u_d(t), \tag{3.64}$$

where $x(t)$ is the current vehicle state, and $u_d(t)$ denotes the power distribution factor – a specific control variable $u(t)$. Pure electric driving is characterised by $u_d = 1$, pure ICE

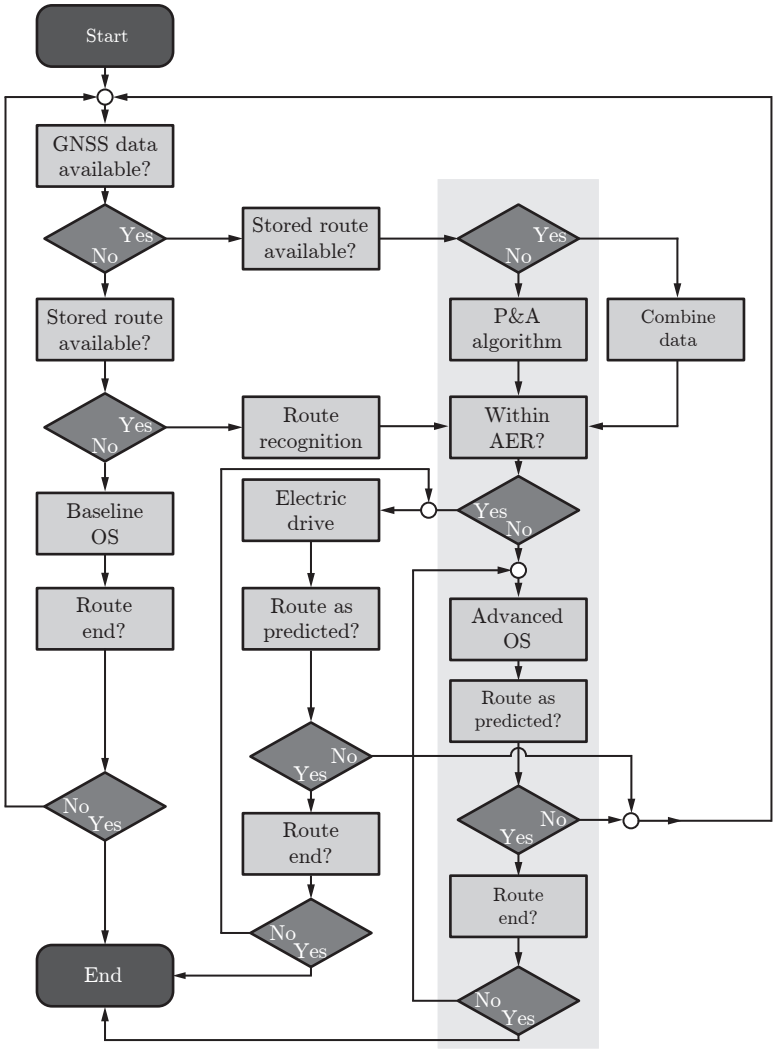

Figure 3.18.: Innovative holistic energy management controller

The controller consists of three control paths, depending on the additional information available. If no additional information is available, the OS uses its baseline strategy, which operates according to predefined rules. If a frequently driven route is recognised and/or input data from the navigation system and GNSS signals are available, this additional information is used to enhance the fuel saving potential of PHEVs. For distances within the AER, pure electric driving is selected, as long as no system boundaries are exceeded. This thesis focuses on the third control path, highlighted in grey. The advanced prediction and adaptation (P&A) algorithm uses data from the navigation system and GNSS signals and combines that data with the individual driving behaviour in order to improve the long-term prediction accuracy.

driving by $u_d = 0$, and values between indicate hybrid driving. In the charge-sustaining operation mode, the battery is only charged via recuperated braking energy. It is obvious, that such an operation achieves fossil fuel savings, but since no additional information is considered, it does not utilise the entire fuel saving potential. No load point shifting is considered.

The baseline strategy is also used in the proposed novel holistic energy management controller (see Figure 3.18). It considers three different information levels, depending on the data available. If no additional information about the route ahead is available, the aforementioned RB-OS is used. If a frequently driven route is recognised, the stored data about the route is used to enable additional fuel saving potential. If input data from a navigation system and GNSS signals are available, the advanced P&A algorithm further enhances the fuel efficiency of PHEVs. If both GNSS with digital map data and stored routes are available, the advanced OS combines both data. For all routes within the AER, the electric drive mode is used. The focus of the present thesis is on utilising additional data from a navigation system and GNSS signals, the grey highlighted control path in Figure 3.18. The route recognition algorithm detects characteristic data during driving and compares that data with the stored routes [93]. Nevertheless, the route recognition algorithm is not part of this thesis. It is used to get an idea of how the whole energy management algorithm works. The structure of the energy management controller enables the use of other information from advanced communication technologies, such as ITS or GIS. Nevertheless, this additional information is not required in order to improve the fuel efficiency. The output of the holistic energy management controller is the requested EMG and ICE torque $T_{EMG,req}$ and $T_{ICE,req}$ based on the power distribution factor u_d.

3.1.2.11. Auxiliaries (AUX)

In conventional engine-driven vehicles, the ICE has to guarantee the proper operation of different AUXs. Although the ICE may be switched off over a long time period in HEVs, AUXs such as the power steering pump, brake booster, heating and A/C have to operate properly. Consequently, in HEVs these AUXs are electrified. In addition, the on-board vehicle electrical system (e.g., interior convenience functions and control units) has to be modified. A conventional alternator alone may not ensure a constant power level. The total AUX power depends on the ambient temperature and other vehicle/driver individual settings. The present thesis does not consider AUXs due to comparison reasons – their power demand may vary on the same road due to switching on/off the A/C, for instance.

3.1.3. Quasi-static Vehicle Modelling Approach

The proposed simulation environment uses model-based control with a quasi-static vehicle model. As mentioned in Chapter 3.1.1, this model approach is unable to consider any drivetrain dynamics and requires information about the entire driving cycle a-priori.

This chapter presents the main differences in the component modelling and describes the implemented first-order vehicle model. The result of the model-based optimisation (cf. Chapter 3.2) is the trajectory of the energy content of the battery, which leads to an optimal fossil fuel consumption. Therefore, the battery's SOC is used as the only state variable x.

$$x(t) \equiv SOC(t) = x_0 + \frac{1}{Q_{nom}} \int_0^{t_e} (I_{ES} + I_{BAT})\ \mathrm{d}t, \tag{3.65}$$

where x_0 is the initial SOC = SOC_0 of the battery, Q_{nom} is the nominal capacity of the battery, I_{ES} is the vehicle electrical system current, and I_{BAT} is the current needed for propulsion. Therefore, the first-order vehicle model reads

$$\dot{x}(t) = f\Big(x(t), u(t), t\Big) \equiv \dot{SOC}(t) = f\Big(SOC(t), u_d(t), t\Big). \tag{3.66}$$

Figure 3.10(b) shows the quasi-static battery model used here. It consists of an internal resistance R_i and an ideal open-circuit voltage source U_{oc}, both of which depend on the current SOC. Using Kirchhoff's voltage law yields

$$U_{oc} - R_i \cdot I_{BAT} - U_{BAT+ES} = 0. \tag{3.67}$$

Applying the total electrical power P_{BAT+ES} instead of the voltage U_{BAT} results in

$$U_{oc} - R_i \cdot I_{BAT} - \frac{P_{EMG} + P_{ES}}{I_{BAT}} = 0. \tag{3.68}$$

Multiplying Eq. (3.68) with I_{BAT} and solving the equation for I_{BAT} results in[13]

$$I_{BAT} = \frac{U_{oc} - \sqrt{U_{oc}^2 - 4 \cdot (P_{EMG} + P_{ES}) \cdot R_i}}{2 \cdot R_i} \tag{3.69}$$

A positive current I_{BAT} indicates a discharging process and vice versa.

The EMG is phenomenologically modelled using the same approach as stated in Chapter 3.1.2.3. Nevertheless, the response characteristics and the power flow are adapted to the quasi-static vehicle model approach. The ICE model is based on a mean value model with ideal system response. The calculation of the average fuel consumption over 100 km was described in Chapter 3.1.2.1.

The torque share at the gearbox input shaft is evaluated with the power distribution factor u_d (cf. Chapter 3.2). It reads

$$u_d = \frac{T_{EMG}}{T_{GBX}} \qquad T_{GBX} \neq 0, \tag{3.70}$$

where u_d defines the share of the EMG on the whole propulsion torque, that is $0 \leq u_d(t) \leq 1$. The case $T_{GBX} = 0$ is irrelevant, since any propulsion torque has to be split.

[13] The solution with a "+" before the square root is neglected, since only the equation shown leads to zero current I_{BAT} when no power is demanded $P_{BAT} + P_{ES} = 0$.

If $u_d = 1$, the propulsion is provided fully electrically – the ICE is switched off, and the clutch opens.

In contrast, the gear-shifting logic depends on the rotational speed at the wheels ω_T and the corresponding wheel torque T_T. Gear change happens instantaneously, and no delay is considered. A gear change results in a volatile change of the gear ratio i_γ. Therefore, the engine speed and torque also change abruptly. The gear selection ensures that the required torque can be accomplished by the ICE only and that the speed limits are not exceeded. If several gears are applicable, the highest possible gear is chosen. This gear-shifting strategy is expected to be a good heuristic approach in terms of fuel efficiency and is sufficiently accurate compared to a more realistic shifting logic implemented in the dynamic drivetrain model.

Roll, air, slope and acceleration resistance forces act on the vehicle chassis, depending on the vehicle speed v_x, acceleration a_x and the road inclination β . To maintain the desired vehicle speed, the torque at the wheels T_T has to be equal to the total driving resistance torque. Since sufficient contact forces between the tyres and the road are assumed, T_T reads

$$T_T = (F_D + F_R + F_\beta + F_A + F_B) \cdot r_{dyn}. \tag{3.71}$$

Furthermore, the backward vehicle model considers the different component efficiencies, the current limitation of the battery, and the rotational masses of the drivetrain. More detailed information is given in [80].

3.1.4. Investigated Simulation Model

In this thesis, a medium-sized passenger car with a total curb weight of about 1500 kg is investigated. Additional weight is added due to the hybrid drivetrain components. Figure 3.19 shows the investigated HEV model. The conventional drivetrain consists of a four-cylinder diesel engine. It has a maximum ICE power $P_{ICE,max}$ of about 120 kW. The vehicle also has a six-speed automatic transmission. The conventional drivetrain is extended by an additional clutch (CL_{II}), a clutch actuator, a power electronic unit, an EMG and a high-capacity battery (BAT). Since the EMG is mounted between the ICE and the starting clutch (CL_I), a P2 layout is modelled. The clutch (CL_I) enables an additional DoF in controlling the propulsion units and avoids ICE drag losses during pure electric driving. The hybridisation degree according to [66], [81] is approximately 70 %. The battery pack only uses cells in series layout, and its total energy content is about 9 kWh. The usable energy content depends on the SOC limits, which should ensure a long battery life-cycle. The HEV can be recharged by an external outlet. Thus, the investigated vehicle is a P2-PHEV.

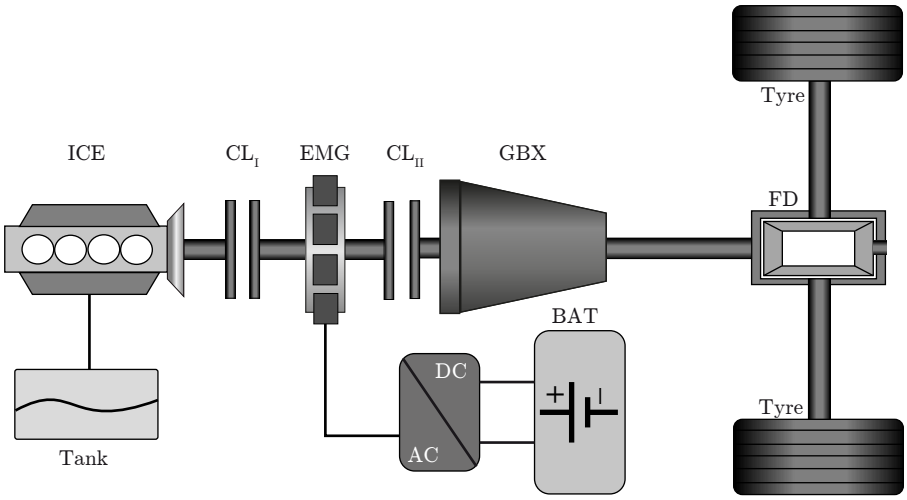

Figure 3.19.: Investigated PHEV drivetrain layout

A P2 layout where the EMG is mounted between the starting clutch (CL_I) and the gearbox (GBX). An additional clutch (CL_{II}) enables charging the battery during standstill. Due to the high battery capacity and the possibility to recharge it from external outlets, the investigated vehicle model is a P2-PHEV.

3.2. Optimisation – Dynamic Programming

Optimisation is a widespread interdisciplinary field with applications ranging from economics to engineering science. It is a powerful tool for comparing the effectiveness of different decisions. In general, optimisation can be described as a *decision making process* which systematically determines the optimal option while taking into consideration certain objectives and limitations [156]. The broad field of optimisation can be divided into *analytical* and *numerical* methods. Moreover, practitioners in the field [156] distinguish between *static*, *dynamic* and *stochastic* optimisation methods. This brief summary highlights the broad application area and the huge number of different methods used. However, this thesis focuses on one numerical, dynamic approach called *dynamic programming* (DP). Hereafter, all mentions of DP refer to the deterministic dynamic programming approach.[14]

Dynamic programming was developed in the 1950s by Richard Bellman and his assistants. It is a flexible and powerful method for solving non-linear, non-convex *multi-stage decision processes*. Instead of tackling the whole multi-stage decision process at once, DP reduces the dimension by introducing a new problem formulation [17]. In the context of the present thesis, DP is used to solve optimal control problems. Consequently, the remainder of this chapter focuses exclusively on such control problems.

3.2.1. Introduction

Generally, an optimal control problem needs an optimisation criterion – a cost functional[15]. Once a suitable cost functional has been chosen, the optimisation algorithm has to select control variables such that the optimisation criterion reaches its minimum or maximum[16]. According to [55], two main approaches can be distinguished in optimal control theory:

1. *Parameter optimisation:*
   This optimisation problem is characterised by a predefined controller structure. Only the controller's parameters are varied to solve the optimisation problem.

2. *Structure optimisation:*
   In contrast to *parameter optimisation*, there is no predefined controller structure. The aim of the optimisation problem is to find a control structure that will minimise the cost functional. Such control problems consist of a mathematical model of the control process and an objective function.

[14] Dynamic programming can be divided into deterministic and stochastic approaches.

[15] Also called cost-to-go, objective function [193], criterion function [18], or return function [16]. The value of this function is often called return [16].

[16] Whether it is minimum or maximum depends on the definition of the cost-to-go function. Mathematically, a minimum can be transformed into a maximum by changing the sign of the cost functional.

In the following chapters, all mentions of optimisation, and especially *dynamic programming*, refer to *structure optimisation*. The continuous-time control process (i.e., dynamic system) can be written in state space form to:

$$\dot{\mathbf{x}}(t) = \mathbf{f}\Big(\mathbf{x}(t), \mathbf{u}(t), t\Big), \quad t \geq t_0 \tag{3.72}$$

where $\mathbf{x}(t)$ is the state vector, $\dot{\mathbf{x}}(t)$ is the temporal change of the state vector, and $\mathbf{u}(t)$ is the control vector at time t. The initial moment of time is defined as t_0. At the terminal moment of time t_e, the state vector $\mathbf{x}(t)$ has to reach a predefined terminal vector $\mathbf{x}_e$. There are an infinite number of policies (also called control laws) $\boldsymbol{\pi} = \Big(\boldsymbol{\mu}(t)\Big)$, which transform the initial state $\mathbf{x}_0$ to the desired terminal state $\mathbf{x}_e$. All policies that comply with the relevant constraints are called *admissible*, [16] and [22]. Actually, a policy is a determination of the control vector $\mathbf{u}(t)$ as a function of the state vector $\mathbf{x}(t)$ and the time t [16]

$$\mathbf{u}(t) = \boldsymbol{\mu}(\mathbf{x}, t). \tag{3.73}$$

With a cost functional J, the many policies are reduced to an optimal policy $\boldsymbol{\pi}^*$[17]. The selection of J effects the optimisation result. Consequently, there are several different cost functionals, depending on certain problems (cf. Appendix B.1). With the help of a predefined dynamic system, see Eq. (3.72), and a cost functional, the general formulation of a continuous-time optimisation problem COP can be written as an optimal control problem:

$$\min_{\mathbf{u}(t)} \left\{ g\Big(\mathbf{x}(t_e), t_e\Big) + \int_{t_0}^{t_e} h\Big(\mathbf{x}(t), \mathbf{u}(t), t\Big) \mathrm{d}t \right\} \tag{3.74}$$

$$\dot{\mathbf{x}}(t) = \mathbf{f}\Big(\mathbf{x}(t), \mathbf{u}(t), t\Big) \tag{3.75}$$

$$\mathbf{x}(0) = \mathbf{x}_0 \tag{3.76}$$

$$\mathbf{x}(t_e) \in \mathbb{X}_e \subseteq \mathbb{R}^n \tag{3.77}$$

$$\mathbf{x}(t) \in \mathbb{X}(t) \subseteq \mathbb{R}^n \tag{3.78}$$

$$\mathbf{u}(t) \in \mathbb{U}(t) \subseteq \mathbb{R}^m, \tag{3.79}$$

(COP)

where Eq. (3.75) describes the continuous-time dynamic model, and Eq. (3.76) and Eq. (3.77) describe the initial and terminal states, respectively. The terminal states have to be within the terminal space $\mathbb{X}_e$. The constraints of the state vector $\mathbf{x}(t)$ and the control vector $\mathbf{u}(t)$ are stated in Eq. (3.78) and Eq. (3.79), respectively. The functions $h(\,)$ and $g(\,)$ are defined by the original optimisation problem.

Since *dynamic programming* is a discrete optimisation method, the continuous-time model in Eq. (3.75) has to be discretized in time first, see Eq. (3.80). Thus, the discrete-time optimisation problem is represented by

$$\mathbf{x}_{k+1} = \mathbf{f}_k(\mathbf{x}_k, \mathbf{u}_k), \qquad k = 0, 1, ..., N-1. \tag{3.80}$$

[17] $()^*$ always denotes values related to the optimal control solution.

where $\mathbf{f}_k$ is a specific function depending on the state variables $\mathbf{x}_k$ and the control variables $\mathbf{u}_k$. The index k indicates that the structure of the function may be different in different time steps. Its optimal[18] cost functional based on the notation in [193] reads

$$J_k^* = \min_{u_k} \left\{ \underbrace{g_N(\mathbf{x}_N) + \phi_N(\mathbf{x}_N)}_{I_N} + \sum_{k=0}^{N-1} \underbrace{h_k(\mathbf{x}_k, \mathbf{u}_k) + \phi_k(\mathbf{x}_k)}_{I_k} \right\} \tag{3.81}$$

where I_N represents the final instantaneous cost-to-go at stage $k = N$ with its assessment of the final states $g_N(\mathbf{x}_N)$ similar to $g\Big(\mathbf{x}(t_e), t_e\Big)$ in Eq. (3.74). The term I_k describes the instantaneous costs at stage $k = 0, 1, ..., N-1$, with the function $h_k(\,)$ accounting for the costs of applying the control vector $\mathbf{u}_k$ at the current states $\mathbf{x}_k$. The term $\phi_k(\mathbf{x}_k)$ describes a penalty function to fulfil the discrete state constraints $\mathbf{x}_k \in \mathbb{X}_k$ at $k = 0, 1, ..., N$, see Eq. (3.77) and Eq. (3.78).

The discrete-time system $\mathbf{x}_{k+1}$ in Eq. (3.80) is called a *multi-stage decision process* if at each stage k the system undergoes a transformation – also called *decision* – in its states. In a conventional optimisation approach[19], the entire multi-stage decision process is considered as essentially one stage. This increases the dimension of the problem. In contrast, DP reduces the dimension of the process by "understanding" the *structure* of the problem [17]. The multi-stage problem is then reduced to a number of single-stage problems. *Multi-stage decision processes* have some features in common [55]:

- There is a physical system, see Eq. (3.80), which is described by some state variables $\mathbf{x}_k$ at any stage k.
- At each stage k, a number of choices $\mathbf{u}_k$ can be made in order to transform the system into other states $\mathbf{x}_{k+1}$.
- The past history of the system is of no importance in determining future actions; only the current stage is important.
- The purpose of the process is to minimise/maximise some functions of the state variables.

Before using these features to formulate the *dynamic programming* algorithm, the advantages and drawbacks are listed here:

- Dynamic programming is a powerful numerical method for solving optimal control problems of non-linear, time-variant, partially constrained final-state discrete-time approximations of continuous dynamic models with fixed final times and time-variant constraints in the control and the state variables [192], [193].
- The solution is guaranteed to be optimal, regardless of the type of problem [45].

[18] The word "optimal" is used as the lowest achievable value under consideration of a predefined discretisation grid and its numerical errors.

[19] Also called enumerative approach [16]

- Since it is a non-causal optimisation method, all inputs (e.g., a driving cycle) have to be known in advance [45].
- Special attention needs to be paid to limiting the computational effort [45], [54], [192], [193].

3.2.2. Principle of Optimality

Dynamic programming utilises a discrete-time dynamic system $\mathbf{x}_{k+1}$ as stated in Eq. (3.80) with its state vector $\mathbf{x}_k$, which reads

$$\mathbf{x}_k = [x_{0,k}, x_{1,k}, ..., x_{n,k}]^T, \tag{3.82}$$

and its control vector $\mathbf{u}_k$, which reads

$$\mathbf{u}_k = [u_{0,k}, u_{1,k}, ..., u_{m,k}]^T, \tag{3.83}$$

with $k = 0, 1, ..., N-1$. The state vector is constrained by an n-dimensional state space $\mathbb{X}_k \subseteq \mathbb{R}^n$, and the control vector is constrained by an m-dimensional control space $\mathbb{U}_k \subseteq \mathbb{R}^m$. Moreover, both the initial state $\mathbf{x}_0$ as well as the terminal state $\mathbf{x}_{k=N} = \mathbf{x}_N$ are given, and it is valid that $\mathbf{x}_N \in \mathbb{X}_N \subseteq \mathbb{R}^n$. The parameter N defines the number of stages of the remaining optimisation problem. In order to proceed from a state vector $\mathbf{x}_k$ to the terminal state vector $\mathbf{x}_N$, the control vector sequence $(\mathbf{u}_k, \mathbf{u}_{k+1}, ..., \mathbf{u}_{N-1})$, or more precisely the policy $\boldsymbol{\pi} = (\boldsymbol{\mu}_k, \boldsymbol{\mu}_{k+1}, ..., \boldsymbol{\mu}_{N-1})$, has to be applied. The term $\boldsymbol{\mu}_k$ is a function vector, which transforms $\mathbf{x}_k$ to $\mathbf{x}_{k+1}$, cf. [18]

$$\mathbf{x}_{k+1} = \mathbf{f}_k\Big(\mathbf{x}_k, \boldsymbol{\mu}_k(\mathbf{x}_k)\Big), \qquad \mathbf{u}_k = \boldsymbol{\mu}_k(\mathbf{x}_k). \tag{3.84}$$

Each policy causes an instantaneous cost-to-go function sequence $(I_k, I_{k+1}, ..., I_{N-1})$. It is assumed that the instantaneous cost-to-go function I_k for each stage k to the next stage $k+1$ only depends on the current control vector $\mathbf{u}_k$, the previous and adjacent state vectors $\mathbf{x}_k$ and $\mathbf{x}_{k+1}$, respectively. Moreover, I_k also considers the state space constraints with a penalty function $\phi(\mathbf{x}_k)$.

The instantaneous cost-to-go function I_k can be written using the discrete-time model in Eq. (3.80) as

$$I_k = \tilde{h}_k(\mathbf{x}_k, \mathbf{x}_{k+1}, \mathbf{u}_k) + \phi_k(\mathbf{x}_k) = h_k(\mathbf{x}_k, \mathbf{u}_k) + \phi_k(\mathbf{x}_k), \tag{3.85}$$

where $k = 0, 1, ..., N-1$. Each policy results in a cost functional value J_k, which can be written as:

$$J_k = I_k + I_{k+1} + ... + I_{N-1}. \tag{3.86}$$

At this point, it is important to highlight the difference between I_k and J_k. The instantaneous cost-to-go I_k is the cost of processing from an arbitrary stage k to its next stage $k+1$. However, the cost functional J_k characterises the cumulative cost of the

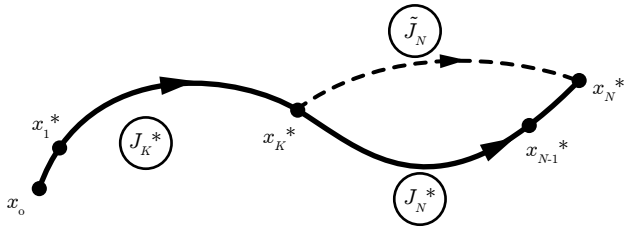

Figure 3.20.: Schematic representation of the *Principle of Optimality*

The solid line shows the optimal state vector sequence $(\mathbf{x}_0^*, \mathbf{x}_1^*, ..., \mathbf{x}_{N-1}^*, \mathbf{x}_N^*)$ with the corresponding optimal policy π^*. Selecting an optimal state $\mathbf{x}_k^*$ divides the optimal trajectory and the optimal control sequence into two parts. Assuming that the cost functional $\tilde{J}_N < J_N^*$, the remainder of the cost functional J_N^* is then not part of the optimal solution, which is in conflict with the preliminary statement.

initial stage k to the terminal stage $k = N$. By using the relation stated in Eq. (3.84), Eq. (3.86) can be reformulated to

$$J_k = J_k(\mathbf{x}_k; \mathbf{u}_k, \mathbf{u}_{k+1}, ..., \mathbf{u}_{N-1}) = J_{\boldsymbol{\pi}}(\mathbf{x}_k). \tag{3.87}$$

Equation (3.87) highlights that the cost functional J_k for a given policy $\boldsymbol{\pi}$ only depends on the policy $\boldsymbol{\pi}$ itself and the initial state vector $\mathbf{x}_k$. Consequently, the optimal control policy $\boldsymbol{\pi}^* = (\boldsymbol{\mu}_k^*, \boldsymbol{\mu}_{k+1}^*, ..., \boldsymbol{\mu}_{N-1}^*)$ is evaluated by minimising the cost functional J_k

$$\min_{\boldsymbol{\pi} \in \boldsymbol{\Pi}} J_k(\mathbf{x}_k; \boldsymbol{\mu}_k^*, \boldsymbol{\mu}_{k+1}^*, ..., \boldsymbol{\mu}_{N-1}^*) = J_{\boldsymbol{\pi}}^*(\mathbf{x}_k). \tag{3.88}$$

The set of all admissible policies is denoted by $\boldsymbol{\Pi}$. The relation in Eq. (3.88) is used to explain the *Principle of Optimality* (see also Figure 3.20).

Bellman [18] formulated the *Principle of Optimality* as follows:

> "An optimal policy has the property that whatever the initial state and initial decision are, the remaining decisions must constitute an optimal policy with regard to the state resulting from the first decision."

3.2.3. Mathematical Formulation - Bellman Equation

Based on the *Principle of Optimality*, a successive mathematical formulation, the so-called *Bellman equation*[20], is derived.

The control sequence $(\mathbf{u}_k, \mathbf{u}_{k+1}, ..., \mathbf{u}_{N-1})$ is given, starting from an arbitrary stage k. The control sequence $(\mathbf{u}_{k+1}, \mathbf{u}_{k+2}, ..., \mathbf{u}_{N-1})$ is then the remainder of the given policy $\boldsymbol{\pi}$.

[20] Also called functional equation

According to Eq. (3.86) and Eq. (3.87), the cost functional J_k can be rewritten as

$$\begin{aligned} &\min_{\mathbf{u}_k, \mathbf{u}_{k+1}, ..., \mathbf{u}_{N-1}} J_k(\mathbf{x}_k; \mathbf{u}_k, \mathbf{u}_{k+1}, ..., \mathbf{u}_{N-1}) = \\ &= \min_{\mathbf{u}_k, \mathbf{u}_{k+1}, ..., \mathbf{u}_{N-1}} \left[I_k(\mathbf{x}_k, \mathbf{u}_k) + J_{k+1}(\mathbf{x}_{k+1}; \mathbf{u}_{k+1}, \mathbf{u}_{k+2}, ..., \mathbf{u}_{N-1}) \right] \end{aligned} \tag{3.89}$$

Determining the optimal policy $\boldsymbol{\pi}^*$ using the *Principle of Optimality* and the mathematical relation in Eq. (3.88) leads to

$$J_k^*(\mathbf{x}_k) = \min_{\mathbf{u}_k} \left[I_k(\mathbf{x}_k, \mathbf{u}_k) + J_{k+1}^*(\mathbf{x}_{k+1}) \right]. \tag{3.90}$$

Together with Eq. (3.80), Eq. (3.90) describes the *Bellman equation*. Dynamic programming evaluates the optimal cost functional $J_k^*(\mathbf{x}_k)$ at every stage k by using the basic recurrence relation in Eq. (3.90). The optimal policy is then calculated backward in time. Using the notation introduced in [193], the cost-to-go for the state vector $\mathbf{x}_k$ in the discretized state space at the node with time-index $k = N$ and state-index i reads

$$J_N(\mathbf{x}^i) = g_N(\mathbf{x}^i) + \phi_N(\mathbf{x}^i). \tag{3.91}$$

The remainder cost functionals at $k = N-1, N-2, ..., 1, 0$ are

$$J_k(\mathbf{x}^i) = \min_{\mathbf{u}_k} \left\{ h_k(\mathbf{x}^i, \mathbf{u}_k) + \phi_k(\mathbf{x}^i) + J_{k+1}\Big(\mathbf{f}_k(\mathbf{x}^i, \mathbf{u}_k)\Big) \right\}. \tag{3.92}$$

For clarity, the index k of the state vector $\mathbf{x}_k$ is omitted in Eq. (3.91) and Eq. (3.92) and in Figure 3.21. Thus, the term $\mathbf{x}^i$ denotes the state vector $\mathbf{x}$ in the discretized state-time space $\mathbb{X}_k$ at the node with time-index k and state-index i (see Figure 3.21). The term J_{k+1} in Eq. (3.92) is evaluated only at discretized points in the state space. Moreover, the output of the model function $\mathbf{f}_k(\mathbf{x}^i, \mathbf{u}_k)$ is a vector with continuous values in the state space, which may be between the nodes of the state space grid. A method to determine an approximation of J_{k+1} in Eq. (3.92) is explained in the following chapter. To sum up, in the conventional formulation, the entire multi-stage decision process is considered as essentially one stage, at the cost of vastly increasing the dimension of the problem [17]. Replacing the enumerative approach with the problem of solving a system of recurrence relations involving functions of much smaller dimensions, as in Eq. (3.90), will yield computational advantages and preserve the single-stage characteristic of the problem [16], see also Chapter 3.2.5.

3.2.4. Approximation in the Cost Functional and Policy Space

In the implemented DP algorithm adopted from [193], the cost functional J_{k+1} in Bellman's equation (3.90) is only solved for discrete state space grid points. Nevertheless, the output of the model function $\mathbf{f}_k(\mathbf{x}^i, \mathbf{u}_k)$ is continuous in the state space and, in general, between the discrete state space grid. Consequently, a proper method has to be selected in order to evaluate an accurate cost-to-go function J_{k+1} at each state space grid point

$\mathbf{x}^i$. In [16], this process is called *successive approximation*. The algorithm adopted from [191], [193] applies linear interpolation to determine a proper value of the cost functional J_{k+1}. Besides the interpolation within the feasible state, special attention is paid to the interpolation performance near the state space constraints defining the lower and upper boundaries of the feasible area. In this thesis, the *boundary-line method* introduced by [191] is used.

The basic interpolation near the boundaries results in numerical errors caused by the discretisation. Since infeasible states have a very high or even infinite cost, these points are not considered for the solution. The numerical problem arises when the DP algorithm evaluates the cost-to-go between feasible and infeasible state grid points. Due to the interpolation, the boundary of the feasible state space is blurred [192]. This leads to inaccurate results, especially near the boundary. The boundary-line method of [191], [193] can only handle one state variable. Thus, the general problem formulation in Eq. (3.80) is reformulated to

$$x_{k+1} = f_k(x_k, u_k) = \tilde{f}_k(x_k, u_k) + x_k. \tag{3.93}$$

The boundary-line method eliminates these numerical problems for one-dimensional dynamic systems, see Eq. (3.93), by determining the lower and upper boundary-lines first. The lower boundary-line is defined as the lowest state $x_{k,lo}$ at each stage k, which results in the predefined terminal state x_N. Consequently, the lower boundary-line can be determined starting from the final state at stage $k = N-1$ and processing to stage $k = 0$. An optimisation problem DOP_k is solved at each decision stage $k = N-1, ..., 1$ in order to calculate the boundary-line backward in time:

$$\begin{aligned}
&\min_{x_{k,lo}, u_k} x_{k,lo}, && (3.94)\\
&\tilde{f}_k(x_{k,lo}, u_k) + x_{k,lo} = x_{k+1,lo}, && (3.95)\\
(\mathrm{DOP}_k) \qquad &u_k \in \mathbb{U} \subset \mathbb{R}, && (3.96)\\
&x_{k,lo} \in \mathbb{X} \subset \mathbb{R}, && (3.97)\\
&x_{N,lo} = x_N, && (3.98)
\end{aligned}$$

where x_{k+1} is the set of optimal solutions of the problem DOP_{k+1}. Equations (3.94) and (3.95) result in an optimisation problem with constraints as stated in Eq. (3.95) through Eq. (3.98). It reads

$$\max_{x_{k,lo}, u_k} \tilde{f}_k(x_{k,lo}, u_k). \tag{3.99}$$

The upper boundary-line $x_{k,up}$ is evaluated similarly. Next to the state values $x_{k,lo}$ and $x_{k,up}$ of the boundary-lines, the cost-to-go values $J_{k,lo}$ and $J_{k,up}$ are stored at each stage k. The boundary-lines can now be used in order to improve the interpolation performance. Near the boundary, interpolation between the finite cost-to-go $J_{k,lo}$, $J_{k,up}$ and a grid point inside the feasible state space is possible, cf. Figure 3.21. According to [192], the set of reachable states of the model function $f_k(x^i, u_k)$ at stage k from a

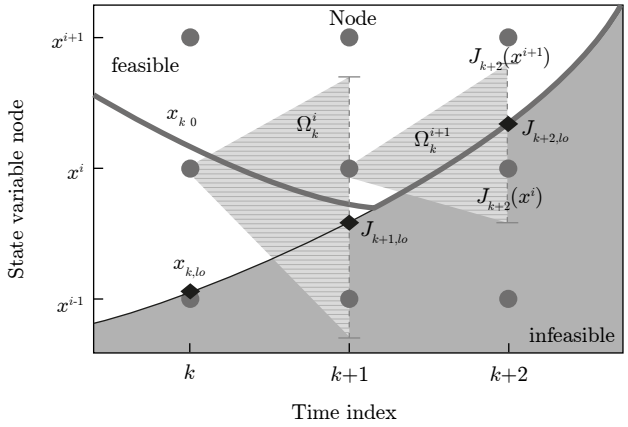

Figure 3.21.: Boundary-line method [191]

This approach improves the interpolation performance near the boundaries. Instead of interpolating between a feasible and an infeasible cost functional, the method pre-calculates the costs directly on the boundary-line. For instance, the cost-to-go for $J_{k+1}(x^i)$ is infinite using the basic DP algorithm, due to an interpolation of a feasible cost-to-go $J_{k+2}(x^{i+1})$ and infeasible $J_{k+2}(x^i)$. The boundary-line method pre-calculates the lower and upper boundary-lines, resulting in an interpolation of two feasible cost-to-go values $J_{k+2}(x^{i+1})$ and $J_{k+2,lo}$. Thus, the cost-to-go $J_{k+1}(x^i)$ is finite. This prevents the intrusion of the infeasible area into the feasible one.

given discrete state variable node x^i is denoted by Ω_k^i. When calculating the cost-to-go at stage $k+1$ and node x^i using the recurrence relation (3.92), $J_{k+1}(x^i)$ becomes infinite if the basic DP algorithm is used, due to the linear interpolation between a finite $J_{k+2}(x^{i+1})$ and an infinite cost functional $J_{k+2}(x^i)$. Consequently, the costs $J_{k+1}(x^i)$ also become infinite, although the grid point is in a feasible area. This numerical error propagates, and the infeasible region grows into the actual feasible one [192]. In contrast, the boundary-line method deployed here utilises the pre-calculated cost-to-go $J_{k+2,lo}$ instead of the infeasible cost $J_{k+2}(x^i)$ for interpolation purposes. Therefore, the state variable node x^i at stage $k+1$ is feasible. This results in an improved accuracy near the boundary and avoids blurring the feasible state space. The restriction to a one-dimensional state variable x is not a limitation for the present thesis, due to the fact that a one-dimensional dynamic model is used, see Chapters 3.1 and 3.2.5. In [45], the idea of avoiding numerical errors near the boundaries is extended to an arbitrary number of state and control variables.

The algorithm first evaluates the lower and upper boundary-lines, and then applies backward in time Eq. (3.90). The output is a map of control signals and the corresponding cost functional J_k at each feasible node x^i, for each stage k. During a subsequent forward calculation, this map is used to find the optimal control sequence u_k^* using the dynamic model in Eq. (3.80). Since the control space $\mathbb{U}_k$ is also discrete and only given for nodes of the discrete state space, the optimal control signal has to be interpolated,

if the actual state does not match with the points in the state space grid. According to [16] and [18], this procedure is called *approximation in policy space*. According to [191], the application of the boundary-line method concurrently improves the performance of the forward simulation, since the interpolation of the control signals is then carried out between feasible grid points and grid points determined on the boundary-line.

3.2.5. Assessing Computational Effort

Computation time is a major issue of DP. In general, the discrete n-dimensional state space $\mathbb{X}_k \in \mathbb{R}^n$ has at each stage k a predefined number of grid points N_{x_i} in each dimension, where $i = 1, 2, ..., n$. The total number of all state space grid points at stage k is then

$$N^{\mathbf{x}} = \prod_{i=1}^{n} N_{x_i}. \tag{3.100}$$

The discretisation of the m-dimensional control space $\mathbb{U}_k \in \mathbb{R}^m$ results in a total number of all control policy space grid points at stage k

$$N^{\mathbf{u}} = \prod_{j=1}^{m} N_{u_j}, \tag{3.101}$$

where N_{u_j} is the number of grid points at stage k in each dimension of the m-dimensional control vector, with $j = 1, 2, ..., m$. Consequently, the estimated computational effort of the backward calculation T_{DP} for all N stages is

$$T_{DP} \approx N \cdot N^{\mathbf{x}} \cdot N^{\mathbf{u}} \cdot \tau. \tag{3.102}$$

where τ is the average time of a single step of calculation. The algorithm used with boundary-line method [192], [193] evaluates a one-dimensional control system with the same number of grid points at each stage k; therefore, Eq. (3.102) is reduced to

$$T_{DP}^{(1)} \approx N \cdot N_x \cdot N_u \cdot \tau. \tag{3.103}$$

where $T_{DP}^{(1)}$ is the total computing time of the backward calculation for a one-dimensional control system.

Considering the boundary-line method introduced in [191], [192], the total computational effort $T_{DP,line}^{(1)}$ of the one-dimensional control system using the boundary-line method is estimated by

$$T_{DP,line}^{(1)} \approx T_{DP}^{(1)} - T_{\infty} + T_{BL}, \tag{3.104}$$

where $T_{DP}^{(1)}$ is the total computational time of the one-dimensional control system of the basic DP algorithm, T_{∞} is the computational effort for calculations within the infeasible area, and T_{BL} is the calculation time of the boundary-line method. Therefore, $T_{DP}^{(1)}$ is

enlarged by T_{BL}. Since the infeasible domain is well known, the computation time T_∞ for grid points in this infeasible domain can be omitted [12]. According to [191], the overall computational time for DP with the boundary-line method $T^{(1)}_{DP,line}$ is less than it is when using the basic algorithm $T^{(1)}_{DP}$, and the accuracy of the solution increases as well.

Equations (3.100) through (3.102) highlight the main factors that influence the computational effort. The dimension of the state vector[21] n and the dimension of the control vector m have the strongest effect on the computing time. This influence is also known as the *curse of dimensionality* [17]. Increasing the number of state or control variables increases the computing effort at an exponential rate [16]. Furthermore, the number of decision stages N linearly affects the performance of the algorithm.

Another important performance measure is the memory demand of the optimisation algorithm. According to Bellman's equation, at each stage $k = 0, 1, ..., N-1$ the optimal control policy $\mathbf{u}_k$ has to be determined for all state grid points $N^{\mathbf{x}}$. Moreover, at each state grid point, an m-dimensional control vector is applied, resulting in a long-term memory demand M_1

$$M_1 = N \cdot N^{\mathbf{x}} \cdot m. \tag{3.105}$$

Furthermore, the algorithm needs to save the current cost functional J^*_k and its predecessor value J^*_{k+1} for the entire discretised state space. Consequently, the required short-term memory M_2 is

$$M_2 = 2 \cdot N^{\mathbf{x}}. \tag{3.106}$$

Considering Eq. (3.100) together with Eq. (3.106) points out that the dimension of the state vector n has a significant influence on the memory allocation.

3.2.6. Relevant Application Aspects

The dimensions of the state vector $\mathbf{x}_k$ and the control signal $\mathbf{u}_k$ are crucial for the performance of DP. Consequently, the optimisation model used in this thesis is limited to a one-dimensional state vector x_k and a single control signal u_k. The following chapter describes this one-dimensional optimisation problem.

3.2.6.1. Selection of a Cost Functional

Chapter 3.2.1 described the criterion functions from a rather general point of view. This chapter introduces cost functionals that are applied in automotive research.

$$J_k(x_k) = g_N(x_N) + \sum_{k=0}^{N-1} m_{k,f}(x_k, u_k), \tag{3.107}$$

[21] Also called order or system dimension [54]

where $m_{k,f}$ represents the instantaneous fuel consumption at each time step k, and $g_N(x_N)$ is the final instantaneous cost-to-go of the terminal state x_N at time step $k = N$. This approach is used in the present thesis. In the literature, however, Eq. (3.107) is often modified in order to include other optimisation criteria. In [190], the basic cost functional in Eq. (3.107) is extended with the ICE state on/off, whereby [61] proposed a cost-to-go function incorporating fossil fuel consumption and pollutant emissions. Basic drivability aspects, such as the number of shifting events and engine events, are investigated in [152]. In [204], a sophisticated cost functional including fuel consumption, vehicle performance and drivability aspects is introduced. The costs of grid electricity are considered in the criterion function of [137]. A general formulation of a cost functional is given in Eq. (3.108)

$$J_k(\mathbf{x}_k) = g_N(\mathbf{x}_k) + \sum_{k=0}^{N-1} \left(\sum_{\xi=1}^{\Xi} w_\xi \cdot h_{k,\xi}(\mathbf{x}_k, \mathbf{u}_k) \right), \tag{3.108}$$

where $\xi = 1, ..., \Xi$ is the number of cost criteria, w_ξ is the weighting factor of the single cost criterion $h_{k,\xi}$. It is obvious that the sum of the weighting factors $\sum w_\xi = 1$. The weighting factors have a substantial influence on the cost functional J_k [137]. Moreover, these weighting factors may be different for changing boundary conditions, such as the length of the route. Furthermore, introducing a weighted cost functional often increases the dimension of the state variable [152], [190]. For this reason, the present thesis uses only the basic formulation of the cost functional in Eq. (3.107).

3.2.6.2. Determination of the Discretisation Grid Resolution

For real-time applications, the number of state and control grid points is a critical aspect, but the total number of decision stages N also has to be chosen properly. In order to implement DP in automotive applications, an adequate trade-off between accuracy and computing time has to be found. Figure 3.22 shows a representation of the discretisation grid and accuracy. To guarantee fast computation, the grid resolution is low, but still in the area where the fuel consumption does not change significantly [80]. In this thesis, a discretisation of the one-dimensional state variable x_k, which represents the SOC of the battery, and the single control variable u_k, which represents the power distribution factor u_d, are both set to 64. This grid provides sufficient accuracy and speeds up the optimisation process [115]. Furthermore, the number of decision stages N is defined by the sample time Δt_s of the backward vehicle model and the total length of the predicted driving cycle.

3.2.6.3. Enhancing Vehicle Model Performance

Besides considering the computational effort, a proper evaluation of the quasi-static vehicle model can further improve the total computing time. First, given a known driving

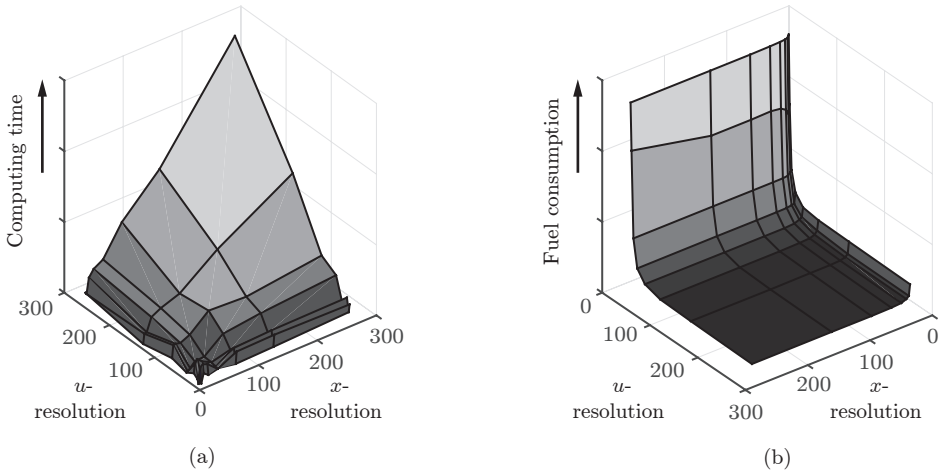

Figure 3.22.: Analysis of the discretisation grid, computing time and the fuel consumption change

The trade-off between accuracy and number of discretisation grid points: The number of discrete nodes N_x and N_u in the state space $\mathbb{X}$ and the control space $\mathbb{U}$, respectively, are chosen to be in an area where the fuel consumption does not change significantly. This guarantees adequate accuracy and low computing time.

cycle[22], and thus a known gear selection, the variables torque $T_{GBX,in}$ and angular speed $\omega_{GBX,in}$ of the gearbox are calculated in advance. Since the scalar control variable only influences the torque distribution u_d of the EMG and the ICE before the gearbox, this pre-calculation is valid. The MATLAB [129] simulation environment used can perform calculations of matrices once at the beginning of the optimisation process, instead of doing vector analysis at each stage k.

Moreover, the pre-calculation allows a reduction in the dimension of the characteristic maps of all components. Because the driving cycle is given, the rotational speeds ω of all drivetrain components are known[23]. Consequently, all two-dimensional maps in the rotational speed ω_i and torque T_i can be reduced to one-dimensional maps in the torque T_i only. The aforementioned actions improve the computing time of the entire optimisation process. More detailed information about the performance improvement is provided in [80].

3.2.6.4. Overall Applied Controller Structure

This thesis investigates two different model-based control structures. The first controller structure is called the *one-level dynamic programming approach*, and the second one is called the *two-level dynamic programming approach*.

[22]The driving cycle is not exactly known, but is predicted.
[23]Starting manoeuvres with clutch slip are covered differently.

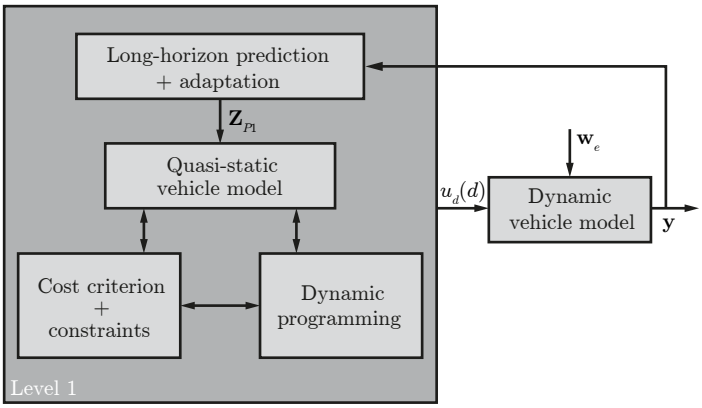

Figure 3.23.: Schematic representation of the *one-level dynamic programming approach*

The closed-loop controller only uses long-horizon prediction and adaptation at low update frequencies. While driving, certain vehicle states $\mathbf{y}$ are gathered and processed by the long-horizon prediction and adaptation algorithm. The predicted input matrix $\mathbf{Z}_{P1}$ consists of the predicted velocity, acceleration and inclination profile. With the help of dynamic programming that includes cost criterion and system constraints, the optimal power distribution $u_d(t)$ is determined. The power distribution is transformed to the spatial domain $u_d(d)$ and is used as input for the dynamic vehicle model. Moreover, external disturbances $\mathbf{w}_e$ act on the vehicle.

One-level dynamic programming approach

Figure 3.23 shows the structure of this approach. Taking into account the predefined system constraints, the cost functional in Eq. (3.107) and the quasi-static vehicle model, DP determines the optimal torque distribution sequence $\left(u_d^*(d)\right) = \left(u_d^*(d_k), ..., u_d^*(d_N)\right)$ of the predicted driving cycle. This distribution sequence is originally evaluated in the time domain $\left(u_d^*(t)\right)$, but is then transformed to the spatial domain $\left(u_d^*(d)\right)$. This transformation accounts for discrepancies in the estimated and actual speed profiles. Chapter 3.3 provides detailed information on the prediction algorithm and its transformation.

The predicted input matrix $\mathbf{Z}_{P1}$, which accounts for the future driving states, reads

$$\mathbf{Z}_{P1} = \begin{bmatrix} \mathbf{v} \\ \mathbf{a} \\ \boldsymbol{\beta} \end{bmatrix}_{P1}, \tag{3.109}$$

where $\mathbf{v}_{P1} = [v_k, v_{k+1}, ..., v_N]$ is the predicted vehicle speed vector, $\mathbf{a}_{P1} = [a_k, a_{k+1}, ..., a_N]$ is the corresponding vehicle acceleration vector, and $\boldsymbol{\beta}_{P1} = [\beta_k, \beta_{k+1}, ..., \beta_N]$ is a vector containing the inclination of the remaining route. The input matrix $\mathbf{Z}_{P1}$ is frequently updated at either fixed time periods Δt_{U1} or at a certain deviation of the predicted and the actual SOC. The torque distribution sequence $\left(u_d^*(s)\right)$ is the input of the dynamic vehicle model. This dynamic vehicle model is affected by external disturbances $\mathbf{w}_e$, such

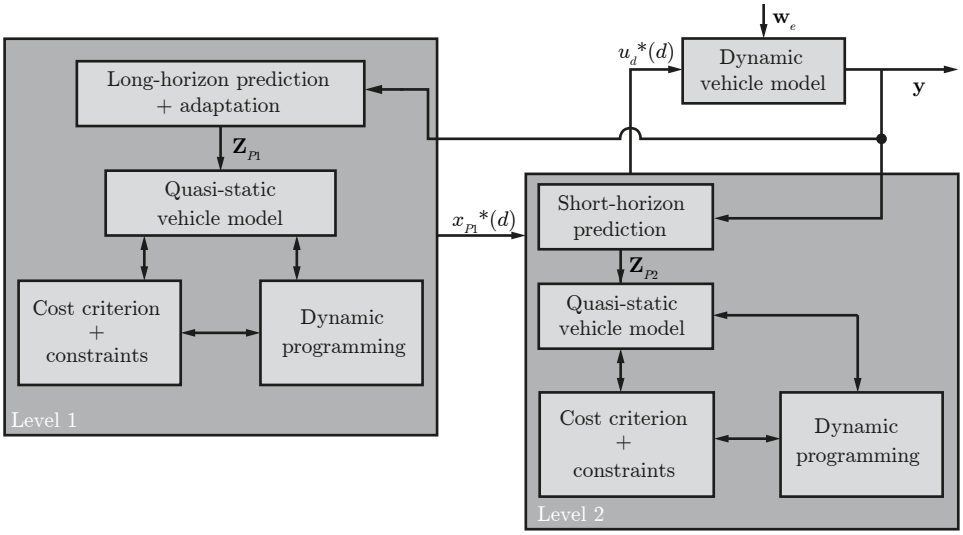

Figure 3.24.: Schematic representation of the *two-level dynamic programming approach*

This approach combines long-horizon and short-horizon prediction in order to improve fuel efficiency. In contrast to the short-horizon prediction, the long-horizon prediction is updated less frequently. The short-horizon prediction uses vehicle states $\mathbf{y}$ to generate the predicted input matrix $\mathbf{Z}_{P2}$ for the quasi-static vehicle model. Together with a spatial domain transformation, dynamic programming determines the optimal power distribution $u_d^*(d)$. The vehicle model interacts with external disturbances $\mathbf{w}_e$.

as wind, road or traffic [75]. Other system outputs are summarised in $\mathbf{y}$. The block *long-horizon prediction and adaptation* is a main part of this thesis and is explained in detail later in this chapter.

Two-level dynamic programming approach

The *two-level dynamic programming approach* uses two different prediction horizons. The first level has the same structure as the controller proposed above. However, the output is the state variable sequence $\left(x_{P1}^*(d)\right)$ instead of the control sequence $\left(u_d^*(d)\right)$. The output of the level-one optimal controller sets the boundary conditions for the *short-horizon prediction*. The prediction horizon is limited to the range of on-board environmental recognition sensors [56], but the prediction is much more accurate due to the prompt occurrence. Consequently, the predicted input matrix of the short-term prediction $\mathbf{Z}_{P2}$ is more detailed than $\mathbf{Z}_{P1}$. It holds that

$$\mathbf{Z}_{P2} = \begin{bmatrix} \mathbf{v} \\ \mathbf{a} \\ \boldsymbol{\beta} \end{bmatrix}_{P2}, \tag{3.110}$$

which at first glance looks the same as Eq. (3.109), but the time aspect and the degree of detail are different. While the level-one prediction accounts for the entire driving route, the level-two controller only accounts for the range of about 250 m [56], [207] and determines the control sequence $\left(u_d^*(t)\right)$. This control sequence is transformed to the spatial domain $\left(u_d^*(d)\right)$ and provides input for the dynamic vehicle model. The *short-horizon prediction* is a closed-loop control with short update intervals Δt_{U2}, in contrast to the *one-level dynamic programming approach*, for which the update interval is limited by the computing time of the entire remaining driving route. Consequently, the short-horizon prediction performs better if disturbances $\mathbf{w}_e$ occur.

The discrete-time model part of the long-horizon prediction and adaptation is ultimately depicted as

$$x_{k+1} = f(x_k, u_k, \mathbf{Z}_{P1}). \tag{3.111}$$

In contrast, the short-horizon prediction discrete-time model is

$$x_{k+1} = f\left(x_k, u_k, \mathbf{Z}_{P2}\right). \tag{3.112}$$

To conclude, the *one-level DP approach* uses the entire driving route in order evaluate the power distribution sequence (u_d). In contrast, the *two-level DP approach* determines the SOC trace over the entire driving cycle first, similar to the one-level DP approach. This SOC trace is then used as a boundary for the short-time optimisation, which determines the power distribution sequence (u_d) for a given prediction horizon, such as within the environmental recognition sensor range of about 250 m. The two methods differ significantly in terms of accuracy and computational effort.

3.3. Prediction and Adaptation Approach

The innovative holistic energy management controller proposed in Chapter 3.2 requires the upcoming speed profile a-priori. However, the assumption of a known future speed profile is not realistic. Consequently, the speed profile has to be predicted. It is obvious that a speed prediction cannot be determined exactly, since it strongly depends on the individual driving style and other road users. Figure 3.25 shows the complex interaction of the driver, vehicle and environment.

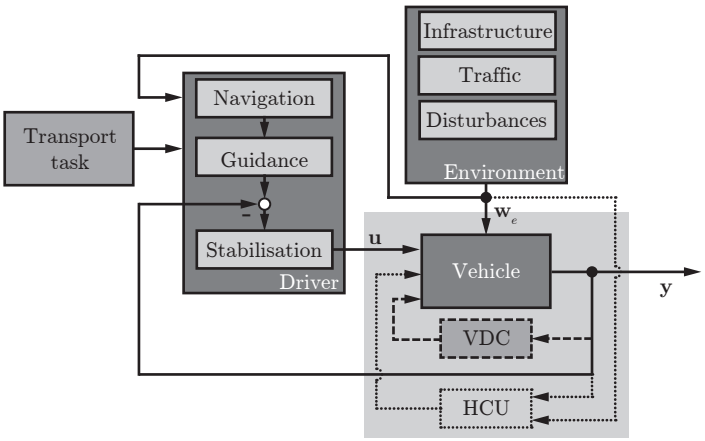

Figure 3.25.: Interaction of driver, vehicle and environment, adapted from [21]

The complex interactions of driver, vehicle and environment hamper prediction of the upcoming power demand. Drivers operate at three different levels in order to accomplish a transportation task – navigation, guidance and stabilisation. They guide their vehicles using the vehicle control inputs $\mathbf{u}$. The vehicle reacts to the driver inputs, but also to the ambient environment $\mathbf{w}_e$, such as infrastructure, traffic and other disturbances. Vehicle states $\mathbf{y}$ are used by different control units (VDC, HCU, ...) and by the driver. The former represent the inner closed loop, and the latter comprise the outer closed loop.

The driver acts on three different levels (cf. Chapter 3.1.2.9) – navigation, guidance and stabilisation – in order to fulfil the desired transportation task. External disturbances $\mathbf{w}_e$, such as infrastructure, traffic or other disturbances, influence both the vehicle and the driver. The vehicle states $\mathbf{y}$ are used by different control units, such as the vehicle dynamics controllers (VDCs) or the hybrid control unit (HCU). They comprise the inner closed loop of the driver-vehicle-environment system. The driver perceives the environmental influences and the vehicle's behaviour and reacts with specific vehicle control inputs $\mathbf{u}$, such as pedal position, steering-wheel angle or selection of gears. Thus, the driver forms the outer closed loop (cf. Figure 3.25).

This thesis proposes two different levels of speed prediction (cf. Figure 3.26). The short-term prediction covers all distances ahead of the vehicle which are in the range of on-board environmental recognition sensors, while the long-term prediction approximates the speed profile over the entire driving route. Consequently, the two levels differ strongly

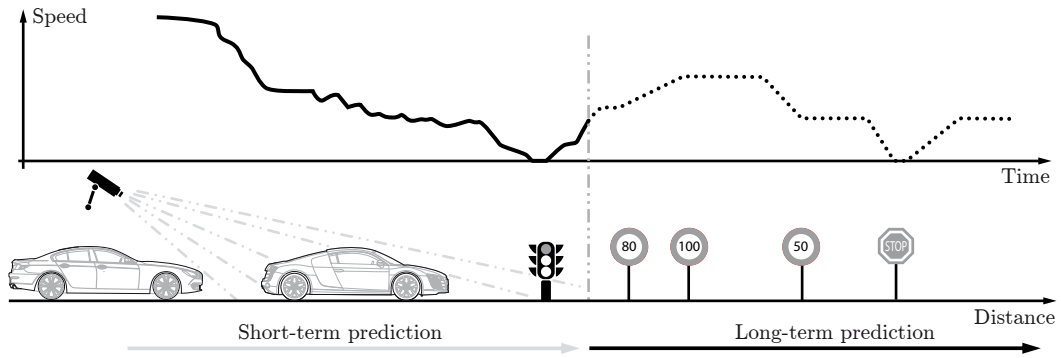

Figure 3.26.: Two levels of speed prediction

The short-term prediction covers all distances ahead of the vehicle which are in the range of on-board environmental recognition sensors. In contrast, the long-term prediction predicts the speed profile over the entire driving route. For this reason, the two prediction levels yield different levels of information detail and processing times.

in terms of information detail and processing time. The present thesis focuses on the long-term prediction, where the information detail is limited. Nevertheless, with the help of fixed-location objects and the driver's individual driving behaviour, a long-term speed prediction is performed. The implemented prediction and adaptation algorithm consists of three main parts, which are described in detail in the remainder of Chapter 3.3.

3.3.1. Fixed-location Information

Drivers adapt their travelling velocity to the current driving environment. However, every road has its fixed characteristics (e.g., speed limits, height profiles and curvatures), and these characteristics are used to estimate an initial rough speed profile without including the driver's individual behaviour (cf. Figure 3.27). In addition, this information is used to perform a better estimation of the remaining driving range considering the current energy content on-board [71]. One basic requirement is knowledge of the vehicle's current position and the upcoming driving route, which can be obtained via digital maps.

Navigation systems in automotive applications

The main objective of a navigation system is to route the driver to the desired destination using information about the current position and digital maps. The evaluation of the current position combines two methods. First, the *dead-reckoning* evaluates a new absolute position depending on the current position, the differences in heading angle, path and the elapsed time, using on-board sensors and, if available, GNSS signal. Next,

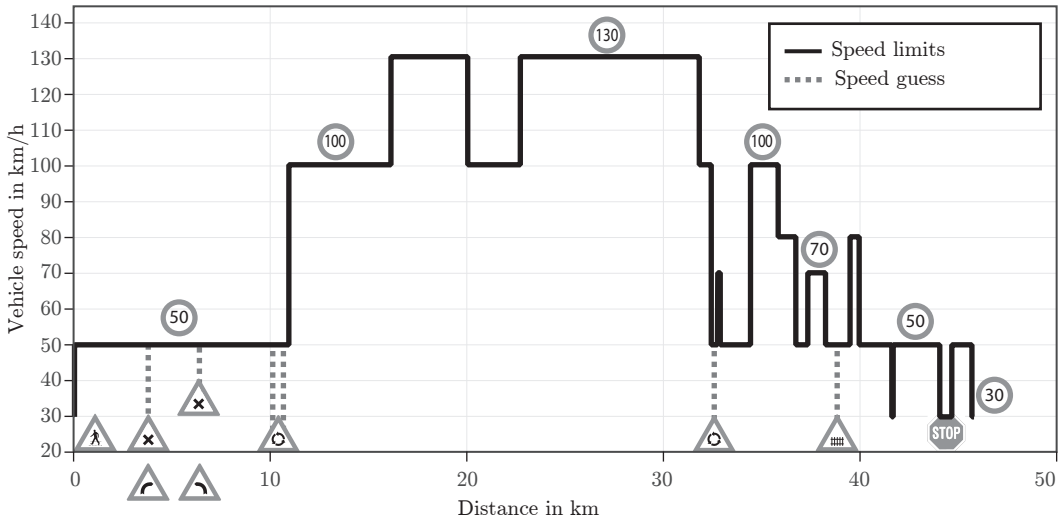

Figure 3.27.: Initial rough speed prediction obtained from the available GNSS signals and digital maps

The solid line represents the definite speed limits of the recorded real-world driving cycle, and the dashed line depicts a selection of additional position-fixed information with its initial speed approximation. The innovative P&A algorithm successively adapts this rough speed profile to the driver's individual driving style.

a *map-matching* algorithm adjusts the absolute position data to the data of digital maps and thus increases accuracy. The determination of the position of on-board navigation systems is done via GNSS (e.g., GPS) and additional on-board sensors. For instance, GPS is based on 31 satellites. If signals from four satellites are available, the position of the receiver can be determined within an accuracy of a few meters [105]. In order to access information from the navigation system, a standardised information exchange interface for advanced driver assistance systems (ADASs), called ADASIS[24] is currently being developed [48].

Legal speed limits

Digital maps provide information about the legal speed limits for the upcoming driving route. The information regarding speed limits is the basis for the implemented innovative P&A algorithm. Figure 3.27 represents the speed limits of the recorded real-world driving cycle, introduced in Chapter 4.1. At first, the transition between consecutive speed limits is volatile. These abrupt speed changes are later replaced by the driver's individual acceleration/deceleration behaviour. At rural roads curvatures, limited visibility and speed limits are the main influences on the travelling speed, while for urban roads, other road users, speed limits and temporary obstacles are the main factors for speed changes [178].

[24] Advanced Driver Assistance Systems Interface Specifications

Upcoming height profile

Modern digital maps also contain information about the height profile of the route ahead. This information is included in the P&A algorithm. Just as the speed limits v_L, the height profile h is available as a function of the position or distance d.

$$v_L = v(d), \tag{3.113}$$

$$h = h(d). \tag{3.114}$$

For simulation purposes, real driving tests were conducted, whereby the actual speed profile, speed limits and the height profile were recorded. Figure 4.2(b) shows the height profile of the recorded simulation driving cycle. The information about the height profile is linked to position points, see also Eq. (3.114), which may contain additional information, such as speed limits v_L or other traffic announcements.

Intersections

Intersections also influence the driver's speed selection. Depending on the type of intersection (e.g., unregulated/regulated, turn left/right or straight on), the average crossing speed varies. For instance, the probability of stopping a vehicle before turning left is higher than that for a right-turn manoeuvre at an unregulated intersection. The different crossing speeds are detected, and this additional information is available for the implemented intelligent P&A algorithm. It is assumed that most drivers adhere to traffic regulations. Consequently, at intersections with a stop sign, the driver stops the vehicle for a certain time t_S. This information is gathered and used for driver-adapted prediction. Predicting the state of traffic lights at intersections over a longer term is a challenging task, since the state may be different when the vehicle arrives there. For this reason, the implemented prediction algorithm does not distinguish between regulated and unregulated intersections. Furthermore, rail-road crossings and roundabouts are covered in a similar way. Using advanced communication technology, such as C2X may improve the prediction accuracy. The term C2X is a hypernym for car-to-car (C2C) and car-to-infrastructure (C2I) communication [105]. However, this technology is beyond the scope of this thesis.

Other traffic events

Besides considering position-fixed information about the height profile and different types of intersections, the algorithm covers many traffic signs, including:

- Overtaking ban
- Pedestrian crossing
- Danger signs (e.g., downhill roads, dangerous curves, roadway narrows)

- Priority roads

The recorded driving cycle does not support any other traffic signs. Information about the curvature of the road κ[25] is another important factor that is included in the innovative algorithm developed here. In general, the algorithm extracts as much position-fixed information as possible. Initially, constant driver-independent (crossing) speeds and acceleration/deceleration are assumed. Later, these areas are gradually replaced by the individual driving behaviour and other dynamic information. Even relying on position-fixed route data alone improves the fuel efficiency of HEVs [12]. However, including the current driving behaviour further improves its potential. The results of the innovative operation strategy in Chapter 4.2.2 emphasise this fact in an impressive manner.

3.3.2. Approximation of the Driving Style and other Dynamic Driving Information

Chapter 3.3.1 proposed a rough speed profile including the speed limits with no speed transitions and a height profile obtained by navigation systems as an initial approximation of the upcoming driving profile. However, this approach does not incorporate the driver's individual driving style and the interaction with other road users. This chapter introduces an adaptation algorithm that is able to add such dynamic information. Historical data about the current trip and data from on-board environmental recognition sensors are used to extract this information.

3.3.2.1. Past Driving Data

The implemented long-term P&A is mainly based on collecting and processing past driving data about the current trip. Figure 3.28 shows the basic principle of the P&A algorithm. While driving, the developed algorithm periodically collects driver/route characteristics and driving situations with the help of a *driving data gathering process*, which samples the longitudinal vehicle speed v_x, accelerator pedal position p_p and the brake pedal position p_b with 1 Hz sampling rate, which is within the main frequency range of longitudinal vehicle dynamics [75]. After a predefined time window Δt_W, relevant data within this moving time horizon are extracted. First, the recorded data is filtered with a zero-phase digital filter[26]. The gathering process determines the average driving speed without standstill $\bar{v}_x$ and the average positive and negative vehicle acceleration $\bar{a}_{x,\pm}$

[25] Information of the curvature is included in digital maps of state-of-the-art navigation systems.
[26] Also called *finite impulse response* (FIR) filter, which processes the input data in both the forward and backward directions

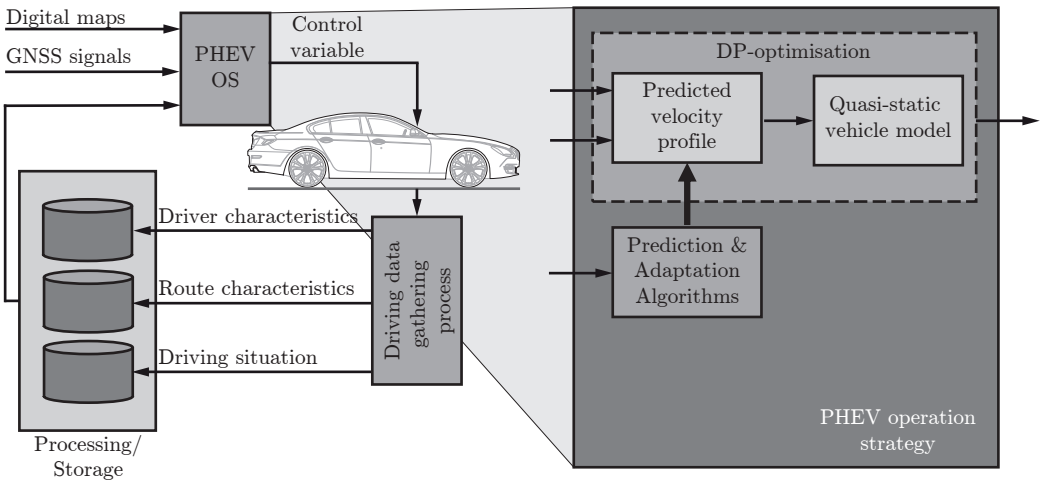

Figure 3.28.: Concept of the prediction and adaptation (P&A) algorithm

During driving, the algorithm gathers information about the driver, route and driving situation in a *driving data gathering process*. Processing and combining this information with position-fixed information, such as digital maps and GNSS signals, enables the innovative operation strategy of PHEVs to further increase the overall fuel saving potential.

within the considered window, see Eq. (3.115) and Eq. (3.116):

$$\bar{v}_x(v_L) = \frac{1}{N_v} \sum_{i=1}^{N_v} v_{x,i}(v_L), \tag{3.115}$$

$$\bar{a}_{x,\pm}(v_{x,0}) = \frac{1}{N_a} \sum_{i=1}^{N_a} a_{x,i}(v_{x,0}), \tag{3.116}$$

where the average driving speed $\bar{v}_x$ and the instantaneous vehicle speed $v_{x,i}$ are related to the current speed limit v_L. The average positive and negative vehicle accelerations $\bar{a}_{x,\pm}$ are calculated according to predefined starting speed levels $v_{x,0}$. The parameters N_v and N_a define the number of time steps within a certain speed limit or starting speed level, respectively.

The collected and processed data is linked to the available position-fixed information and is used to predict the future driving states v_P and a_P, which, in a more general form, read:

$$v_P(v_L) = f\Big(\bar{v}_x(v_L)\Big), \tag{3.117}$$

$$a_{P,\pm}(v_{x,0}) = f\Big(\bar{a}_{x,\pm}(v_{x,0})\Big), \tag{3.118}$$

where the predicted vehicle speed v_P is a function of the average vehicle speed of the past driving $\bar{v}_x$. The predicted positive and negative vehicle accelerations $a_{P,\pm}$ depend on the past average acceleration behaviour $\bar{a}_{x,\pm}$. The speed levels are divided in 10 km/h steps. Furthermore, the extracted data is linked to position-fixed events. This makes it possible to determine the average speed for a certain speed limit as stated in Eq. (3.115). Instead of using the speed limits v_L of the route ahead, a driver-adapted speed profile v_P is used. However, there are still volatile speed gradients. The predicted acceleration $a_{P,\pm}$ replaces the speed change at speed limit transitions. The starting point for an acceleration or deceleration manoeuvre at a specific speed limit change depends on the particular driver. Generally, the manoeuvre does not start exactly at the position of the speed limit change. An acceleration process may start before the speed limit changes to a higher level, although deceleration phases do occur later. The P&A process considers an average time Δt_A and Δt_B for such acceleration and deceleration phases, as discussed in Chapter 3.3.3.

If no past speed values are stored for a certain speed limit, the current speed limit is used as an initial speed approximation. Later, a speed correction factor K_v is used to better approximate missing speed values. This factor is evaluated for each speed limit by

$$K_v = \frac{\bar{v}_x(v_L)}{v_L}, \tag{3.119}$$

The same scenario may occur for evaluating the future acceleration behaviour at speed limit transitions $a_{P,\pm}$. In that case, an approach based on the studies in [29] is used to approximate missing acceleration data. The implemented approximation for acceleration manoeuvres reads:

$$a_{P,+}(v_x) = \frac{D_1}{v_x + D_2} - D_3 v_x^2, \tag{3.120}$$

where D_1, D_2, and D_3 are fitting parameters. The first term in Eq. (3.120) accounts for the maximum traction force. The factor D_2 is used to improve the fitting performance. The second term in Eq. (3.120), which includes D_3, considers the air drag. All other driving resistances are omitted. For braking events, a modified approach based on [29] is deployed:

$$a_{P,-}(v_x) = D_4 \cdot (v_x < v_{L0}) + D_5 \cdot (v_x \geq v_{L0}), \tag{3.121}$$

where D_4 and D_5, are fitting parameters and v_{L0} is a predefined longitudinal velocity threshold. Unlike in [29], there are two constant deceleration values, which should approximately account for the increasing deceleration values at lower speeds [178]. This means that a braking manoeuvre from 50 km/h to 30 km/h is significantly greater than a deceleration from 100 km/h to 80 km/h [178]. An analysis of the investigated driving cycle proves that the deceleration increases with lower vehicle speed (cf. Figure E.1 in Appendix E). At the beginning of a trip, both acceleration and deceleration values have to be initialised, which is done with the most recent values saved from the previous trip. Figure 3.29(a-b) provides a schematic representation of both fitting curves.

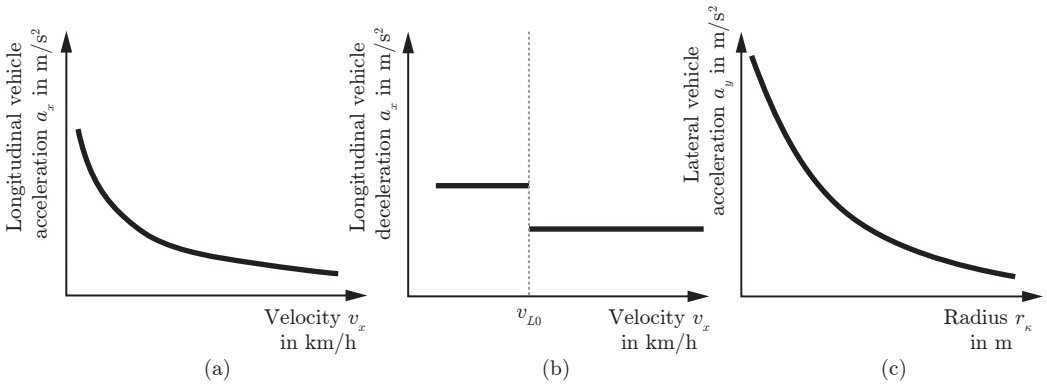

Figure 3.29.: Schematic representation of the acceleration behaviour

Figure (a) depicts the longitudinal acceleration behaviour a_x depending on the longitudinal vehicle speed v_x, while Figure (b) shows the modified approach for estimating the deceleration behaviour based on [29]. A speed threshold v_{L0} is introduced in order to account for different deceleration behaviour at different speeds. Figure (c) shows the lateral acceleration behaviour a_y as a function of the curvature radius r_κ.

When passing fixed-position events (e.g., intersections or railway crossings), the average speed for such an event is stored separately. These average speed values are used later for speed prediction in similar driving route events. The algorithm also adapts the cornering speed to the current driver. According to different scientific studies [29], [178], the cornering speed is another characteristic value for evaluating different driving styles. The procedure is similar to the approximation of the longitudinal acceleration behaviour. When driving through a curve, the longitudinal vehicle velocity v_x is recorded. In addition, digital maps provide the curvature κ of the road segment [113]. The lateral acceleration a_y of the vehicle can be approximated by

$$a_y = \frac{v_x^2}{r_\kappa} = \kappa v_x^2, \tag{3.122}$$

where r_κ is the radius of the current curve. The information about the curvature κ and the selected longitudinal velocity v_x are used to predict the driver behaviour for similar curvatures in the upcoming route[27]. The speed behaviour in curves is predicted based on [178], where a deceleration phase is followed by a constant speed segment, after which there is another accelerating. The *principle of the third sections of a curve*[28] is applied. Thus, the first third of the curve is used to decelerate, the second third is driven at a constant speed, and in the last third the driver accelerates again, see also Figure E.2. The deceleration and acceleration are determined by the method described above, and the constant speed is evaluated by transforming Eq. (3.122).

[27] It is assumed that the driver is not cutting curves. Thus, the curvature of the road is the intended curvature of the driver.

[28] In German: *Prinzip der Drittelspunkte einer Kurve*

3.3.2.2. On-board Environmental Recognition Sensors

On-board environmental recognition sensors are used to account for dynamic influences from the driving environment, which cannot be reliably predicted over the long-term. For example, it is impossible to accurately predict the status of traffic signal lights or traffic congestion. Advanced driver assistance systems rely on different kinds of on-board environmental recognition sensors, see also [21]. *Adaptive cruise control* (ACC) frequently uses radar, laser or camera sensors to evaluate the longitudinal distance and the relative velocity of a vehicle up ahead. Information about whether or not there is a vehicle up ahead can be used to perform a short-term prediction, and if there is a vehicle, to adapt the long-term prediction [119]. For instance, if there is a vehicle ahead which cannot be overtaken, the relative longitudinal velocity decreases steadily, and the probability of a deceleration manoeuvre increases. Besides radar sensors, automotive applications often utilise data from camera systems. This technology is able to classify different traffic objects, such as traffic signs or other road users. However, an accurate distance evaluation is possible [189], but difficult as discussed in [37]. For this reason, car manufacturers combine different data sources to increase reliability and accuracy, an approach which is known as *sensor fusion*. The present thesis assumes that the vehicle features on-board environmental recognition sensors that are able to evaluate objects ahead. Although detailed sensor modelling is not part of this thesis, the sensors enable the short-term prediction to gather information within a certain sensor range. Based on state-of-the-art sensors, the implemented sensor range is up to 250 m [56], [207]. The test vehicle used for the current research was not equipped with any on-board environmental recognition sensors. For this reason, this thesis assumes that the short-term prediction performs ideally within its sensor range. This means that within the sensor range, the speed profile and all additional data is known. Nevertheless, the main contributions of the present research rely on the advanced long-term prediction and adaptation. For comparison reasons, all methods use this limitation concerning the short-term prediction.

3.3.2.3. External Source of Information

Since data stored in digital maps and used for navigation in the automotive industry is static, dynamic influences from the driving environment along the planned route cannot be considered with that technology alone. *Radio data system - Traffic message channel* (RDS-TMC) is used to make additional data available for navigation systems. This data type can be received by broadcasting systems, such as frequency modulation-radio data system (FM-RDS) and digital audio broadcasting (DAB), and by mobile telecommunication systems, such as global system for mobile communication (GSM) and general packet radio service (GPRS). The RDS-TMC message consists of an event and its location [105]. The navigation system may use this information and eventually recalculate the route. Moreover, vehicles can be used as mobile sensors. This technology is called *floating car data* (FCD). By using cellular mobile communication, vehicles are able to detect and send data to a traffic centre network. This method enables the determination of

the traffic speed on the road network. The collected data can be used to identify factors such as traffic congestion [195]. Using additional data (e.g., from sensors transmitted by the vehicle CAN[29]-Bus, such as vehicle acceleration, or information from ADAS), can increase the accuracy of this technology, which is called *extended floating car data* (XFCD) [19]. In the future, other advanced communication methods, such as C2X communication technology, may provide additional information about the infrastructure and other road users. However, since the introduction of this technology is challenging, despite intensive research [105], the present thesis does not consider additional information regarding such external sources.

3.3.3. Time Domain and Spatial Domain Transformation

The data from the navigation system or digital map are based on a certain position, which is given by its *longitude* and *latitude*. A suitable Earth model, such as the *world geodetic system 1984* (WGS84) [87], transforms the geographic coordinates into a plane coordinate system. For each position point, other entities are saved, such as speed limits, curvatures and height position. Nevertheless, the optimisation algorithm described in Chapter 3.2 needs the predicted route information on a time basis. Indeed, although it is possible to design the optimisation algorithm to work in a position-based manner [60], many physical quantities (e.g., the power or energy) are defined on a time basis. The P&A algorithm has to perform a transformation between time and spatial domain, and vice versa. The position-fixed information is applied on the speed limit profile first, and the driver's individual driving behaviour is added later. Both steps are performed in the spatial domain. Assuming the crossing speed at a certain event v_E, cf. Figure 3.30(d), the starting position d_0 and ending position d_e are determined by

$$d_0 = d_{E,1} - \frac{1}{2} a_{E,1} t_{E,1}^2 - v_0 t_{E,1}, \tag{3.123}$$

$$d_e = \frac{1}{2} a_{E,2} t_{E,2}^2 + v_E t_{E,2} + d_{E,2}, \tag{3.124}$$

where $d_{E,1}$ and $d_{E,2}$ are the starting and ending positions of the constant event speed segment, and $a_{E,1}$ and $a_{E,2}$ are the accelerations before and after the event. A constant positive or negative speed gradient a_E is assumed during a certain event. Thus, the time interval during an event $t_{E,1/2}$ reads

$$t_{E,1} = \frac{v_E - v_0}{a_E}, \tag{3.125}$$

$$t_{E,2} = \frac{v_e - v_E}{a_E}, \tag{3.126}$$

where the numerator $v_E - v_0$ represents the speed difference Δv of a deceleration event with the starting speed v_0 and the predicted event speed v_E. In contrast, $v_e - v_E$ is the

[29] Abbreviation for controller area network

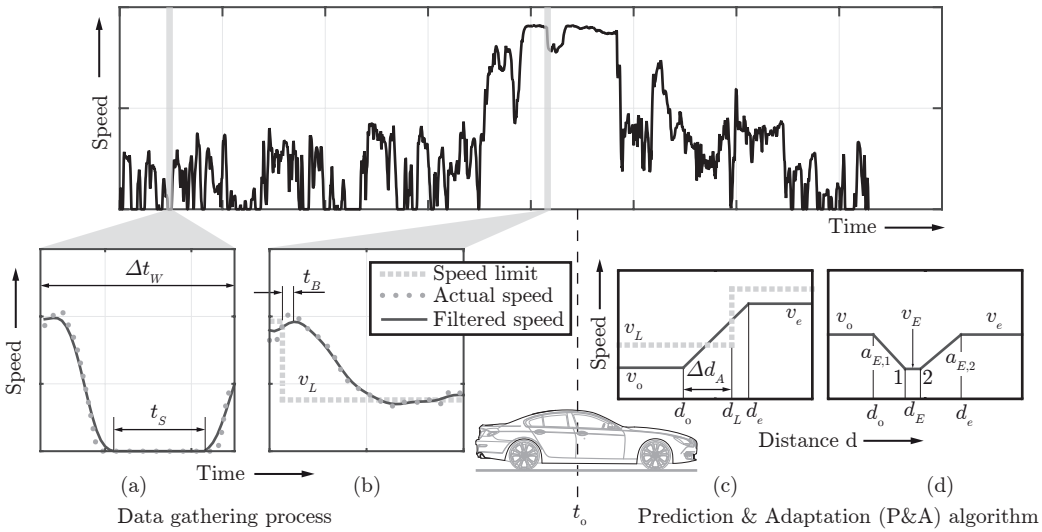

Figure 3.30.: Schematic representation of evaluated and predicted driving data

The *driving data gathering process* identifies characteristic data within a certain time window Δt_W, e.g., the stopping time t_S, see Figure (a), or the time delay t_B after the speed limit v_L drops, see Figure (b), from the previously driven route. This data is then used in the P&A algorithm to predict future driving states, such as the predicted vehicle speed at a certain event v_E. For prediction purposes position-fixed data is used. Figure (c) shows the adaptation of a certain speed limit change. The distance before an acceleration occurs is described with $\Delta d_A = v_0 t_A$, where v_0 is the initial speed, and t_A is the average time before an acceleration manoeuvre occurs. Figure (d) depicts a more general driving event. Although the gathering process is performed on a time basis, the prediction is done in the spatial domain.

speed difference of an acceleration event with the final speed v_e. If the speed difference Δv is positive, the acceleration a_E is positive as well, and vice versa. At speed limit transitions, where drivers typically accelerate before a speed limit transition occurs and then decelerate later, the algorithm accounts for this fact with the time intervals t_A and t_B, respectively, as shown in Figure 3.30(b). Other data, such as the stopping time, are also incorporated, cf. Figure 3.30(a). Assuming a nearly constant driving speed v_0 before such an event occurs, the event position $d_E = d_0$ is evaluated by

$$d_0 = d_L - t_A v_0, \tag{3.127}$$

where d_L is the position of a speed limit change, and t_A is the period of acceleration before the actual speed limit v_L changes. In an acceleration manoeuvre, the event speed v_E is equal to the initial speed v_0, and the assumed constant event acceleration a_E is predicted with the help of Eq. (3.118). The ending position is determined by Eq. (3.124). In the case of a braking manoeuvre, Eq. (3.127) is reformulated as

$$d_0 = d_L + t_B v_0, \tag{3.128}$$

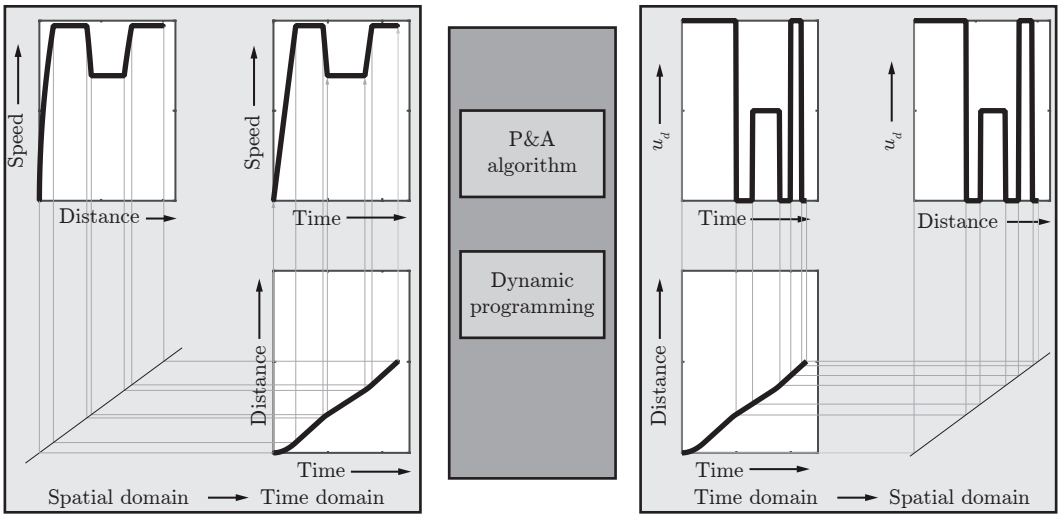

Figure 3.31.: Schematic representation of the time/spatial domain transformation

First, the future power demand is determined in the spatial domain. For optimisation purposes, it is then transformed into the time domain using linear interpolation. The output of the optimisation is a power distribution $u_d(t)$ in the time domain, which is then transformed back into the spatial domain $u_d(d)$.

where the braking event position is $d_E = d_0$, and t_B is the time delay of the braking manoeuvre. The time period of the event is determined by Eq. (3.126), and the ending position is calculated using Eq. (3.124). Figure 3.30(c) shows an acceleration manoeuvre caused by a speed limit change, which is handled in a similar manner. After considering all driver-relevant data in the long-term prediction, the predicted speed profile $v_P(s)$ and the height profile $h(s)$ are transformed into the time domain. It holds that

$$\Delta d_i = \Delta t_s v_i, \tag{3.129}$$

$$d = \sum_{i=1}^{N} \Delta d_i. \tag{3.130}$$

The time interval Δt_s is set to a constant 1 s with respect to the optimisation time and accuracy, see also Chapter 3.2. Moreover, the sample time is in the relevant range of the longitudinal vehicle dynamics, according to [75]. Performing a linear interpolation finally results in a predicted speed profile and height profile in the time domain, see Figure 3.31. The output of the optimisation process is the power distribution $u_d(t)$, which is transformed back into the spatial domain.

The optimisation process described in Chapter 3.2 determines the optimal control for the predicted power characteristics. The predicted speed profile v_P consists of segments with constant speed or acceleration/deceleration phases. When driving in a steady-state, no component torque of inertia acts. The recorded driving cycles for different

drivers show that maintaining a constant exact speed is not realistic. For this reason, the constant speed segments are combined with a noise, which is assumed to represent the driver/vehicle behaviour. Thus, the adapted velocity profile within the originally constant speed segments reads:

$$v_{k+1} = v_k + \nu_k a_k(v_k)\Delta t_s. \tag{3.131}$$

The parameter ν_k is assumed to be normally distributed and varies in the interval $[-1 \quad 1]$, Δt_s is the sampling time, which is set to 1 Hz, and a_k is the acceleration. Here again this arises from the relevant range of the longitudinal vehicle dynamics [75] and corresponds closely to the recorded data. The acceleration a_k again depends on the driving speed v_k at time step k. The optimisation algorithm determines the optimal control $u_d(t)$ and the corresponding state $x(t)$ in the time domain. Since the speed prediction is different from the actual vehicle speed, different positions occur, even though the same moment of time is considered. For the long-term prediction, the time-based state $x(t)$ and control variable $u_d(t)$ are transformed to the spatial domain. Figure 3.31 shows the transformation of the time domain to the spatial domain for the power distribution u_d. For the transformation of the state variable x, a similar approach is applied using the relation stated in Eq. (3.129) and Eq. (3.130).

4
Results

4.1. Real-world Driving Cycle

The implemented advanced operation strategy focuses on improving fuel efficiency in real-world driving situations. Thus, a real-world driving cycle was recorded in the area of Graz, Austria. The route, which consists of urban, suburban and highway sections, is referred to hereafter as the FTG cycle. Figure 4.1 shows the distribution of the route in both the time and spatial domains. The route in Figure 4.2 is about 46 km in distance, which correlates well with the average driving distance for commuters living in

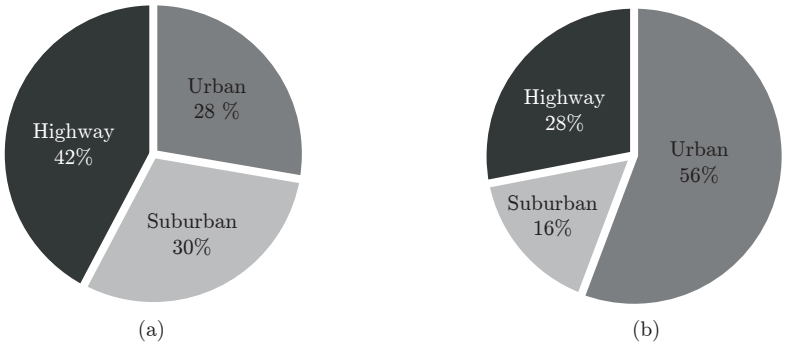

Figure 4.1.: Statistical distribution of the real-world driving cycle

The driving route consists of urban, rural and highway sections. Figures (a) and (b) show the distribution in the spatial and time domains, respectively. The different proportions of the sections arise from the different mean travelling speeds.

Table 4.1.: Comparison of driving cycle characteristics. The characteristic values are based on [144].

Characteristic Parameter	Unit	NEDC	WLTP	FTG Cycle
Total driving time	s	1220	1800	3645
Dead time	s	333	239	577
Relative dead time	%	27.30	13.27	15.63
Distance	km	10.93	23.26	46.27
Mean distance between stops[2]	km	0.78	2.58	1.16
Max. velocity	km/h	130.00	131.30	131.10
Mean velocity	km/h	32.30	46.52	45.70
Mean velocity of motion	km/h	44.40	53.65	54.29
Max. positive acceleration	m/s^2	1.04	1.75	3.10
Mean positive acceleration	m/s^2	0.53	0.42	0.51
Max. negative acceleration	m/s^2	−1.39	−1.50	−3.56
Mean negative acceleration	m/s^2	−0.82	−0.44	−0.52
Percentage of constant velocity	%	62.70	17.16	15.63
Percentage of constant velocity without standstill	%	36.48	4.55	0.90
Maximum height difference	m	0.0	0.0	182.40

Styria [199]. For this reason, and since many people living in the Graz area commute[1], this driving cycle can be considered a typical commuter profile for the Graz area. Unlike legally stipulated driving cycles (e.g., NEDC or WLTP), the FTG cycle includes a height profile. The speed profile was recorded via on-road tests with different drivers at different times of day, in order to take into account different driving styles and environmental conditions. Although the results presented below are based on one specific driving profile (see Figure 3.30), the innovative operation strategy can be applied on any other profile as well. Table 4.1 provides a summary of the characteristic parameters of this individual driving cycle with one specific driver.

It is evident that the FTG cycle and the WLTP are comparable in many parameters. Although the currently valid NEDC is not considered representative of real-world driving scenarios due to its cyclical driving pattern [171], [203], it is nevertheless used for regulatory work. In contrast, its successor, the WLTP, features higher mean velocity, deceleration and acceleration, as shown in Table 4.1. The individual FTG cycle is characterized by more aggressive acceleration and deceleration manoeuvres, and almost no driving at constant speed. According to [144], the key characteristics stated in Table

[1] More than one-third (36.2 %) of commuters living in Graz work in the surrounding region (known as "Graz Umgebung"), while 39.3 % of the commuters living in this surrounding region work in Graz. Of the total number of commuters both into and out of Graz, 45.1 % of them have to travel between 10-19 km daily [199].

[2] Quotient of the total driven distance and the total number of vehicle stops

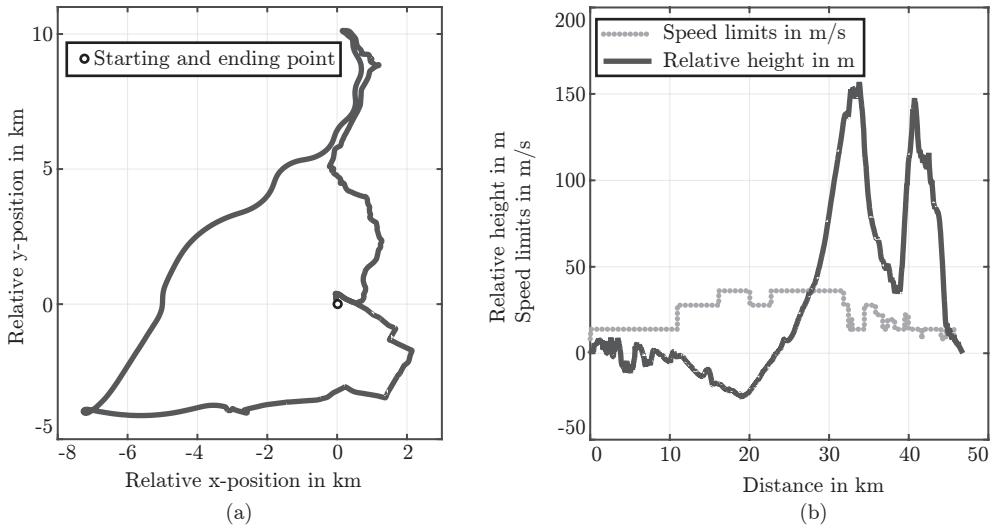

Figure 4.2.: Real-world driving cycle

Figure (a) depicts the driving route in a plane reference system, and Figure (b) shows the relative height profile and the speed limits depending on the distance. Legally stipulated driving cycles do not consider a height profile.

4.1 can be used to classify driving cycles. All three cycles are mixed cycles, consisting of urban, suburban and highway sections. Mixed cycles are characterised by a relatively low mean velocity but a high maximum speed. Nevertheless, the NEDC is near the lower threshold of an urban cycle. Similar results are obtained when considering the relative dead time. According to [144], a relative dead time below 15 % describes a mixed-driving cycle, while values above this limit indicate an urban driving route. By comparing the mean velocity and the mean velocity of motion, all cycles can be further described as urban driving cycles with longer rural areas, according to the classification in [144]. The NEDC is a *modal* driving cycle, since the percentage of constant velocity is high. In contrast, the WLTP and the FTG cycles are *stylistic*. Using legally stipulated driving cycles enables the comparison of different vehicles and measurements in order to enhance vehicle efficiency under standardised conditions (e.g., no auxiliary loads). However, such legally stipulated driving cycles are not suitable for evaluating real-world fuel consumption [121]. Although recorded individual driving cycles cannot guarantee identical driving conditions, they may be closer to real driving behaviour.

The selected speed profile discussed in Chapter 4.1 describes a rather sporty driving behaviour, due to the high longitudinal acceleration and deceleration manoeuvres (see Table 4.1). Since it was recorded in the afternoon during rush hour, especially at the beginning of the driving cycle, many driving situations could not be predicted (e.g., traffic congestion).

4.2. Numerical Analysis of the Investigated PHEV

The following analyses are performed with the predefined P2-PHEV topology shown in Figure 3.19. Table D.1 shows the topology's main vehicle parameters. Both drivetrain modelling approaches are used. The backward-facing vehicle model (see Chapter 3.1.3) is used in the innovative energy management controller, in order to estimate the future component loads of the drivetrain. In contrast, the dynamic vehicle model (see Chapter 3.1.2) is used as a realistic vehicle model which obtains the power distribution factor u_d of the innovative operation strategy as a specific control input. Furthermore, unless otherwise stated, all results below are based on the FTG cycle. First a sensitivity analysis is performed, followed by a performance investigation of the fuel saving potential and the effect on the longitudinal vehicle dynamics. At the end of the chapter, the impacts of the proposed operation strategy are highlighted.

4.2.1. Sensitivity Analysis – Controller Stability

The presented advanced OS uses a model-based optimisation algorithm to improve the overall fuel efficiency of PHEVs. The implemented quasi-static vehicle model (see Chapter 3.1.3) requires a number of drivetrain parameters from the real vehicle (cf. Chapter 3.1.4 and Table D.1). These parameters must be determined precisely. Nevertheless, some parameters (e.g., the total vehicle mass or the air drag) may change across several driving cycles. Other parameters are difficult to evaluate accurately, such as inertias of the drivetrain components.

Using a sensitivity analysis, the influence of uncertainties in specific input parameters of the backward-facing vehicle (e.g., the vehicle mass) is related to its effect on a specific output of the complete simulation model: in this case, the overall fuel consumption of the dynamic vehicle model. Hence, the following test procedure is conducted to analyse the influence of imprecisely measured parameters. In the simulation environment, specific parameters in the backward-facing vehicle model are varied stepwise, whereas parameters in the dynamic vehicle model remain unchanged. The change in total fuel consumption is used to measure the effect of imprecise parameters. Figure 4.3 illustrates the influence of specific parameters.

An imprecise evaluation of the total vehicle mass of the backward-facing model has a slight influence on the total fuel consumption in the context of the proposed operation strategy controller. Varying this parameter between curb weight and the maximum allowed total vehicle weight results in a deviation of less than 1.5 % on the total fuel consumption. Therefore, the energy management controller does not require an exact vehicle mass. However, using a vehicle mass estimator, such as in [93], can further improve the performance of the operation strategy.

Varying the EMG inertia in the model-based optimisation algorithm produces a negligible effect on overall fuel consumption. The maximum change in fuel consumption is less than

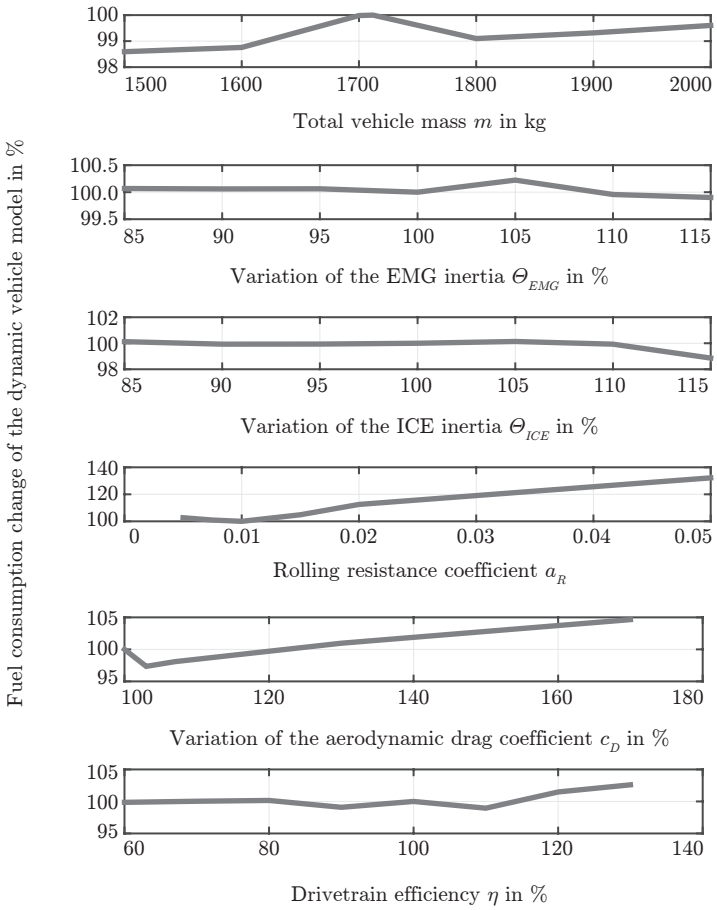

Figure 4.3.: Parameter sensitivity analysis [115]

The total vehicle mass, the inertia of both propulsion units and the overall drivetrain efficiency have a minor influence on the performance of the innovative operation strategy. However, the rolling resistance coefficient and the aerodynamic drag coefficient have to be determined more precisely. Nevertheless, the innovative energy management controller shows a robust behaviour to changes in the aforementioned vehicle parameters.

0.5 % over the entire variation range of ± 15 %.

Varying the ICE inertia produces nearly the same result as the variation of the EMG inertia. Over almost the entire variation range of ± 15 %, the effect on the overall fuel consumption is limited.

In contrast to the component inertias, the rolling resistance coefficient a_R may vary frequently depending on different road surfaces and environmental influences. In Figure 4.3, the reference rolling coefficient is set to 0.01, which represents a good asphalt road. In the simulation environment, the rolling resistance depends exclusively on the vertical

Table 4.2.: Different rolling resistance coefficients a_R on even, ideally stiff roads for constant tyre pressure, adapted from [86]

Road Surface	a_R
Firm asphalt	0.005-0.015
Firm gravel	0.02-0.03
Tarred gravel	0.04-0.04
Good earth path	0.05-0.15
Wet, soaked surfaces	0.15-0.35

load of the tyres, which is a common approach [86]. In reality, the rolling resistance is also a function of the vehicle speed. According to [86] and [135], only at low speed is the rolling resistance approximately constant and near to 0.01. Besides the vehicle speed and the vertical tyre load, the overall rolling resistance also depends strongly on the characteristics of the road, the tyre pressure and the tyre temperature. Deformation of the road surface and water films also increase the rolling resistance. Table 4.2 shows the rolling resistance coefficient for different road surfaces at a given constant tyre pressure. Varying the rolling resistance has a strong influence on total fuel consumption. Nevertheless, assuming that the vehicle is driven primarily on good asphalt roads and that rain sensors are able to capture the weather conditions, the rolling resistance coefficient can be approximated with sufficient accuracy, which limits the variation range. For instance, if the coefficient varies within the range from 0.005 to 0.015, the sensitivity analysis shows that the total fuel consumption increases by less than 4 %.

Figure 4.3 highlights the almost linear influence of the aerodynamic drag on the overall fuel consumption. Adding various attached parts (e.g., roof racks or even pulling a caravan) significantly modifies the aerodynamic drag coefficient (see Table 4.3). Beyond the aforementioned modifications, there are many other factors that influence aerodynamic drag, such as the state of the radiator grill [181]. Modifying the aerodynamic drag coefficient within the range stated in Table 4.3 increases the total fuel consumption by approximately 5 %. A concurrent increase of the total frontal area of the vehicle or vehicle-caravan combination is not considered within this research.

Evaluating the drivetrain efficiency is a difficult task, since there are many influencing factors, including the dependency on the rotational speed and the current component load. The overall powertrain efficiency is successively changed in the range of ±40 %. An imprecisely determined drivetrain efficiency leads to a nearly constant influence over a wide variation range. The maximum deviation is less than 2 %.

Figure 4.3 also shows areas where a deviation from the real to a theoretically worse value leads to a slight improvement of the overall fuel consumption. This phenomenon can be explained by considering the whole simulation environment. Since the vehicle models used vary (see Chapter 3.1), the optimal result for the quasi-static vehicle model is not necessarily the optimum for the dynamic vehicle model. Furthermore, a drift

Table 4.3.: Change of the aerodynamic drag coefficient c_D due to attaching parts according to [181]. The values represent the maximum change for each additional component.

Attaching part	Change of c_D in %
Reference vehicle	0 %
Ski rack	+30 %
Bicycle rack on the roof	+60 %
Caravan	+300 %
Vehicle setting	Change of c_D in c_D points
Open side window	+30
Open sun roof	+30

between the two models occurs, especially due to the numerical integrators used to calculate the cumulative fuel consumption and the SOC of the battery. When parameters different from the real value are used subsequently, the drift is partly compensated for and results in a slight fuel consumption improvement. Unlike many studies, [61], [91], [122], which only determined the fuel saving potential in a quasi-static vehicle model without considering any dynamics in the drivetrain, the current research evaluated this potential with a dynamic vehicle model. In summary, an inaccurate parameter determination does not automatically lead to higher overall fuel consumption. However, especially the aerodynamic drag coefficient c_D and the rolling resistance coefficient a_R must be evaluated precisely or have to be adapted to the current driving situation in order to ensure the proper functioning of the innovative operation strategy. Nevertheless, the parameter sensitivity analysis shows the robust behaviour of the proposed method with respect to changes in the aforementioned vehicle parameters.

4.2.2. Performance Analysis – Fuel Saving, Longitudinal Vehicle Dynamics

The technology of hybrid electric vehicles holds great promise for increasing the overall fuel efficiency of passenger cars. Simultaneously, this means of transport also offers potential for improving longitudinal vehicle dynamics, although implementing hybrid electric components means adding additional weight. The first part of this chapter investigates the enhancements in longitudinal vehicle dynamics. The measurements commonly used for the longitudinal vehicle performance are the acceleration capability from 0-100 km/h, 80-120 km/h in the fourth gear, and 80-120 km/h in the fifth gear [114]. Moreover, in [205], the top speed, stopping distance, gradeability and towing capability are discussed as performance criteria.

Table 4.4.: Enhanced longitudinal vehicle performance of the investigated PHEV compared to a conventional ICE-driven vehicle in % [114]

Measurement	Continuous power	Pulse power
0-100 km/h	+30 %	+38 %
80-120 km/h, 4^{th} gear	+28 %	+37 %
80-120 km/h, 5^{th} gear	+35 %	+44 %

Acceleration performance

Table 4.4 summarises the acceleration improvement the PHEV gains by using its continuous and its pulse battery power compared to the baseline vehicle, which is a conventional ICE-driven vehicle with no additional weight. The continuous battery power is available for an indefinite amount of time without damaging or overheating the battery, as long as sufficient electric energy is available. In contrast, the pulse power supply is limited to a short time period, but provides a higher power supply. Sufficient grip potential is assumed.

Although the total vehicle weight increases due to the additional PHEV drivetrain components, the accelerations from 0-100 km/h and from 80-120 km/h can be improved up to 30 % and 35 %, respectively. Using the briefly available pulse power of the battery enables further longitudinal vehicle performance enhancements. The acceleration from 0-100 km/h is up to 38 % faster than with the conventional passenger car, and the performance from 80-120 km/h increases by up to 44 %. Comparing the results in Table 4.4 highlights the importance of the intelligent planning of the energy content of the PHEV. If the SOC is not planned, the PHEV may not use the entire potential of the longitudinal vehicle performance. The performance improvements even when using only the continuous power of the battery are noticeable for drivers. Using the battery's pulse power can enhance the performance by an additional 10 % [114]. The high driveaway torque and the fast response time of the EMG are beneficial for the acceleration performance.

Top speed

The maximum speed of the PHEV depends on the final gear ratio of the gearbox and the final drive. In addition, the total vehicle power affects the top speed characteristics. At high speeds on an even road, the air drag is dominant. Moreover, the air drag increases with the vehicle speed by a power of two, see Eq. (3.62). The top speed is reached if the total propulsion force at the wheels is equal to all driving resistance forces. The EMG of the investigated PHEV is able to support the ICE over the entire speed range. This yields a top speed improvement of about 4 %, as long as there is enough battery power available and sufficient tyre-road grip.

Table 4.5.: Relative improvement of the investigated PHEV's gradeability compared to the conventional ICE-driven vehicle. The gradeability range of different gears for a common vehicle is also shown, based on [133].

Gear	Improvement of σ in %	σ-range in %
1^{st}	+0 %	40-95
2^{nd}	+0 %	25-60
3^{rd}	+45 %	15-45
4^{th}	+82 %	10-35
5^{th}	+94 %	8-28
6^{th}	+101 %	5-22

Gradeability

The gradeability of a vehicle describes the maximum road inclination β a vehicle can move upwards at a constant speed. Reformulating Eq. (3.71) leads to the gradeability expression:

$$\sin\beta = \frac{1}{m_{VEH}g}\left(\frac{T_T}{r_{dyn}} - F_R - F_D\right), \tag{4.1}$$

where the acceleration resistance term F_A does not appear in the formula due to the constant speed manoeuvre. The gradeability is often given as a percentage, which reads

$$\sigma = 100 \cdot \arctan\beta. \tag{4.2}$$

Table 4.5 shows the investigated PHEV's gradeability improvement over the conventional ICE-driven vehicle. In the first two gears, the maximal transferable tyre force is reached; thus, no improvement can be seen. In higher gears, the gradeability is increased by up to 101 % compared to the baseline vehicle. Additionally, Table 4.5 summarises the gradeability range of conventional ICE-driven vehicles according to [133]. The baseline vehicle is within that range.

Similar to the gradeability, the towing capability increases as long as there is enough electric power left. The towing capability is important when pulling a caravan, for example. In this case, the total mass, the aerodynamic drag coefficient and the total frontal area strongly affect the vehicle performance. The braking performance hardly changes, even though the total vehicle weight has increased.

All investigations of the longitudinal vehicle dynamics – top speed, acceleration performance, gradeability and towing capability – emphasise the importance of intelligently balancing the SOC of the PHEV. Ensuring sufficient energy content of the battery is important to improve the overall vehicle performance.

Table 4.6.: Comparison of optimum fuel saving results of the investigated PHEV for different driving cycles. The fuel saving potential is based on the same PHEV with its baseline strategy.

NEDC (4x)	**WLTP** (2x)	**FTG Cycle** (1x)
9.7 %	8.2 %	11.7 %

Overall fuel efficiency

Almost all longitudinal vehicle performance criteria can be improved by adding sufficiently powerful hybrid drivetrain components. Nevertheless, the improvement strongly depends on the available energy content of the battery. The proposed innovative energy management controller is able to intelligently plan the battery's energy content and simultaneously reduce the overall fossil fuel consumption of PHEVs.

Table 4.6 highlights the maximum attainable fuel saving potential of the investigated PHEV compared to its baseline strategy for different driving cycles. For comparison reasons, the NEDC is driven four times in a row, and the WLTP is driven two times in a row, in order to ensure approximately the same driving distance. The results assume perfect knowledge of the entire driving cycle, which is not actually realistic or causal. Nevertheless, the results can be used to assess the performance of a causal operation strategy. First, due to the fixed, predefined rules and the fact that the route ahead is not considered, the baseline strategy enables different fuel saving performances for different driving cycles. The difference in the optimal fuel saving potential can be explained by the different characteristics of the driving cycles. Due to the lower mean velocity (see Table 4.1), the NEDC has less irreversible drag loss than the WLTP, resulting in higher theoretical fuel savings. The FTG cycle and WLTP have comparable characteristics, as shown in Table 4.1, but the real-world driving cycle includes a height profile.

Figure 4.4 represents the SOC traces of different PHEV operation strategies over the entire driving cycle. The thin dashed grey line depicts the baseline strategy. This strategy utilises the electric traction motor as often as possible, without considering the remaining driving route. The lack of route information results in a significant decrease in the SOC at the beginning of the driving cycle. Thus, the electrical system availability – a measure that identifies the time period where the electric energy is above a certain threshold – is low, at only 23.4 %. At about 10 km of distance, the operation strategy switches to charge-sustaining and maintains the battery's energy content at a rather low SOC level. At first, almost no fossil fuel is consumed; however, in charge-sustaining operation mode, the ICE has to provide almost all traction power. This results in an increase of +13.3 % in total fuel consumption compared to the optimum operation strategy.

The solid black SOC characteristic in Figure 4.4 depicts the reference strategy – a predictive operation strategy. The future power demand is predicted with the help of the speed

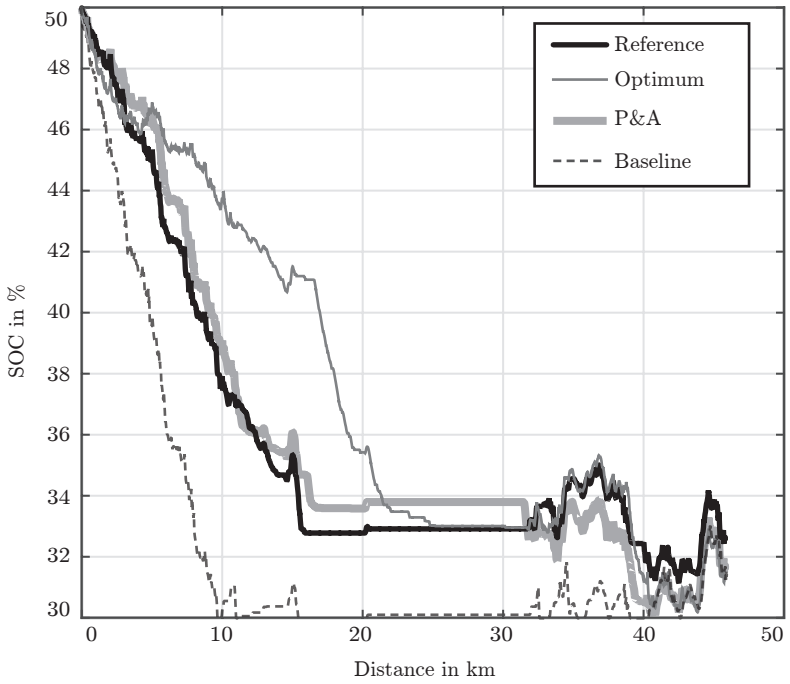

Figure 4.4.: Comparison of the SOC traces of different operation strategies

The baseline strategy uses no prediction algorithm. All other strategies utilise additional information about the upcoming route and driving characteristics to further improve the overall fuel efficiency.

limits of the upcoming driving route and predefined, driver-independent acceleration characteristics and information about the future height profile. This reference operation strategy is able to increase the electrical system availability up to 91.8 %. Although the overall fuel efficiency is better than the baseline strategy, this strategy consumes +7.3 % more fuel than the optimum operation strategy. The average predicted power demand is often higher than the actual one, especially in urban areas, which results in a higher SOC level at the end of the driving cycle.

The proposed innovative energy management controller, which is called P&A, is represented by the thick solid grey line in Figure 4.4. This controller can improve performance by adapting the predicted power demand to the individual driving style. This allows the operation strategy to end up with a lower SOC level. The electrical system availability is a bit lower than with the reference strategy, but it is still at a very high level (86.8 %). Moreover, the overall fuel consumption decreases further, although it remains about +5.7 % higher than the optimum level. This is equivalent to an increased fuel efficiency of +1.4 % and 6.7 % compared to the reference and baseline strategies, respectively.

Table 4.7.: Comparison of different HEV operation strategy results. The fuel consumption of the optimum operation strategy is used for comparison issues; all other values refer to that optimum.

Characteristic Parameter	Baseline	Reference	P&A	Optimum
Electrical system availability[3]	23.40 %	91.80 %	86.80 %	87.80 %
Fossil fuel consumption	113.30 %	107.30 %	105.70 %	100.00 %
SOC_{end}	31.25 %	32.54 %	31.71 %	31.40 %

The thin grey line in Figure 4.4 shows the optimum result, which can only be achieved if the entire power demand of the driving cycle is precisely known in advance. Due to the perfect knowledge of the upcoming speed profile and route, the operation strategy is able to maintain the energy content of the battery in the most fuel-efficient manner possible. Especially in the first approximately 15 km, which consist of mainly urban driving, the SOC is balanced at a higher level than all others. This transpires because of the exact advanced long-term knowledge about future traffic situations, such as interactions with other road users, traffic lights and stop-and-go traffic, over the entire driving cycle. Notice that the driving cycle was recorded during the afternoon rush hour. Consequently, there were many driving situations which could not be predicted long-term. This explains the deviation of the SOC trace of the optimum operation strategy and the two other predictive approaches in Figure 4.4.

Table 4.7 summarises all operation strategies. With very similar SOC levels at the end of the driving cycle SOC_{end}, different fuel savings and electrical system availabilities can be achieved. Nevertheless, an accurate prediction of the future driving states enables a lower SOC_{end}.

To enhance the overall fuel efficiency, the advanced PHEV operation strategy frequently changes its operation mode (see Figure 4.5). A power distribution factor u_d of 1 represents pure electric driving, whereas $u_d = 0$ corresponds to pure ICE driving. In the range of $0 < u_d < 1$ both propulsion units work together. Frequent changes of the operation mode may be advantageous for the overall fuel efficiency. Nevertheless, this can negatively influence the drivability of the vehicle. Detailed research on the drivability is not part of this thesis, but a qualitative assessment was done using the switching time between different driving modes. The detailed representation in Figure 4.5 shows that the switching time is rarely below 2 s. The implementation of the algorithm allows changes with a maximum of 1 Hz. The influence of the frequently changing ICE operation mode – ICE on/off or idling – has to be investigated in detail in future work.

[3]It is defined as the period of time during which the SOC of the battery is above a certain threshold.

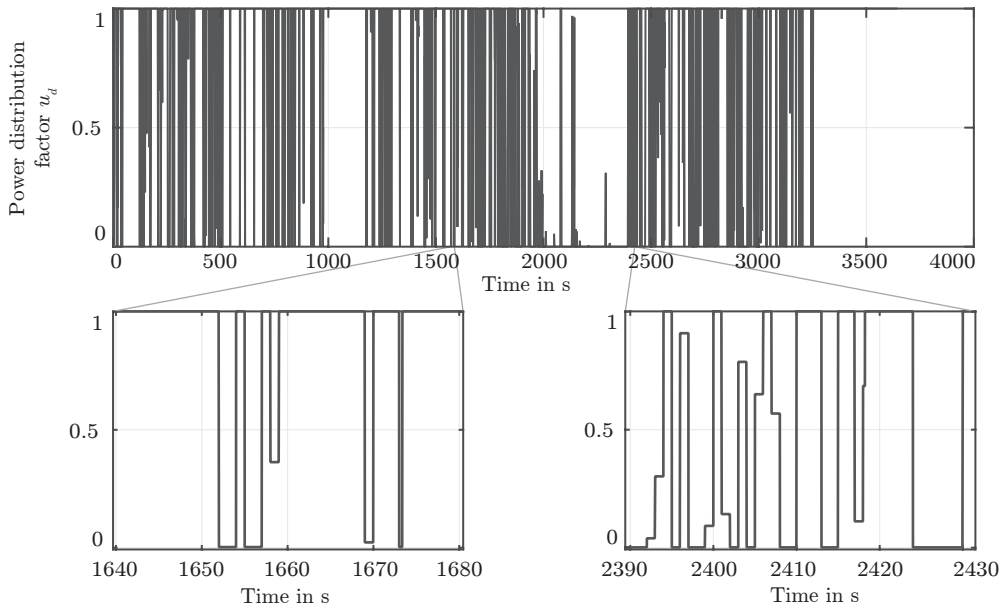

Figure 4.5.: Power distribution factor characteristics u_d of the innovative P&A strategy

A power distribution factor $u_d = 1$ describes pure electric driving, while $u_d = 0$ is pure ICE driving. If $0 < u_d < 1$, the PHEV operates in its hybrid mode. It is evident that duty-cycles below 2 s are infrequent. However, frequently changing operation modes – especially those where the ICE is switched on/off – influence the overall vehicle behaviour, such as drivability.

Computing time

Computing time is a crucial issue in vehicle application, and DP applications are known to be time consuming. However, introducing a multi-level optimisation approach, such as the two-level dynamic programming approach in Chapter 3.2.6.4, effectively reduces the computational burden. Moreover, the single-dimension, quasi-static vehicle optimisation model in combination with an adequate grid resolution contribute to a low computing effort. Using a consumer notebook (see Table 4.8), the computing time for the long-horizon prediction optimisation is about 52 s. In contrast, the short-horizon prediction optimisation takes a maximum of 0.7 s, depending on the travelling speed. Nevertheless, state-of-the-art automotive control units, such as [107], have much less computing capacity.

4.3. Impact of the Proposed Operation Strategy

The operation strategy of HEVs has a significant influence on the vehicle performance. The proposed intelligent energy management controller is able to concurrently increase the overall fuel efficiency and enhance the longitudinal vehicle performance of a P2-

Table 4.8.: The simulation environment used here is based on a consumer notebook.

Component	**Specification**
Operation system	Windows 7 Enterprise x64
Central processing unit (CPU)	i7-2860 QM
Random access memory (RAM)	16 GB
MATLAB version	7.11.0.584 (R2010b) win32

PHEV drivetrain layout. Performance criteria such as acceleration capability, top speed and gradeability are improving remarkably.

However, the operation strategy has to intelligently maintain the energy content of the battery over the entire driving route. High electrical system availability is a prerequisite. An electrical system availability of about 87 % of the innovative operation strategy ensures that the PHEV can use the entire potential of the longitudinal performance. Moreover, the anticipatory planning of the SOC simultaneously improves overall fossil fuel consumption. The results show that improvements of up to 11.7 % are theoretically possible for the pre-described route, compared to rule-based operation strategies.

Besides enhancing the longitudinal vehicle performance, the hybrid electrical system availability and the overall fuel efficiency, the advanced operation strategy can also reduce GHG emissions. The European Union emission reduction targets require that in 2015 new cars do not emit more than an average of 130 g/km CO_2, and in 2020 the threshold is lowered to 95 g/km. All thresholds are related to the current legally stipulated driving cycle, the NEDC. Car manufacturers have to pay an excess emissions premium if the average CO_2 of their fleets exceeds those thresholds. In 2019, these fees can be up to €95 for each gram of CO_2 exceeding the current threshold. The P2-PHEV studied with the advanced operation strategy emits about 110 g/km CO_2 in a real-world driving cycle. This is 15 % less than the 2015 emissions target. However, this level exceeds the desired level for 2020 by about 16 %. Additional costs for OEMs of about €1,425 for each car sold will arise in 2019[4]. However, taking into account the total vehicle power of more than 200 kW, and that the CO_2 level is related to a real-world driving cycle, the proposed operation strategy can help approach future emissions targets, even for high-power vehicles. In order to clarify the benefits of the innovative operation strategy, a currently available reference vehicle with comparable performance data is used in simulation for comparison reasons. It has nearly the same weight-to-power-ratio and almost the same maximum power. The overall CO_2 emissions and thus the total fossil fuel consumption of the simulated PHEV decrease by about 25 %.

Moreover, comparing the additional potential of the advanced OS, the baseline and the reference strategy, car manufacturers may use the innovative algorithm in a different way. Increased efficiency in using the battery's energy content may motivate OEMs to reduce

[4]Assuming that the average CO_2 level is similar to the investigated vehicle

the number of cells in the battery pack so that the resulting total fuel consumption level can be similar to that of the baseline strategy. According to [108], battery costs are the dominant component as far as production costs are concerned. Reducing the number of battery cells decreases the overall fuel efficiency, but both weight and cost decrease as well. In addition, the innovative operation strategy does not cause any additional material costs, and it can be used in different vehicle types with similar drivetrain layouts.

Reduced production costs may lead to a lower purchasing price for customers. At a minimum, they will be able to experience the enhanced longitudinal vehicle performance. In Austria, customers profit from a reduced NoVA tax. Compared to the reference vehicle, the tax is reduced by up to 7 %. Moreover, the annual vehicle motor tax decreases by about € 720. This means a cost reduction of about 49 % in annual vehicle taxation. In 2014, the average driving distance per year was about 13,100 km [218], and the average costs for diesel was € 1.296 per litre [149]. Driving a PHEV with the proposed intelligent operation strategy enables annual fuel costs savings of about € 70.

The aforementioned examples emphasise that combining the investigated PHEV drivetrain configuration with the proposed innovative operation strategy will yield noticeable benefits in the form of reduced taxes and costs for both OEMs and consumers as well.

5

Summary and Conclusion

This thesis addresses the development of highly efficient and more environmentally friendly vehicles by introducing an innovative operation strategy for PHEVs. This chapter gives a summary of the present research and concludes with a final statement.

Chapter 1: Introduction. This chapter pointed out that individual mobility is a basic prerequisite that ensures economic growth and increases the standard of living. Although conventional diesel and gasoline-driven vehicles are still dominant, economic, ecological, social and political factors are encouraging the development of vehicles with alternative drivetrains. The Earth's crude oil reserves, which are finite and non-renewable, stand in contrast to the increasing world population and the expected increase in mobility in developing countries. Moreover, GHG emissions from the transportation sector have more than doubled since 1970 and were still increasing at a faster rate than any other energy end-use sector in 2010. Hence, vehicles are partially contributing to global warming, which contributes to rising sea levels. In order to manage these trends, national and international regulators are tightening fuel consumption and emissions restrictions. The introduction of *low-emission zones* (LEVs) and *zero-emission zones* (ZEZs) in many cities is one measure to address these problems. Moreover, mandatory emission reduction targets – in Europe the average CO_2 emissions of the entire vehicle fleet has to reach 95 g/km in 2020 – and additional penalty payments are spurring the development of more environmentally friendly vehicles. Vehicles with alternative drivetrains are able to effectively reduce or even eliminate local emissions in urban areas. The present research focused on hybrid electric vehicles (HEVs), which offer the best of both electric and combustion-engine propulsion (i.e., purely electric urban driving and high operating range), although the vehicle mass and purchase costs are high.

This chapter also discussed different test procedures for evaluating the overall fuel con-

sumption and exhaust emissions of conventional vehicles driven by internal combustion engines (ICEs), HEVs and plug-in HEVs, as well as for evaluating in both real-world traffic situations and simulations. The chapter concluded with different studies about the future market penetration of vehicles with alternative drivetrains – political interventions and subventions have a strong influence on their market shares.

Chapter 2: State-of-the-Art Hybrid Electric Vehicles. The present research focused on the development of an operation strategy (OS) for PHEVs. However, this chapter started with a classification of HEVs according to their degree of hybridisation (DoH) – a measure that quantifies the power capability of the electric traction system. The DoH helps to distinguish between different HEVs, namely micro, mild, full and plug-in HEVs. Hybrid electric vehicles enable additional operation modes, which efficiently reduce overall fossil fuel consumption. Operation modes such as ICE start/stop, coasting, e-drive, boosting, recuperation, load point shifting and phlegmatisation are inherent to HEVs. However, the effectiveness of these functions depends strongly on the DoH.

The HEV's drivetrain layout is more complex than that of conventional ICE-driven vehicles. Nevertheless, different HEV drivetrain configurations have become widespread. In general, there are three main HEV concepts – series, parallel and power-split HEVs. In series HEVs, there is no direct mechanical connection of the ICE to the drive shafts. An electric traction motor/generator (EMG) supplies all necessary propulsion power. Such vehicles offer good fuel saving performance if relatively high driving dynamics are predominant (e.g., stop-and-go urban traffic), but the required multiple energy conversions are disadvantageous. In contrast, in parallel HEVs, both propulsion units – ICE and EMG – are mechanically linked to the drive shaft. Depending on the arrangement and dimensioning of the EMG, there are different parallel drivetrain variations. The present thesis investigated a P2-HEV, in which the EMG is mounted between the clutch (CL) and the gearbox (GBX). The benefit is that the clutch allows for independent driving of the EMG without ICE drag losses. However, an ICE operation in a steady-state in areas of high efficiency is not guaranteed. Power-split HEVs are the final main drivetrain layout. At least one planetary gear-set (PGS) is used to distribute the mechanical power of the ICE to an electrical and mechanical power path. In combination with two EMGs, the PGS represents an electrical continuously variable transmission (eCVT). On the one hand, the high flexibility in selecting an appropriate ICE operation point and the elimination of the conventional GBX and CL are advantageous. On the other hand, the increased system complexity, vehicle weight and costs are unfavourable.

Besides the drivetrain layout of HEVs, their operation strategy is a key success factor for outstanding fuel savings, enhanced longitudinal vehicle performance and a high level of safety and comfort. The state-of-the-art OSs were also discussed in this chapter. Different OSs are used for on-line applications, as well as for benchmark issues.

Rule-based operations strategies (RB-OSs) are widespread in HEVs. These strategies consist of predefined rules and correlations based on expert engineering knowledge and often ensure high ICE operation efficiency by avoiding less efficient operation points. Moreover, *fuzzy logic* – a generalisation of rule-based OS – is applied to further improve

the performance of HEVs. The intuitive selection and the straightforward implementation are favourable. However, RB-OSs may not completely achieve optimal fuel economy.

In contrast, *optimal* operation strategies may determine the optimal fuel economy. However, this approach assumes perfect knowledge of the upcoming route a-priori, which is rarely possible in real traffic. Nevertheless, methods such as *dynamic programming* are often used as performance benchmarks for real-time-capable operation strategies. *Deterministic DP* (DDP) is used for benchmarking a single driving cycle, whereas *stochastic dynamic programming* (SDP) is used to derive an optimal solution for a family of driving cycles by using probability distributions of selected driving cycles. *Pontryagin's minimum principle* (PMP) is also used for benchmarking, but its performance in finding a solution depends on the problem formulation.

Due to the inherent challenge of knowing the entire driving cycle a-priori, *suboptimal* operation strategies are developed in order to increase the overall fuel efficiency of HEVs. The *equivalent consumption minimisation strategy* (ECMS) reduces the optimisation problem to an instantaneous minimisation. Prediction of the route ahead enables additional fuel savings. Thus, in recent years, researchers have developed OSs that incorporate additional information from roadside sensors, *intelligent transportation systems* (ITSs) and *geographical information systems* (GISs). For plug-in HEVs (PHEVs), multi-level energy management controllers based on *model predictive control* (MPC) or *stochastic model predictive control* (SMPC) are often used. The recent introductions of PHEVs by established OEMs highlight the potential and future trend of such a means of transport.

The main scientific contributions of the present thesis – introduction of a holistic energy management controller, innovative long-term prediction and adaptation (P&A), and an analysis in a dynamic vehicle model – completed this chapter.

Chapter 3: Methodology. A numeric simulation environment was established to investigate the benefits of additional information about the route ahead. It consists of a *quasi-static vehicle model*, which was used for optimisation in this work. A realistic *dynamic vehicle model* was used to prove the potential of the innovative operation strategy in real-world driving cycles.

Chapter 3.1 also discussed in detail the difference between the two model approaches – quasi-static and dynamic vehicle modelling. The chapter then described in depth the implemented component models, such as the internal combustion engine, clutch, electric motor/generator, battery, gearbox, final drive, tyre, the holistic vehicle model, driver model, hybrid control unit and auxiliaries, including their control units and all relevant assumptions. The innovative holistic energy management controller was then introduced, which selects an appropriate operation mode path based on the available information. Subsequently, the difference of the quasi-static model approach to the dynamic modelling is delineated. Thus, Subchapter 3.1 closed with detailed information about the implemented P2-PHEV model with its main drivetrain layout and parameters.

Subchapter 3.2 described the applied *dynamic programming* approach. Dynamic pro-

gramming is a powerful tool for optimising non-convex and non-linear multi-stage optimisation problems with control and state constraints. Its fundamentals – the *Principle of Optimality* and the *Bellman equation* – were discussed in detail with respect to applications in automotive systems. Moreover, this subchapter highlighted the relevant implementation aspects, such as approximation, the proper choice of state and control variables, and the selection of an appropriate cost functional in order to enhance the computation performance. The subchapter concluded with a discussion of the two applied controller structures, namely the *one-level DP* and the *two-level DP*.

The innovative long-term prediction and adaptation approach was the last part of this chapter. First, it highlighted the complexity of predicting future driving states, due to the interlaced interactions of the driver-vehicle-environment system. The P&A approach is based on fixed-location information, such as speed limits or height profile of the upcoming route obtained from *global navigation satellite system* (GNSS) signals and digital maps. However, the core of the innovative long-term prediction algorithm is to gather, process and utilise driving data from the driver's previous trips in order to increase the long-term prediction accuracy, without requiring other information, such as roadside sensors. Methods to approximate the driver's individual driving style, such as the acceleration/deceleration behaviour depending on the current driving speed or the driver's individual sense of comfortable maximum lateral vehicle acceleration, were applied to incorporate position-fixed information. The chapter concluded with the required transformation between the spatial and time domains and combined the drivetrain modelling, optimisation, prediction and adaptation parts into one coherent methodology.

Chapter 4: Results. First, this chapter introduced the recorded, institute-specific, real-world driving cycle, called the FTG cycle, and analysed it in detail. This cycle, which is very comparable with the upcoming legal driving cycle *worldwide harmonized light vehicles test procedure* (WLTP), includes a height profile as well. In addition, a numerical analysis of the investigated PHEV was performed, including an analysis of the energy management controller's stability in the face of sensitivity to variations in the main vehicle parameters. The sensitivity analysis showed a robust behaviour of the innovative OS for PHEVs with respect to changes in specific vehicle parameters.

The scope of this thesis was to develop an innovative operation strategy for PHEVs in order to simultaneously improve the overall fuel economy and enhance longitudinal vehicle dynamics by incorporating information about the upcoming route and the individual driving style in the supervisory control.

This chapter highlighted that typical performance indices – acceleration performance, top speed, gradeability and towing capability – for the investigated PHEV drivetrain layout may outperform the conventional ICE-driven vehicle with less overall vehicle weight. The acceleration performance improves by up to 44 %, the top speed by 4 %, and the gradeability in higher gears up to 101 %, assuming there is sufficient electric energy available from the battery.

In addition, compared to state-of-the-art energy management control, the presented in-

novative approach is not only based on static digital map data, but also includes the individual driving style in long-term prediction. The research highlights that the overall fuel consumption is only 5.7 % higher than the global optimum obtained by DP with perfect a-priori information of the driving cycle, even if the long-term prediction is not exact, which is the case in most driving situations. Moreover, the energy content of the battery is maintained for the entire trip, ensuring sufficient energy reserves to instantly provide the total vehicle system power. Compared to a simple charge depleting/sustaining OS, the electrical system availability increases by up to approximately 3.7 times, from 23.4 % to 86.8 %. However, there are still uncertainties about future driving situations, such as the conditions of the surrounding traffic environment. The present research shows that, especially in urban areas, driving situations are hard to predict in the long-term, which leads to a deviation from the optimum performance.

The proposed DP-based, two-level supervisory control approach effectively reduces computational time by splitting the optimisation problem into a long-term task and a short-term task. The reduced first-order vehicle model used for optimisation is based on only one state and only one control variable – state of charge (SOC) and power distribution factor u_d. Although this reduces the computational burden, the long-term optimisation is still time intensive. Thus, real-time application is promising, particularly when the computing power of the HCU is enhanced.

Inputs from advanced information technologies, such as *intelligent transportation systems* (ITSs), *geographical information systems* (GISs) or C2X-communication, can be included. However, these technologies are not widely available or are not ready for serial production. Therefore, the proposed innovative energy management controller relies only on past recorded vehicle and driving data, the availability of GNSS signals and additional information about the upcoming height and route profile. Nevertheless, the structure of the data processing algorithm allows for the integration of average speed profiles recorded by roadside traffic sensors.

Finally, it is important to emphasise that, beyond the improved fuel economy and system availability, the costs for both car manufacturers and consumers may be reduced. The proposed OS can effectively help to achieve current and future CO_2 targets, even in a real-world driving cycle. Even high-performance vehicles (>200 kW) are able to approach the goal of an average of 95 g/CO_2 across the entire vehicle fleet by 2020.

Final statement: The present research work provides an in-depth analysis of PHEVs, and especially their OSs. The introduced innovative P&A algorithm, based solely on the vehicle, the driver's past trip data and GNSS signals, was able to enhance fuel efficiency in areas where no average speed profile information is available from roadside traffic sensors. One novel feature is the long-term prediction and adaptation to driver behaviour, in order to increase the prediction accuracy and decrease computational effort. The research has demonstrated that not only fuel efficiency is increased, but also overall electrical system availability. The OS enables a high level of vehicle performance and comfort, while keeping fossil fuel consumption at a low level. This will lead to improved customer acceptance and thus higher market shares for HEVs, which, along with reducing GHG emissions, should be the primary goal of developing OSs for HEVs.

A

HEV Drivetrains

A.1. Classification by DoH and Battery Capacity

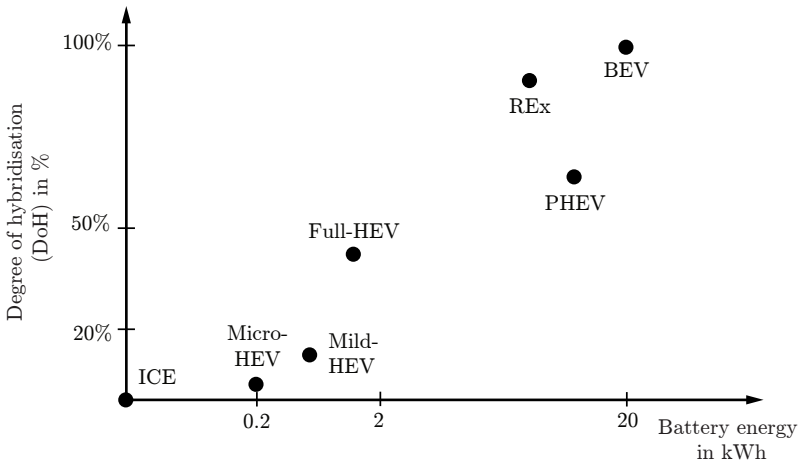

Figure A.1.: Classification of HEVs based on their DoH and battery capacity [66]

Hybrid electric vehicles are classified according to their DoH. The conventional ICE-driven vehicle (ICE) has a DoH of 0, whereas a battery electric vehicle (BEV) has a DoH of 1. Micro/mild/full HEVs, plug-in HEVs (PHEVs) and range-extender vehicles (REx) have a DoH within the interval]0 1[.

A.2. Variations of a P1-HEV Drivetrain Layout

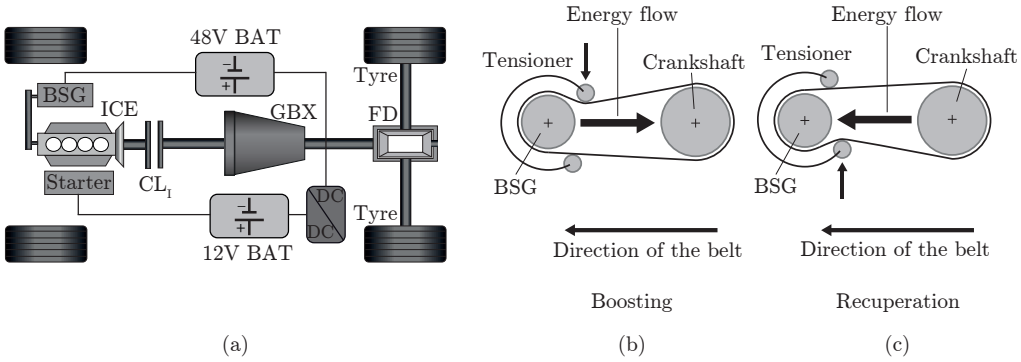

(a) (b) (c)

Figure A.2.: Schematic representation of a belt-driven starter generator (BSG), adapted from [196]

The BSG is a variation of a P1-HEV drivetrain topology. It is integrated into the belt drive of the ICE, see Figure (a). Although the integration into conventional drivetrains is easy, the system packaging is slightly increased, and an additional 12 V starter for cold starts is required. Figures (b) and (c) show the necessary belt tensioner, which ensures good power transfer when the engine and alternator modes are toggled between boosting, see Figure (b), and recuperation, see Figure (c) [196].

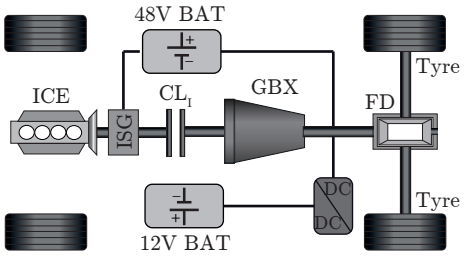

Figure A.3.: Schematic representation of an integrated starter generator (ISG), adapted from [196]

The ISG configuration provides higher system performance than the belt-driven starter generator (BSG), since it is directly mounted on the crankshaft of the ICE. Thanks to the direct power supply and the higher system performance, no additional 12 V starter is required to tow start the ICE reliably, even at low ambient temperatures.

A.3. Characteristics of a Power-split HEV Drivetrain

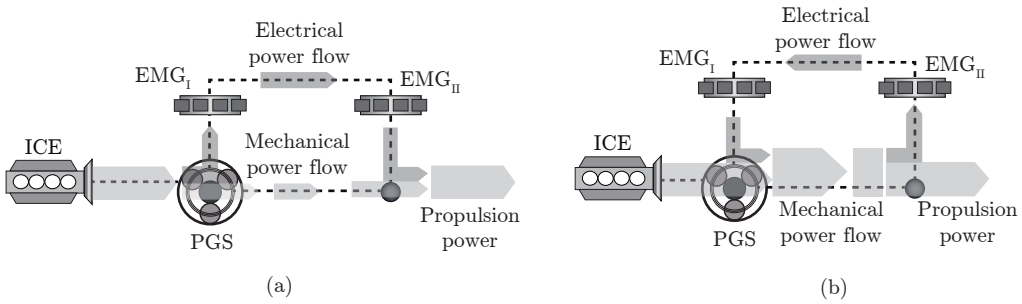

Figure A.4.: Schematic representation of the power flow in a power-split HEV [23]

In a power-split HEV, the power flow in the electrical path is bidirectional. In Figure (a), the power is transferred from EMG_I to EMG_{II}, which represents the common operation mode. In Figure (b), EMG_{II} transmits power to EMG_I. Thus, the power in the mechanical path is the sum of the ICE and EMG_I power. Consequently, the power of the electrical path has to circuit with losses in the system, without contributing to propulsion. This partially produces a high reactive power in the electrical path, and thus decreases the overall vehicle efficiency.

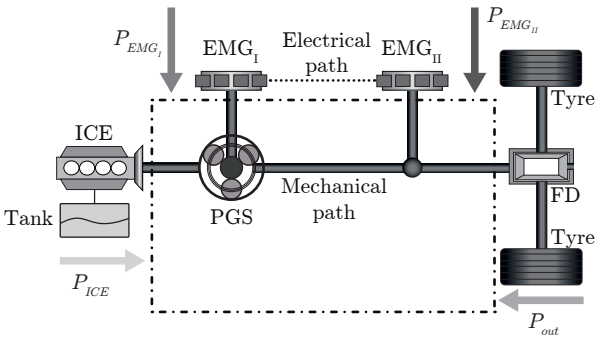

Figure A.5.: Schematic representation of an input-split (L1-In), adapted from [169]

The input-split is a variation of a power-split HEV. At the gearbox input, the power is divided into a mechanical part and an electrical part. The ICE is directly connected to the ring gear, and the EMG_I is connected to the sun gear. Both the EMG_{II} and the planetary carrier are linked with the output drive. Although no battery is required for setting the gear ratio, one is implemented to save energy.

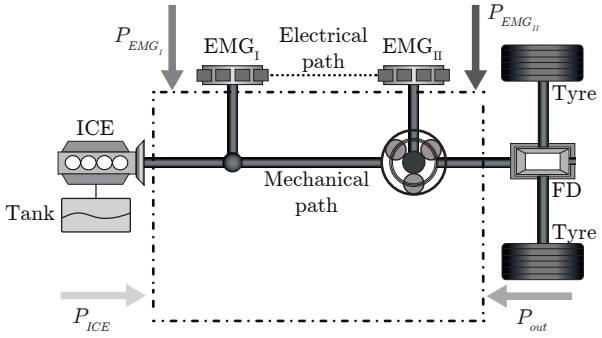

Figure A.6.: Schematic representation of an output-split (L1-Out), adapted from [169]

The output-split is a variation of a power-split HEV. At the gearbox input, the power is divided into a mechanical part and an electrical part. The ICE and the EMG$_I$ are directly connected with the ring gear. The second EMG$_{II}$ is mounted to the sun gear. Only the planetary carrier is linked with the output drive. Although no battery is required for setting the gear ratio, one is implemented to save energy.

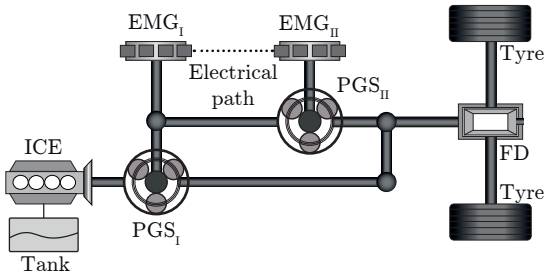

Figure A.7.: Schematic representation of a compound power-split, adapted from [169]

The compound power-split is another variation of a power-split HEV. It consists of two planetary gear-sets (PGSs) and two EMGs. Thus, it has two mechanical paths. The compound power-split is a combination of an input-split (L1-In) and an output-split (L1-Out). The ICE is directly connected to the first ring gear. The sun gear of the first PGS$_I$ is linked with the EMG$_I$ and the ring gear of the PGS$_{II}$. The planetary carriers of PGS$_I$ and of PGS$_{II}$ together form the output drive. The second EMG$_{II}$ is connected to the sun gear of PGS$_{II}$.

B

HEV Control Approaches

B.1. Optimisation

Optimisation requires a cost functional J. The following chapter provides a very rough overview of the most common ones, according to [55].

- Lagrangian cost functional:

$$J = \int_{t_0}^{t_e} h\Big(\mathbf{x}(t), \mathbf{u}(t), t\Big)\,\mathrm{d}t. \tag{B.1}$$

  Equation (B.1) describes the generalisation of an energy/route/time-optimal cost functional [55], where $h(\ )$ is a function, defined by the problem, $\mathbf{x}(t)$ is the state vector, $\mathbf{u}(t)$ is the control vector, and t is the time.

- Cost functional of Mayer[1]

$$J = g\Big(\mathbf{x}(t_e), t_e\Big). \tag{B.2}$$

  This only evaluates the terminal state of the dynamic system at time t_e, where $g(\ )$ describes a function defined by the original problem.

- Cost functional of Bolza[2]

$$J = g\Big(\mathbf{x}(t_e), t_e\Big) + \int_{t_0}^{t_e} h\Big(\mathbf{x}(t), \mathbf{u}(t), t\Big)\mathrm{d}t. \tag{B.3}$$

  Equation (B.3) characterises the combination of the cost functionals in Eq. (B.1) and Eq. (B.2). Consequently, it represents a very general formulation.

[1] German mathematician (1839 - †1908)
[2] German mathematician (1857 - †1942)

B.2. Fuzzy logic

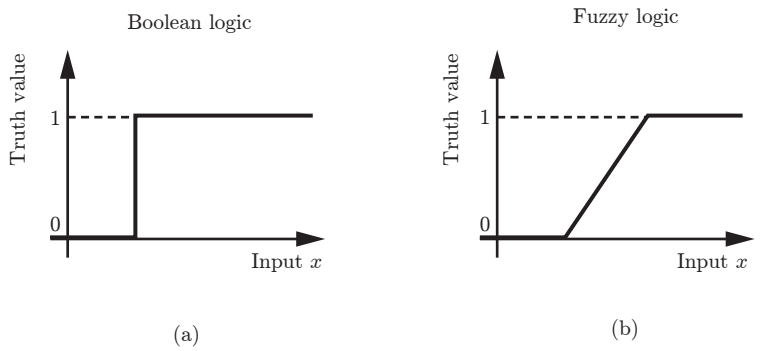

Figure B.1.: Difference between classical Boolean logic and fuzzy logic [198]

Figure (a) shows the classical Boolean logic, where only two truth values true/false (1/0) are possible. In contrast, Figure (b), the fuzzy logic permits truth values within the interval [0 1]. Consequently, an input x is with a certain degree of membership true or false.

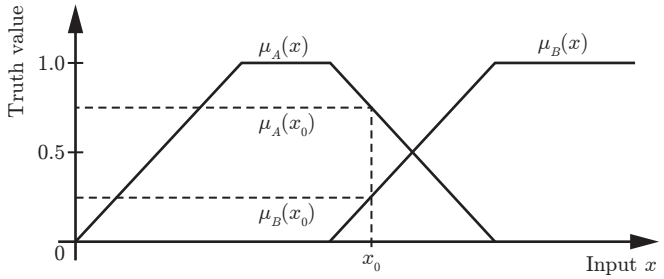

Figure B.2.: Schematic representation of a membership function of FLS [198]

Two fuzzy sets A and B are given, with their corresponding membership functions $\mu_A(x)$ and $\mu_B(x)$. These functions assign to each value x_0 belonging to the basic set $\mathbb{X}$ a degree of membership $\mu_A(x_0)$ and $\mu_B(x_0)$ an arbitrary truth value within the interval [0 1]. In the example given, the degree of membership to the fuzzy set A is $\mu_A(x_0) = 0.75$ and to fuzzy set B is $\mu_B(x_0) = 0.25$. Thus, the input variable $x = x_0$ belongs concurrently to both fuzzy sets.

C
Modelling

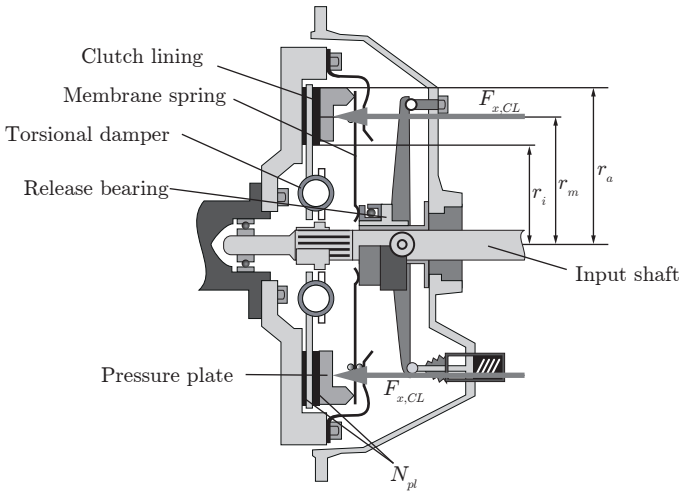

Figure C.1.: Schematic representation of the transferable clutch torque, adapted from [206]

The transferable clutch torque T_{CL}, which depends on the axial contact force $F_{x,CL}$, the average friction radius r_m, the friction coefficient μ and the number of clutch plates N_{pl}, reads: $T_{CL} = N_{pl} \cdot r_m \cdot \mu \cdot F_{x,CL}$. The average friction radius is calculated by $r_m = \frac{2}{3} \frac{r_a^3 - r_i^3}{r_a^2 - r_i^2}$. This relation is often simplified to $r_m = \frac{r_a + r_i}{2}$ [206]; r_a and r_i are the radii of the outer and inner friction linings, respectively.

D

Model Parameters

Table D.1.: Main parameters of the vehicle simulation model

Parameter	Symbol	Value	Unit
Conventional drivetrain			
Total vehicle mass (incl. driver) without additional weight of HEV components	m_{VEH}	1500	kg
Peak power ICE	$P_{ICE,max}$	120	kW
Moment of inertia ICE	Θ_{ICE}	0.25	kgm^2
Aerodynamic drag coefficient	c_D	0.28	-
Frontal area	A_x	2.26	m^2
Dynamic tyre radius	r_{dyn}	0.31	m
Number of gears	N_γ	6	-
Rolling resistance coefficient	a_R	0.01	-
Efficiency gearbox	η_{GBX}	0.98	-
Gear ratio final drive	i_{FD}	3.15	-
Efficiency final drive	η_{FD}	0.96	-
HEV drivetrain			
Peak power EMG	$P_{EMG,max}$	81	kW
Total energy content battery	$E_{BAT,max}$	9	kWh
Moment of inertia EMG	Θ_{EMG}	0.12	kgm^2
Nominal cell voltage	U_{cell}	3.2	V
Number of serial cells	N_s	120	-
Number of parallel cells	N_p	1	-

E

Prediction and Adaptation

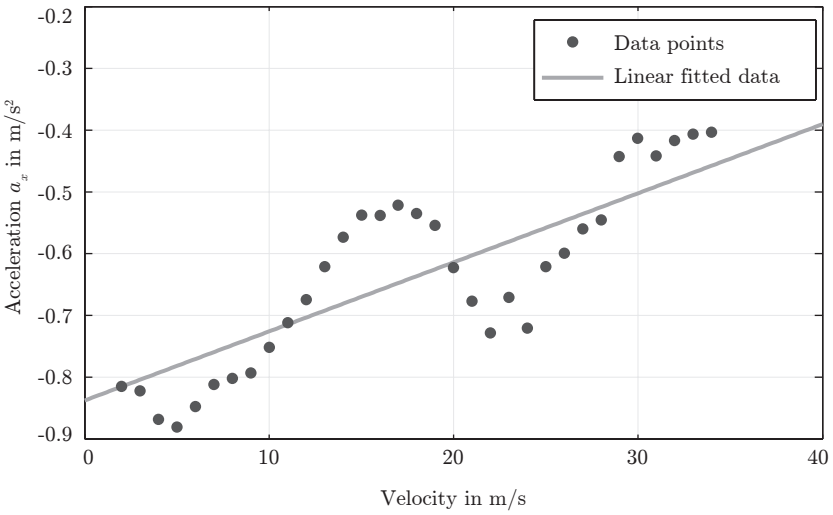

Figure E.1.: Analysis of the deceleration behaviour for the investigated driving cycle

The points represent the original acceleration points based on a certain vehicle speed. It is evident that deceleration decreases with increasing vehicle speed. The line shows the corresponding linearly fitted curve that confirms the aforementioned effect.

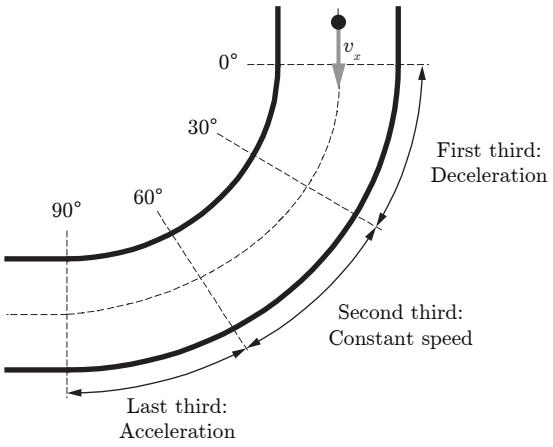

Figure E.2.: Schematic representation of the principle of third sections of a curve [178]

In the first third of a curve, the vehicle decelerates; in the second third, the driver holds the vehicle speed approximately constant; and in the last third, the driver accelerates again.

List of Figures

List of Tables

Bibliography

[1] Normverbrauchsabgabegesetz 1991 (BGBl. Nr. 695/1991 idFBGI. I Nr. 118/2015), 1991.

[2] §3 Mineralölsteuergesetz 1995 (BGBl. Nr. 630/1994 idF BGBI. I Nr. 118/2015), 1995.

[3] Entwicklung von Szenarien der Verbreitung von PKW mit teil- und vollelektrifiziertem Antriebsstrang unter verschiedenen politischen Rahmenbedingungen ELEKTRA. Begleitstudie (Forschungsauftrag) 816074, 2009.

[4] IG-L-Messkonzeptverordnung 2012 (BGBl. Nr. II 127/2012), 2015.

[5] Versicherungssteuergesetz 1953 (BGBl. Nr. 133/1953 idF BGBI. I Nr. 34/2015), 2015.

[6] M. Abdul-Hak and N. Al-Holou. ITS based Predictive Intelligent Battery Management System for plug-in Hybrid and Electric vehicles. In *Vehicle Power and Propulsion Conference, 2009. VPPC '09. IEEE*, pages 138–144, 2009.

[7] J. Adamy. *Regelung für lineare und nichtlineare Regelstrecken*, chapter 6, pages 417–502. Nichtlineare Systeme und Regelung. Berlin, Wiesbaden, 2014.

[8] N. Amann, M. Beck, O. Bitsche, P. Casals, B. Cebulski, C. Ehret, and J. Faßnacht. *Komponenten des Hybridantriebes*, chapter 3, pages 75–300. Kraftfahrzeug-Hybridantriebe. Springer Science+Business Media, Wiesbaden, 2012.

[9] K. Aoki, S. Kuroda, S. Kajiwara, H. Sato, and Y. Yamamoto. Development of Integrated Motor Assist Hybrid System: Development of the 'Insight', a Personal Hybrid Coupe. *SAE Technical Paper*, 2000.

[10] N. Ardey, M. Bollig, S. Juraschek, M. Klüting, and C. Landerl. Plug and Drive – das neue Plug-In System von BMW. *36. International Vienna Motor Symposium 2015*, pages 214–228, 2015.

[11] Statisik Austria. Kfz-Zulassungen 2014. Pressekonferenz, 2015.

[12] M. Back. Prädiktive Antriebsregelung zum energieoptimalen Betrieb von Hybridfahrzeugen. Doctoral thesis, 2005. Institut für Regelungs- und Steuerungssysteme, Universität Karlsruhe (TH).

[13] G. Banse. *"Nicht so exakt wie möglich, sondern so genau wie nötig!" Das Einfachheitsprinzip in den Technikwissenschaften*, pages 93–104. Einfachheit als

Wirk-, Erkenntnis- und Gestaltungsprinzip. Sitzungsberichte Leibniz-Sozietät der Wissenschaft, Berlin, 2011.

[14] B. M. Baumann, G. Washington, B. C. Glenn, and G. Rizzoni. Mechatronic design and control of hybrid electric vehicles. *Mechatronics, IEEE/ASME Transactions on*, 5(1):58–72, 2000.

[15] R. E. Bellman. *Dynamic Programming*. Number 3. Dover Publications, New York, 2003.

[16] R. E. Bellman. *A Multi-Stage Allocation Process*, chapter 1, pages 3–60. Dynamic Programming. Dover Publications, New York, 2003.

[17] R. E. Bellman. *Preface*, pages VII–XVIII. Dynamic Programming. Dover Publications, New York, 2003.

[18] R. E. Bellman. *The Structure of Dynamic Programming Process*, chapter 3, pages 81–115. Dynamic Programming. Dover Publications, New York, 2003.

[19] H. Belzner, T. Lange, and I. Matschke. Traffic information with seamless coverage. *ATZ Worldwide*, 7(112):510–515, 2010.

[20] A. Bergmann. *Abgasnachbehandlung Dieselmotor*, pages 772–801. Handbuch Verbrennungsmotoren. Springer Science+Business Media, Wiesbaden, 4 edition, 2007.

[21] S. Bernsteiner. Integration of Advanced Driver Assistance Systems on Full-Vehicle Level – Parametrization of an Adaptive Cruise Control System Based on Test Drives. Doctoral thesis, 2015. Institute of Automotive Engineering, Graz University of Technology.

[22] D. P. Bertsekas. *The Dynamic Programming Algorithm*, volume 1 of *Dynamic Programming and Optimal Control*, chapter 1, pages 1–62. Athena Scientific, Belmont, 3 edition, 2005.

[23] J. W. Biermann. *Fahrzeugauslegung*, chapter 5, pages 101–161. Energiemanagement im Fahrzeug. Springer Science+Business Media, Wiesbaden, 2014.

[24] J. W. Biermann and C. Renner. *Betriebsstrategien*, chapter 4, pages 301–324. Kraftfahrzeug-Hybridantriebe. Springer Science+Business Media, Wiesbaden, 2012.

[25] Yang Bin, Yaoyu Li, Qiuming Gong, and Zhong-Ren Peng. Multi-information integrated trip specific optimal power management for plug-in hybrid electric vehicles. In *American Control Conference, 2009. ACC '09.*, pages 4607–4612, 2009.

[26] J. Böhle and B. Stiebels. Der neue Touareg Hybrid. *ATZ Extra*, 14(12):30–35, 2009.

[27] H. Borhan, A. Vahidi, A. M. Phillips, M. L. Kuang, I. V. Kolmanovsky, and S. Di Cairano. MPC-Based Energy Management of a Power-Split Hybrid Electric Vehicle. *Control Systems Technology, IEEE Transactions on*, 20(3):593–603, 2012.

[28] M. Börjesson and I. Kristoffersson. The Gothenburg congestion charge. Effects, design and politics. *Transportation Research Part A: Policy and Practice*, 75:134–146, 5 2015.

[29] J. Bossdorf-Zimmer, H. Kollmer, R. Henze, and F. Kücükay. Fingerprint des Fahrers zur Adaption von Assistenzsystemen. *ATZ – Automobiltechnische Zeitschrift*, 113(3):226–231, 2011.

[30] K. Brandt. *Einsatzfelder für Lithium-Ionen-Batterien*, chapter 31, pages 383–391. Handbuch Lithium-Ionen-Batterie. Springer Science+Business Media, Heidelberg, 2013.

[31] S. Braun, M. Krauss, F. Rattei, W. Bohne, M. Engelmann, U. Deuke, and M. Di Pierro. The full hybrid powertrain for BMW activehybrid X6. *ATZ Worldwide*, 111(11):4–12, 2009.

[32] S. Di Cairano, D. Bernardini, A. Bemporad, and I. V. Kolmanovsky. Stochastic MPC With Learning for Driver-Predictive Vehicle Control and its Application to HEV Energy Management. *Control Systems Technology, IEEE Transactions on*, 22(3):1018–1031, 2014.

[33] S. Di Cairano, Wei Liang, I. V. Kolmanovsky, M. L. Kuang, and A. M. Phillips. Power Smoothing Energy Management and Its Application to a Series Hybrid Powertrain. *Control Systems Technology, IEEE Transactions on*, 21(6):2091–2103, 2013.

[34] C. C. Chan. The State of the Art of Electric, Hybrid, and Fuel Cell Vehicles. *Proceedings of the IEEE*, 95(4):704–718, 2007.

[35] A. Chasse, P. Pognant-Gros, and A. Sciarretta. Online implementation of an optimal supervisory control for a parallel hybrid powertrain. *SAE Int.J. Engines 2(1)*, 2009.

[36] Zheng Chen, C. C. Mi, Jun Xu, Xianzhi Gong, and Chenwen You. Energy Management for a Power-Split Plug-in Hybrid Electric Vehicle Based on Dynamic Programming and Neural Networks. *Vehicular Technology, IEEE Transactions on*, 63(4):1567–1580, 2014.

[37] M. Darms. *Fusion umfelderfassender Sensoren*, chapter 17, pages 237–248. Handbuch Fahrerassistenzsysteme. Vieweg+Teubner Verlag, Wiesbaden, 2012.

[38] H. Diess. BMW i3 und BMW i8. Zeitgemäße Antriebsstränge für eine neue Freude am Fahren. *35. International Vienna Motor Symposium 2014*, pages 1–14, 2014.

[39] G. Dillmann, G. Prys, C. Klinkert, J. Sauer, A. Otasevic, and R. Steinbock. Efficient Driving. *ATZ Extra*, 13(8):48–55, 2008.

[40] E. Donges. *Fahrerverhaltensmodelle*, chapter 2, pages 15–23. Handbuch Fahrerassistenzsysteme. Vieweg+Teubner, Wiesbaden, 1 edition, 2009.

[41] R. Dorn, R. Schwartz, and B. Steurich. *Batteriemanagementsystem*, chapter 14,

pages 177–187. Handbuch Lithium-Ionen-Batterie. Springer Science+Business Media, Heidelberg, 2013.

[42] S. Ebbesen, P. Elbert, and L. Guzzella. Battery State-of-Health Perceptive Energy Management for Hybrid Electric Vehicles. *Vehicular Technology, IEEE Transactions on*, 61(7):2893–2900, 2012.

[43] L. Eckstein and G. Mimberg. *Power train*, chapter 3, pages 137–198. Longitudinal Dynamics of Vehicles. fka - Forschungsgesellschaft Kraftfahrwesen mbH Aachen, Aachen, 2014.

[44] H. Eichlseder. Verbrennungskraftmaschinen – Vertiefte Ausbildung. Lecture notes, Institute for Internal Combustion Engines and Thermodynamics, Graz University of Technology, 2005.

[45] P. Elbert, S. Ebbesen, and L. Guzzella. Implementation of dynamic programming for n-dimensional optimal control problems with final state constraints. *Control Systems Technology, IEEE Transactions on*, 21(3):924–931, 2013. ID: 1.

[46] R. B. Ellison, S. P. Greaves, and D. A. Hensher. Five years of London's low emission zone: Effects on vehicle fleet composition and air quality. *Transportation Research Part D: Transport and Environment*, 23:25–33, 8 2013.

[47] EU. Verordnung (EG) Nr. 443/2009 des Europäischen Parlaments und des Rates vom 23. April 2009 zur Festsetzung von Emissionsnormen für neue Personenkraftwagen im Rahmen des Gesamtkonzepts der Gemeinschaft zur Verringerung der CO_2-Emissionen von Personenkraftwagen und leichten Nutzfahrzeugen, 2009.

[48] ERTICO ITS Europe. http://adasis.org/. Accessed on 08/05 2015.

[49] MWV Mineralölwirtschaftsverband e.V. Durchschnittlicher Preis für Dieselkraftstoff in Deutschland in den Jahren 1950 bis 2015* (Cent pro Liter). Available at http://de.statista.com/statistik/daten/studie/779/umfrage/durchschnittspreis-fuer-dieselkraftstoff-seit-dem-jahr-1950/, 2015. Accessed on 09/12 2015.

[50] MWV Mineralölwirtschaftsverband e.V. Durchschnittlicher Preis für Superbenzin in Deutschland in den Jahren 1972 bis 2015* (Cent pro Liter). Available at http://de.statista.com/statistik/daten/studie/776/umfrage/durchschnittspreis-fuer-superbenzin-seit-dem-jahr-1972/, 2015. Accessed on 09/12 2015.

[51] P. Firsching, M. Kneißer, and M. Rauch. Segeln und erweitertes Start-Stopp im Kleinwagensegment. *ATZ – Automobiltechnische Zeitschrift*, 117(9):56–61, 2015.

[52] R. Fischer, G. Jürgens, F. Kücükay, R. Najork, and B. Pollak. *Kernaufgabe der Fahrzeuggetriebe*, chapter 1, pages 1–45. Das Getriebebuch. Springer Vienna, Vienna, 2012.

[53] R. Fischer, G. Jürgens, F. Kücükay, R. Najork, and B. Pollak. *Steuerung und Regelung*, chapter 5, pages 187–215. Das Getriebebuch. Springer Vienna, Vienna, 2012.

[54] O. Foellinger. *Die Dynamische Programmierung von Bellman*, chapter 7, pages 237–279. Optimale Regelung und Steuerung. Oldenburg, Munich, 3 edition, 1994.

[55] O. Foellinger. *Die Strukturoptimierung dynamischer Systeme als Variationsproblem*, chapter 1, pages 21–47. Optimale Regelung und Steuerung. Oldenburg, Munich, 3 edition, 1994.

[56] D. Freundt and B. Lucas. LRR3 von Bosch – Long Range Radar Sensor für den stark Wachsenden Markt der Fahrerassistenzsysteme. pages 55–68, 2008. Wolfsburg, Germany.

[57] Lijun Gao, S. Liu, and R. A. Dougal. Dynamic lithium-ion battery model for system simulation. *Components and Packaging Technologies, IEEE Transactions on*, 25(3):495–505, 2002.

[58] M. Gipser. FTire: a physically based application-oriented tyre model for use with detailed MBS and finite-element suspension models. *Vehicle System Dynamics: International Journal of Vehicle Mechanics and Mobility*, 43:76–91, 2005.

[59] Q. Gong, Y. Li, and Z.-R. Peng. Optimal power management of plug-in HEV with intelligent transportation system. In *Advanced intelligent mechatronics, 2007 IEEE/ASME international conference on*, pages 1–6, 2007.

[60] Q. Gong, Y. Li, and Z.-R. Peng. Computationally efficient optimal power management for plug-in hybrid electric vehicles based on spatial-domain two-scale dynamic programming. *Proceedings of the 2008 IEEE International Conferecne on Vehicular Electronics and Safety*, pages 90–95, 2008.

[61] Q. Gong, Y. Li, and Z.-R. Peng. Trip-based optimal power management of plug-in hybrid electric vehicles. *Vehicular Technology, IEEE Transactions on*, 57(6):3393–3401, 2008. ID: 1.

[62] J. B. Goodenough. *Battery Components, Active Materials for*, chapter 3, pages 51–92. Batteries for Sustainability – Selected Entries from the Encyclopedia of Sustainability Science and Technology. Springer Science+Business Media New York, New York, 2013.

[63] U. D. Grebe and L. T. Nitz. Voltec – The Propulsion System for Chevrolet Volt and Opel Ampera. *MTZ worldwide eMagazine*, 72(5):4–11, 2011.

[64] C.-O. Griebel, F. Rabenstein, M. Klüting, F. Kessler, J. Kretschmer, and E. Hockgeiger. The Full-Hybrid Powertrain of the new BMW ActiveHybrid5. *20. Aachen Colloquium Automobile and Engine Technology*, pages 1–17, 2011.

[65] J. A. Gubner. *Introduction to Markov chains*, chapter 12, pages 476–515. Probability and random processes for electrical and computer engineers. Cambridge University Press, New York, 2006.

[66] L. Guzzella and A. Sciarretta. *Electric and Hybrid-Electric Propulsion Systems*, chapter 4, pages 67–162. Vehicle Propulsion Systems – Introduction to Modeling and Optimization. Springer Science+Business Media, Heidelberg, 3 edition, 2013.

[67] L. Guzzella and A. Sciarretta. *IC-Engine-Based Propulsion Systems*, chapter 3, pages 47–66. Vehicle Propulsion Systems – Introduction to Modeling and Optimization. Springer Science+Business Media, Heidelberg, 3 edition, 2013.

[68] L. Guzzella and A. Sciarretta. *Supervisory Control Algorithms*, chapter 7, pages 243–276. Vehicle Propulsion Systems – Introduction to Modeling and Optimization. Springer Science+Business Media, Heidelberg, 3 edition, 2013.

[69] L. Guzzella and A. Sciarretta. *Vehicle Energy and Fuel Consumption – Basic Concepts*, chapter 2, pages 13–46. Vehicle Propulsion Systems – Introduction to Modeling and Optimization. Springer Science+Business Media, Heidelberg, 3 edition, 2013.

[70] M. H. Hajimiri and F. R. Salmasi. A Fuzzy Energy Management Strategy for Series Hybrid Electric Vehicle with Predictive Control and Durability Extension of the Battery. *Electric and Hybrid Vehicles, 2006. ICEHV '06. IEEE Conference on*, pages 1–5, 2006.

[71] J. G. Hayes, R. P. R. de Oliveira, S. Vaughan, and M. G. Egan. Simplified electric vehicle power train models and range estimation. In *Vehicle Power and Propulsion Conference (VPPC), 2011 IEEE*, pages 1–5, 2011.

[72] R. L. Hirsch, R. Bezdek, and R. Wendeling. *Peaking of World Oil Production: Impacts, Mitigation, and Risk Management*. Report, DOE NETL. February 2005.

[73] W. Hirschberg. TMsimple: A simple to use tyre model. Technical report, Institute of Automotive Engineering, Graz University of Technology, 2009.

[74] W. Hirschberg, F. Palcak, G. Rill, and J. Sotnik. Reliable Vehicle Dynamics Simulation in Spite of Uncertain Input Data. In *12th EAEC European Automotive Congress 2009*. Slovak Society of Automotive Engineers (SAITS), 2009. Bratislava.

[75] W. Hirschberg and H. M. Waser. Fahrzeugdynamik. Lecture notes, Institute of Automotive Engineering, Graz University of Technology, 2010.

[76] W. Hirschberg and H. M. Waser. Kraftfahrzeugtechnik. Lecture notes, Institute of Automotive Engineering, Graz University of Technology, 2012.

[77] M. Hirz, W. Dietrich, A. Gfrerrer, and J. Lang. *Integrated Computer-Aided Design in Automotive Development – Development Processes, Geometric Fundamentals, Methods of CAD, Knowledge-Based Engineering Data Management*. Springer Science+Business Media, Springer Heidelberg New York Dordrecht London, 2013.

[78] P. Hofmann. *Definition und Klassifizierung der Hybridkonzepte*, chapter 2, pages 17–54. Hybridfahrzeuge – Ein alternatives Antriebskonzept für die Zukunft. Springer Wien, 2010.

[79] P. Hofmann. *Hybridkomponenten*, chapter 4, pages 101–205. Hybridfahrzeuge – Ein alternatives Antriebskonzept für die Zukunft. Springer Wien, 2010.

[80] M. Hofstetter. Kraftstoffeinsparungspotential von Plug-In Hybridfahrzeugen mit

prädiktiver Betriebsstrategie. Master thesis, 2014. Institute of Automotive Engineering, Graz University of Technology.

[81] G. Hohenberg, T. D. D. Terra, C. Schyr, K. Gschweitl, and C. Christ. Anforderungen an Prüfstände für Hybridfahrzeuge. *MTZ-Konferenz Motor 2006*, pages 103–114, 2006.

[82] C. Holman, R. Harrison, and X. Querol. Review of the efficacy of low emission zones to improve urban air quality in European cities. *Atmospheric Environment*, 111:161–169, 6 2015.

[83] M. Horn and N. Dourdoumas. *Dimensionierung von Standardreglern*, chapter 15, pages 257–270. Regelungstechnik. Addison-Wesley Verlag, Munich, 1 edition, 2004.

[84] T. Huber. *Modellgestützte Hybrid Systementwicklung – Modellierung und Optimierung*, chapter 14, pages 328–340. Elektronisches Management motorischer Fahrzeugantriebe – Elektronik, Modellbildung, Regelung und Diagnose für Verbrennungsmotoren, Getriebe und Elektroantriebe. Vieweg+Teubner, Wiesbaden, 1 edition, 2010.

[85] A. Hülsmann. Methodenentwicklung zur virtuellen Auslegung von Lastwechselphänomenen in PKW. Doctoral thesis, 2007. Fakultät für Maschinenwesen der Technischen Universität München (TUM).

[86] T. Hüsemann. *Driving Dynamics*, volume 2 of *Chassis Handbook. Fundamentals, Driving Dynamics, Components, Mechatronics, Perspectives*, chapter 2, pages 35–147. Vieweg and Teubner, 1 edition, 2011.

[87] National imagery and mapping agency (NIMA). Department of Defense World Geodetic System 1984. Technical Report NIMA TR8350.2, 2000.

[88] SAE International. Hybrid Electric Vehicle (HEV) and Electric Vehicle (EV) Terminology, 2008.

[89] N. Jalil, N. A. Kheir, and M. Salman. A rule-based energy management strategy for a series hybrid vehicle. *Proceedings of the American Control Conference*, 1:689–693, 1997.

[90] S.-I. Jeon, Y.-I. Park, J.-M. Lee, and S.-T. Jo. Multi-Mode Driving Control of a Parallel Hybrid Electric Vehicle Using Driving Pattern Recognition. *Journal of Dynamic Systems, Measurement, and Control*, 124(1):141–149, August 28 2000.

[91] Bingnan Jiang and Yunsi Fei. On-road PHEV power management with hierarchical strategies in vehicular networks. *IEEE Intelligent Vehicles Symposium (IV)*, pages 1077–1084, 2014.

[92] L. Johannesson, M. Asbogard, and B. Egardt. Assessing the Potential of Predictive Control for Hybrid Vehicle Powertrains Using Stochastic Dynamic Programming. *Intelligent Transportation Systems, IEEE Transactions on*, 8(1):71–83, 2007.

[93] P. Karoshi, K. Tieber, G. Peneder, C. Kneissl, H. Kraus, M. Hofstetter, J. Fabian,

and M. Ackerl. A History-Based Load Requirement Prediction Algorithm, for Predictive Hybrid- and Thermal Operation Strategies. *SAE International*, 12.-14.4.2016, 2016.

[94] KBA. Pkw-Bestand in Deutschland nach Kraftstoffarten (Stand: 1.Januar 2015). Available at http://de.statista.com/statistik/daten/studie/4270/umfrage/pkw-bestand-in-deutschland-nach-kraftstoffarten/, 2015. Accessed on 9.8 2015.

[95] P. Keil and A. Jossen. Aufbau und Parametrierung von Batteriemodellen. *19. DESIGN&ELEKTRONIK–Entwicklerforum Batterien & Ladekonzepte*, 2012.

[96] U. Keller, M. Back, F. Nietfeld, M. Mürwald, and A. Docter. Plug-In Hybrid von Mercedes-Benz – Der Antriebsstrang des S500 Plug-In Hybrid. *35. International Vienna Motor Symposium 2014*, 2014.

[97] U. Keller, T. Gödecke, M. Weiss, C. Enderle, and G. Henning. Diesel Hybrid - The Next Generation of Hybrid Powertrains by Mercedes-Benz. *33. International Vienna Motor Symposium 2012*, pages 1–20, 2012.

[98] U. Keller, S. Schmiedler, J. Strenkert, N. Ruzicka, and F. Nietfield. *Plug-In Hybrid from Mercedes-Benz – The next generation PLUG-IN Hybrid with 4-cylinder gasoline engine*, pages 829–850. 15. Internationales Stuttgarter Symposium. Springer Fachmedien, Wiesbaden, 2015.

[99] S. Kermani, S. Delprat, R. Trigui, and T.-M. Guerra. Predictive energy management of hybrid vehicle. *Vehicle Power and Propulsion Conference, 2008. VPPC '08. IEEE*, pages 1–6, 2008.

[100] J. T. B. A. Kessels, M. W. T. Koot, P. P. J. van den Bosch, and D. B. Kok. Online Energy Management for Hybrid Electric Vehicles. *Vehicular Technology, IEEE Transactions on*, 57(6):3428–3440, 2008.

[101] T. Van Keulen, B. De Jager, J. Kessels, and M. Steinbuch. Energy management in hybrid electric vehicles: Benefit of prediction. pages 264–269, 2010.

[102] T. Van Keulen, B. De Jager, and M. Steinbuch. An adaptive sub-optimal energy management strategy for hybrid drive-trains. *IFAC Proceedings of the 17th World Congress*, 2008.

[103] U. Kiencke and L. Nielsen. *Engine Control Systems*, chapter 5, pages 99–148. Automotive Control Systems. Springer-Verlag Berlin Heidelberg, Springer-Verlag Berlin Heidelberg, 2 edition, 2005.

[104] U. Kiencke and L. Nielsen. *Road and Driver Models*, chapter 11, pages 425–464. Automotive Control Systems. Springer-Verlag Berlin Heidelberg, 2 edition, 2005.

[105] T. Kleine-Besten, U. Kersken, W. Pöchmüller, and H. Schepers. *Navigation und Telematik*, chapter 39, pages 599–624. Handbuch Fahrerassistenzsysteme. Vieweg+Teubner Verlag, Wiesbaden, 2012.

[106] B. Klima, A. Huss, and M. Nöst. Integrated methodology for simulation and

measurement of the diesel hybrid potential. *ATZ worldwide*, 111(2):50–56, 02/01 2009.

[107] S. Knirsch, R. Straßer, G. Schiele, S. Möhn, W. Binder, and M. Enzinger. The Powertrain of the new Audi Q7 e-tron 3.0 TDI quattro. *36. International Vienna Motor Symposium 2015*, pages 229–251, 2015.

[108] R. Kochhan, S. Fuchs, B. Reuter, P. Burda, S. Matz, and M. Lienkamp. An Overview of Costs for Vehicle Components, Fuel and Greenhouse Gas Emissions. *ResearchGate*, pages 1–18, 2014.

[109] U. Köhler. *Aufbau von Lithium-Ionen-Batteriesystemen*, chapter 8, pages 95–106. Handbuch Lithium-Ionen-Batterie. Springer Science+Business Media, Heidelberg, 2013.

[110] P. Köpf, C. Sasse, K. Steinel, and G. Wagner. *Antriebe*, chapter 5, pages 150–348. Vieweg Handbuch Kraftfahrzeugtechnik. Springer Science+Business Media, Wiesbaden, 5 edition, 2007.

[111] KPMG. KPMG's Global Automotive Executive Survey 2015. Report, pages 1–40, 2015.

[112] D. Kraft, T. Huber, and S. Sterzing-Oppel. *Simulation und Auslegung*, chapter 5, pages 325–340. Kraftfahrzeug-Hybridantriebe. Vieweg+Teubner Verlag, Wiesbaden, 2012.

[113] U. Kramer. *Längsführung*, chapter 3, pages 63–92. Fahrzeugführung: Modelle, Simulation und Regelung. Hansen, Munich, 2008.

[114] H. Kraus, M. Ackerl, and P. Karoshi. Performance Analysis of Plug-In Hybrid Passenger Vehicles. *FISITA World Automotive Congress*, 02-06.06.2014, 2014. Maastricht.

[115] H. Kraus, M. Ackerl, P. Karoshi, M. Hofstetter, and J. Fabian. A new approach to an adaptive and predictive operation strategy for PHEVs. *SAE International*, 21-23-04.2015, 2015.

[116] R. Langari and J. S. Won. Intelligent energy management agent for a parallel hybrid vehicle – part I: system architecture and design of the driving situation identification process. *Vehicular Technology, IEEE Transactions on*, 54(3):925–934, 2005.

[117] P. Langen and W. Nehse. BMW EfficientDynamics – looking in the future. *30. International Vienna Motor Symposium 2009*, pages 138–147, 2009.

[118] M. Lederer. *Anforderungen an das Energiemanagement*, chapter 2, pages 11–45. Energiemanagement im Fahrzeug. Springer Science+Business Media, Wiesbaden, 2014.

[119] S. Lefevre, Chao Sun, R. Bajcsy, and C. Laugier. Comparison of parametric and

non-parametric approaches for vehicle speed prediction. In *American Control Conference (ACC), 2014*, pages 3494–3499, Portland, 2014.

[120] S. Leuthner. *Übersicht zu Lithium-Ionen-Batterien*, chapter 2, pages 13–19. Handbuch Lithium-Ionen-Batterie. Springer Science+Business Media, Heidelberg, 2013.

[121] J. Liebl. *Einleitung*, chapter 1, pages 1–9. Energiemanagement im Fahrzeug. Springer Science+Business Media, Wiesbaden, 2014.

[122] Chan-Chiao Lin, Jun-Mo Kang, J. W. Grizzle, and Huei Peng. Energy management strategy for a parallel hybrid electric truck. *American Control Conference, 2001. Proceedings of the 2001*, 4:2878–2883, 2001.

[123] Chan-Chiao Lin, Huei Peng, and J. W. Grizzle. A stochastic control strategy for hybrid electric vehicles. In *American Control Conference, 2004. Proceedings of the 2004*, volume 5, pages 4710–4715, 2004.

[124] M. Lindemann, T.-M. Wolter, R. Freimann, and S. Fengler. Simulation as a solution for designing hybrid powertrains. *ATZ worldwide*, 111(5):12–17, 05/01 2009.

[125] A. Lohrengel and P. Dietz. *Kupplungen und Bremsen*, chapter G3, pages 501–515. Dubbel. Springer Berlin Heidelberg, 2014.

[126] A. A. Malikopoulos. Supervisory Power Management Control Algorithms for Hybrid Electric Vehicles: A Survey. *Intelligent Transportation Systems, IEEE Transactions on*, 15(5):1869–1885, 2014.

[127] P. Markschläger, H.-G. Wahl, F. Weberbauer, and M. Lederer. *Assistenzsystem für mehr Kraftstoffeffizienz*, chapter 3, pages 146–153. Vernetztes Automobil. Springer Science+Business Media, Wiesbaden, 2014.

[128] O. Martens. Regelung einer permanenterregten Synchronmaschine. Lecture notes, pages 1–23. Institute of Control Engineering, TU Braunschweig, 2015.

[129] MATLAB. *version 7.11.0.584 (R2010b)*. The MathWorks Inc., 2010.

[130] F. Matthies. Beitrag zur Modellbildung von Antriebssträngen für Fahrbarkeitsuntersuchungen. Doctoral thesis, 2013. Fakultät IV für Elektrotechnik und Informatik, Technische Universität Berlin.

[131] G. P. Merker and P. Eckert. *Verbrennung*, chapter 21, pages 638–656. Handbuch Verbrennungsmotor. Springer Science+Business Media, Wiesbaden, 7 edition, 2015.

[132] M. Mitschke and H. Wallentowitz. *Aerodynamik des Kraftfahrzeuges*, chapter 3, pages 55–69. Dynamik der Kraftfahrzeuge. Springer Fachmedien Wiesbaden, Wiesbaden, 5 edition, 2014.

[133] M. Mitschke and H. Wallentowitz. *Fahrleistung und Kraftstoffverbrauch*, chapter 7, pages 137–181. Dynamik der Kraftfahrzeuge. Springer Fachmedien Wiesbaden, Wiesbaden, 5 edition, 2014.

[134] M. Mitschke and H. Wallentowitz. *Leistungsangebot, Kennfelder von Kraftfahrzeugantrieben*, chapter 6, pages 89–135. Dynamik der Kraftfahrzeuge. Springer Fachmedien Wiesbaden, Wiesbaden, 5 edition, 2014.

[135] M. Mitschke and H. Wallentowitz. *Reifen*, chapter 2, pages 9–54. Dynamik der Kraftfahrzeuge. Springer Fachmedien Wiesbaden, Wiesbaden, 5 edition, 2014.

[136] G. Mohan, F. Assadian, and S. Longo. Comparative analysis of forward-facing models vs. backward-facing models in powertrain component sizing. In *Hybrid and Electric Vehicles Conference 2013 (HEVC 2013), IET*, pages 1–6, 2013.

[137] S. J. Moura, H. K. Fathy, D. S. Callaway, and J. L. Stein. A stochastic optimal control approach for power management in plug-in hybrid electric vehicles. *Control Systems Technology, IEEE Transactions on*, 19(3):545–555, 2011. ID: 1.

[138] N. Müller, S. Strauß, S. Tumback, and A. Christ. Segeln – Start/Stopp-Systeme der nächsten Generation. *MTZ – Motortechnische Zeitschrift*, 72(9):644–649, 2011.

[139] C. Musardo, G. Rizzoni, and B. Staccia. A-ECMS: An Adaptive Algorithm for Hybrid Electric Vehicle Energy Management. In *Decision and Control, 2005 and 2005 European Control Conference. CDC-ECC '05. 44th IEEE Conference on*, pages 1816–1823, 2005.

[140] United Nations. Concerning the Adoption of Uniform Technical Prescriptions for Wheeled Vehicles, Equipment and Parts which can be Fitted and/or be Used on Wheeled Vehicles and the Conditions for Reciprocal Recognition of Approvals Granted on the Basis of these Prescriptions, 2015.

[141] H. Naunheimer, B. Bertsche, and G. Lechner. *Leistungsbedarf und Leistungsangebot*, chapter 3, pages 73–99. Fahrzeuggetriebe – Grundlagen, Auswahl, Auslegung und Konstruktion. Springer Berlin Heidelberg, Heidelberg, 2007.

[142] H. Naunheimer, B. Bertsche, and G. Lechner. *Systematik der Fahrzeuggetriebe: Konstruktive Grundkonzepte*, chapter 6, pages 141–237. Fahrzeuggetriebe – Grundlagen, Auswahl, Auslegung und Konstruktion. Springer Berlin Heidelberg, Heidelberg, 2007.

[143] H. Naunheimer, B. Bertsche, and G. Lechner. *Überblick über das System Verkehr-Fahrzeug-Getriebe*, chapter 2, pages 28–72. Fahrzeuggetriebe – Grundlagen, Auswahl, Auslegung und Konstruktion. Springer Berlin Heidelberg, Heidelberg, 2007.

[144] H. Neudorfer, A. Binder, and N. Wicker. Analyse von unterschiedlichen Fahrzyklen für den Einsatz von Elektrofahrzeugen. *Elektrotechnik & Informationstechnik*, 123/7/8: 352–360, 2006.

[145] N.N. PELOPS White Paper. Technical report, Forschungsgesellschaft Kraftfahrwesen mbH Aachen, 2007.

[146] N.N. Toyota Prius III. *ATZ – Automobiltechnische Zeitschrift*, 111(11):806–809, 2009.

[147] N.N. IPG Documentation – IPGDriver. User manual, IPG Automotive GmbH, 2012.

[148] N.N. 2015 Honda Accord Hybrid Overview – Official Site. Available at http://automobiles.honda.com/accord-hybrid/, 2015. Accessed on 09/11 2015.

[149] ÖAMTC. Durchschnittliche Kraftstoffpreise (Jahreswerte in €). Available at http://www.oeamtc.at/portal/tanken+2500++1004854, 2015. Accessed on 09/17 2015.

[150] C. Oertel, A. Fandre. Das Reifenmodellsystem RMOD-K Ein Beitrag zum virtuellen Fahrzeug. *ATZ – Automobiltechnische Zeitschrift*, (11):1074–1079, 2001.

[151] The International Council on Clean Transportation (icct). CO2 emissions from new passenger cars in the EU: Car manufacturer's performance in 2014. Technical report, icct, 2015.

[152] D. F. Opila, D. Aswani, R. McGee, J. A. Cook, and J. W. Grizzle. Incorporating drivability metrics into optimal energy management strategies for hybrid vehicles. In *Decision and Control, 2008. CDC 2008. 47th IEEE Conference on*, pages 4382–4389, 2008. ID: 1.

[153] N. A. Owen, O. R. Inderwildi, and D. A. King. The status of conventional world oil reserves – Hype or cause for concern? *Energy Policy*, 38(8):4743–4749, 8 2010.

[154] H. B. Pacejka and I. J. M. Besselink. Magic Formula Tyre Model with Transient Properties. *Vehicle System Dynamics: International Journal of Vehicle Mechanics and Mobility*, 27:234–249, 1997.

[155] G. Paganelli, M. Tateno, A. Brahma, G. Rizzoni, and Y. Guezennec. Control development for a hybrid-electric sport-utility vehicle: strategy, implementation and field test results. In *American Control Conference, 2001. Proceedings of the 2001*, volume 6, pages 5064–5069, 2001.

[156] M. Papageorgiou, M. Leibold, and M. Buss. *Optimierung – Statische, dynamische, stochastische Verfahren für die Anwendung*, volume 3. Springer-Verlag Berlin Heidelberg, Berlin, 2012.

[157] R. M. Patil, Z. Filipi, and H. K. Fathy. Comparison of Supervisory Control Strategies for Series Plug-In Hybrid Electric Vehicle Powertrains Through Dynamic Programming. *Control Systems Technology, IEEE Transactions on*, 22(2):502–509, 2014.

[158] M. Percoco. The effect of road pricing on traffic composition: Evidence from a natural experiment in Milan, Italy. *Transport Policy*, 31:55–60, 1 2014.

[159] P. Pisu and G. Rizzoni. A Comparative Study Of Supervisory Control Strategies for Hybrid Electric Vehicles. *Control Systems Technology, IEEE Transactions on*, 15(3):506–518, 2007.

[160] R. Prud'homme and J. P. Bocarejo. The London congestion charge: a tentative economic appraisal. *Transport Policy*, 12(3):279–287, 5 2005.

[161] J. E. B. Randles. Kinetics of rapid electrode reactions. *Discussions of the Faraday Society*, 1:11–19, 1947.

[162] E. Rapaport. The Stockholm environmental zone, a method to curb air pollution from bus and truck traffic. *Transportation Research Part D: Transport and Environment*, 7(3):213–224, 5 2002.

[163] A. Riel, W. Hasewend, E. Bogner, and R. Fischer. Vehicle and powertrain modelling in the hole development process. *ATZ worldwide*, 106(6):6–13, 06/01 2004.

[164] M. Ringdorfer. Integrated Vehicle Dynamics Controller for Electric Drives and Mechatronic Drivetrain Components. Doctoral thesis, 2014. Institut für Regelungs- und Automatisierungstechnik, Graz University of Technology.

[165] G. Ripaccioli, D. Bernardini, S. Di Cairano, A. Bemporad, and I. V. Kolmanovsky. A stochastic model predictive control approach for series hybrid electric vehicle power management. In *American Control Conference (ACC), 2010*, pages 5844–5849, 2010.

[166] K. Rohde-Brandenburger. *Verbrauch in Fahrzyklus und im Realverkehr*, chapter 7, pages 243–306. Energiemanagment im Kraftfahrzeug. Springer Science+Business Media, Wiesbaden, 2014.

[167] M. Roth. *Simulation*, chapter 10, pages 367–414. Energiemanagement im Fahrzeug. Springer Science+Business Media, Wiesbaden, 2014.

[168] G. Rousseau, D. Sinoquet, and P. Rouchon. Constrained Optimization of Energy Management for a Mild-Hybrid Vehicle. *Oil & Gas Science and Technology -Rev. IFP*, 62(4):623–634, 2007.

[169] S. Saenger-Zetina and M. Wagner. *Hybride Antriebsstrukturen*, chapter 2, pages 7–74. Kraftfahrzeug-Hybridantriebe. Springer Science+Business Media, Wiesbaden, 2012.

[170] M. Salman, N. J. Schouten, and N. A. Kheir. Control strategies for parallel hybrid vehicles. *American Control Conference, 2000. Proceedings of the 2000*, 1(6):524–528, 2000.

[171] S. Samuel, L. Austin, and D. Morrey. Automotive test drive cycles for emission measurement and real-world emission levels – A Review. *Journal of Automotive Engineering, Proceedings of IMechE Part D*, 216(7):555–564, 2002.

[172] F. Schäfer and C. Von Essen. *Abgasemissionen*, chapter 21, pages 817–891. Handbuch Verbrennungsmotor. Springer Science+Business Media, Wiesbaden, 7 edition, 2015.

[173] F. Schäfer and C. Von Essen. *Hybridantriebe*, chapter 29, pages 1080–1158. Hand-

buch Verbrennungsmotor. Springer Science+Business Media, Wiesbaden, 7 edition, 2015.

[174] R. Schedel. Viel Entwicklungspotential in der Aerodynamik. *ATZ – Automobiltechnische Zeitschrift*, 109(1):40–45, 2007.

[175] Wurster U. Schieschke, R. IPG-TIRE Ein flexibles, umfassendes, Reifenmodell für den Einsatz in Simulationsumgebungen. *Automobil-Industrie*, 33.Jahrgang(5):495–500, 1988.

[176] M. Schöttle. Toyota Prius Plug-in. *ATZelektronik*, 5(6):42–45, 2010.

[177] N. J. Schouten, M. A. Salman, and N. A. Kheir. Fuzzy logic control for parallel hybrid vehicles. *Control Systems Technology, IEEE Transactions on*, 10(3):460–468, 2002.

[178] M. Schraut. Umgebungserfassung auf Basis lernender digitaler Karten zur vorausschauenden Konditionierung von Fahrerassistenzsystemen. Doctoral thesis, 2000. Fakultät für Elektrotechnik und Informationstechnik, Technische Universität München (TUM).

[179] U. Schreiber and J. Schindler. Complete vehicle powertrain simulation. *ATZ worldwide*, 103(6):20–22, 06/01 2001.

[180] C. Schröder. McKinsey: Marktanteil von Hybrid- und Elektrofahrzeugen liegt 2020 bei bis zu 33 %. *ATZonline.de*, 2009. Accessed on 02/12 2014.

[181] T. Schütz, L. Krüger, and M. Lentzen. *Luftkräfte und deren Beeinflussung an Personenkraftwagen*, chapter 4, pages 177–382. Hucho - Aerodynamik des Automobils. Springer Science+Business Media, Wiesbaden, 6 edition, 2013.

[182] A. Sciarretta, M. Back, and L. Guzzella. Optimal control of parallel hybrid electric vehicles. *Control Systems Technology, IEEE Transactions on*, 12(3):352–363, 2004.

[183] A. Sciarretta and L. Guzzella. Control of hybrid electric vehicles. *Control Systems, IEEE*, 27(2):60–70, 2007.

[184] OPEC Secretariat. 2014 World Oil Outlook. Technical report, Organization of the Petroleum Exporting Countries (OPEC), 2014.

[185] D. Semmler, J. Kerner, L. Spiegel, O. Bitsche, T. Rauner, I. Stache, and M. Marques. Der Antriebsstrang des Porsche Panamera S E-Hybrid. *34. International Vienna Motor Symposium 2013*, 25:26, 2013.

[186] L. Serrao, S. Onori, A. Sciarretta, Y. Guezennec, and G. Rizzoni. Optimal energy management of hybrid electric vehicles including battery aging. In *American Control Conference (ACC), 2011*, pages 2125–2130, 2011.

[187] R. Sims, R. Schaeffer, F. Creutzig, X. Cruz-Núnez, M. D'Agosto, D. Dimitriu, M. J. Figueroa, L. Fulton, S. Kobayashi, O. Lah, A. McKinnon, P. Newman, M. Ouyang, J. J. Schauer, D. Sperling, and G. Tiwari. *Transport*, chapter 8, pages 599–670.

Climate Change 2014: Mitigation of Climate Change. Contribution of Working Group III to the Fifth Assessment Report of the Intergovernmental Panel on Climate Change. Cambridge University Press, Cambridge, 2014.

[188] S. Sorrell, J. Speirs, R. Bentley, A. Brandt, and R. Miller. Global oil depletion: A review of the evidence. *Energy Policy*, 38(9):5290–5295, 9 2010.

[189] G. P. Stein, O. Mano, and A. Shashua. Vision-based ACC with a single camera: bounds on range and range rate accuracy. In *IEEE Intelligent Vehicles Symposium*, pages 120–125. IEEE, 2003. Columbus.

[190] C. Sun, S. J. Moura, Xiaosong Hu, J. K. Hedrick, and Fengchun Sun. Dynamic Traffic Feedback Data Enabled Energy Management in Plug-in Hybrid Electric Vehicles. *Control Systems Technology, IEEE Transactions on*, 23(3):1075–1086, 2015.

[191] O. Sundström. Optimal control and design of hybrid-electric vehicles. Doctoral thesis, 2009. Institute for Dynamic Systems and Control, ETH Zurich.

[192] O. Sundström, D. Ambuehl, and L. Guzzella. On implementation of dynamic programming for optimal control problems with final state constraints. *Oil & Gas Science and Technology -Rev. IFP*, 65(1):91–102, 2010.

[193] O. Sundström and L. Guzzella. A generic dynamic programming matlab function. In *Control Applications, (CCA) & Intelligent Control, (ISIC), 2009 IEEE*, pages 1625–1630, 2009. ID: 1.

[194] Core Writing Team, R. K. Pachauri, and L. A. Meyer. Climate Change 2014: Synthesis Report. Contribution of Working Groups I, II and III to the Fifth Assessment Report of the Intergovernmental Panel on Climate Change. Technical report, IPCC, 2015.

[195] Wang Tiedong and Hu Jingjing. Applying floating car data in traffic monitoring. *Control Science and Systems Engineering (CCSSE), 2014 IEEE International Conference on*, pages 96–99, 2014.

[196] M. Timmann and M. Renz. 48 V at Mercedes-Benz – options for further applications. *14. Internationales Stuttgarter Symposium*, pages 645–663, 2014.

[197] L. Ulrich. Top ten tech cars. *Spectrum, IEEE*, 51(4):38–47, 2014.

[198] H. Unbehauen. *Grundlagen der Fuzzy-Regelung*, chapter 10, pages 329–360. Regelungstechnik I. Vieweg+Teubner Verlag, 2001.

[199] A7 Landes und Gemeindeentwicklung. *Registerzählung 2011 – Erwerbstätige und Pendler*. Number 5 in Steirische Statistiken. Mayer, M.; Graz, 2014.

[200] Department of Economic United Nations and Social Affairs. Weltbevölkerung nach Kontinenten im Jahr 2010 und Prognose für 2100 (in Millionen). Available at http://de.statista.com/statistik/daten/studie/184686/umfrage/weltbevoelkerung-nach-kontinenten/, 2015. Accessed on 09/12 2015.

[201] M. Vennebörger, C. Strübel, B. Wies, and K. Wiese. Leichtlaufreifen für Pkw mit niedrigem CO2-Ausstoss. *ATZ – Automobiltechnische Zeitschrift*, 115(7-8):572–577, 2013.

[202] O. Vollrath, N. Armstrong, A. Lamm, O. Bitsche, and J. Schenk. The hybrid solution by Mercedes-Benz in S-Class. *ATZ Worldwide*, 111(5):4–11, 2009.

[203] H. C. Watson and E. E. Milkins. An international drive cycle. *Proceedings of 21th FISITA Congress Belgrade*, 1986.

[204] X. Wei. Modeling and control of a hybrid electric drivetrain for optimum fuel economy, performance and driveability. Doctoral thesis, 2004. Ohio State University.

[205] X. Wei and G. Rizzoni. Objective Metrics of Fuel Economy, Performance and Driveability – A Review. *SAE International*, 2004.

[206] S. Winkelmann and H. Harmuth. *Schaltbare Reibkupplungen*, volume 34. Springer-Verlag Berlin Heidelberg New York Tokyo, Berlin, 1985.

[207] H. Winner. *Radarsensorik*, chapter 12, pages 123–185. Handbuch Fahrerassistenzsysteme. Vieweg+Teubner Verlag, Wiesbaden, 2012.

[208] J.-S. Won and R. Langari. Intelligent Energy Management Agent for a Parallel Hybrid Vehicle. *Proceeding of the American Control Conference*, pages 2560–2565, June 2003.

[209] J.-S. Won and R. Langari. Intelligent Energy Management Agent for a Parallel Hybrid Vehicle – Part II: Torque Distribution, Charge Sustenance Strategies, and Performance Results. *Vehicular Technology, IEEE Transactions on*, 54(3):935–953, 2005.

[210] Gao Xiangyang, Zhang Jun, and Ning Ning. Transient behavior modeling and physical meaning analysis for Battery. In *Computer Application and System Modeling (ICCASM), 2010 International Conference on*, volume 2, pages V2–383–V2–386, 2010.

[211] Y. Yokoi, S. Ichikawa, S. Doki, S. Okuma, T. Naitou, T. Shiimado, and N. Miki. Driving pattern prediction for an energy management system of hybrid electric vehicles in a specific driving course. In *Industrial Electronics Society, 2004. IECON 2004. 30th Annual Conference of IEEE*, volume 2, pages 1727–1732, 2004.

[212] R. Zanasi, G. Sandoni, and R. Morselli. Simulation of variable dynamic dimension systems: The clutch example. *Proceeding of the European Control Conference 2001*, pages 3149–3154, 2001.

[213] M. G. Zeyen and A. Wiebelt. *Thermisches Management der Batterie*, chapter 13, pages 165–175. Handbuch Lithium-Ionen-Batterie. Springer Science+Business Media, Heidelberg, 2013.

[214] C. Zhang and A. Vahidi. Real-time optimal control of plug-in hybrid vehicles with trip preview. *American Control Conference (ACC), 2010*, pages 6917–6922, 2010.

[215] C. Zhang and A. Vahidi. Route Preview in Energy Management of Plug-in Hybrid Vehicles. *Control Systems Technology, IEEE Transactions on*, 20(2):546–553, 2012.

[216] C. Zhang, A. Vahidi, P. Pisu, X. Li, and K. Tennant. Role of Terrain Preview in Energy Management of Hybrid Electric Vehicles. *Vehicular Technology, IEEE Transactions on*, 59(3):1139–1147, 2010.

[217] H.-J. Zimmermann. *Fuzzy Set Theory – and Its Applications*, volume 4. Springer Science+Business Media, New York, 2001.

[218] VCÖ MOBILITÄT MIT ZUKUNFT. Österreichs Autofahrer fahren immer weniger Kilometer. Available at http://www.vcoe.at/de/presse/aussendungen-archiv/details/items/vcoe-oesterreichs-autofahrer-fahren-immer-weniger-kilometer, 2015. Accessed on 09/17 2015.